

Searching for α -cluster states in ^{12}C using the Active Target Time Projection Chamber Demonstrator

Charlotte WOUTERS

Promotor: Prof. Riccardo Raabe
Begeleiders: Dr. Tommaso Marchi &
Dr. Cobus Swartz

Proefschrift ingediend tot het
 behalen van de graad van
Master of Science in de Fysica

Academiejaar 2015-2016

© Copyright by KU Leuven

Without written permission of the promotores and the authors it is forbidden to reproduce or adapt in any form or by any means any part of this publication. Requests for obtaining the right to reproduce or utilize parts of this publication should be addressed to KU Leuven, Faculteit Wetenschappen, Geel Huis, Kasteelpark Arenberg 11 bus 2100, 3001 Leuven (Heverlee), Telephone +32 16 32 14 01.

A written permission of the promotor is also required to use the methods, products, schematics and programs described in this work for industrial or commercial use, and for submitting this publication in scientific contests.

Dankwoord

In dit dankwoord wil ik een heleboel mensen bedanken die hebben bijgedragen tot het voltooien van dit eindwerk. In de eerste plaats wil ik mijn promotor Riccardo Raabe bedanken, voor de boeiende en aangename tijd die ik dit jaar heb mogen spenderen in de ‘Nuclear Reactions’ groep.

A very big thank you goes out to my daily supervisors Cobus and Tommaso. You made this year a very enriching experience. Thanks for guiding me around at the experiment in Orsay, for all your tips and suggestions during the data analysis and for always making time to answer my questions.

Together with them, I also want to thank the rest of my office, Jannes, Francesca and Simone, for their input into my work and the enjoyable working atmosphere.

I also have to thank the collaborators of the international ACTAR TPC project, especially Thomas and Alex, for sharing our findings and ideas in the monthly web-meetings.

Met het afronden van deze thesis komt er ook een einde aan vijf jaren als fysicastudent. Daarom wil ik graag mijn medestudenten bedanken voor de vele leuke momenten tijdens deze periode. Bedankt ook voor de gezellige pauzemomentjes die het thesissen nog aangenamer maakten.

Als laatste wil ik mijn ouders bedanken voor de steun, de interesse en het luisterend oor. Ook mijn zus en broers, waarbij ik altijd terecht kan voor een lach en ontspanning.

En Ruben, bedankt om er altijd voor mij te zijn!

Scientific summary

This thesis studies the isotope ^{12}C with the objective to learn more about the exact structure of one of its excited states, the Hoyle state. It is named after scientist F. Hoyle who predicted the existence of this 0^+ state at an energy of 7.65 MeV in ^{12}C to explain the natural abundance of carbon in our universe. Because of its location slightly above the energy threshold for α -decay and its extended matter radius that was observed in scattering experiments, the Hoyle state is believed to have a special three-alpha structure. This idea is supported by theory, as the state is not reproduced by the Shell Model, but is predicted by different cluster models.

Because of its deformed structure, the Hoyle state is expected to be accompanied by a rotational band of higher energy cluster states. Candidates for the 2^+ and 4^+ band members have already been proposed in different scattering experiments with ^{12}C . A goal of this study is to validate the excitation energies of these cluster states in ^{12}C and to obtain an estimate of the moment of inertia of the Hoyle state.

For this purpose, a scattering experiment with a 80 MeV ^{12}C ion beam was proposed using a demonstrator of the ACTAR TPC detector at the ALTO facility in Orsay, France. With this high-efficiency detection system, developed to study the most exotic radioactive isotopes, the reaction particles are tracked in a gas volume and a three-dimensional reconstruction of the reaction vertex is possible. This has the big advantage that a good energy resolution can be maintained, even when working with large target thicknesses. Using a He: C_4H_{10} mixture as gas target, reactions of the ^{12}C beam ions with three different target nuclei (C, α and p) can be induced. When an unbound cluster state of ^{12}C gets populated in such a reaction, it immediately decays by break-up and three α -particles are observed in the gas.

After a calibration of the different detectors that cover the walls of the gas chamber, the data are analysed involving a step-by-step reconstruction of the reaction events. By fitting each of the outgoing particle ionization tracks the point of origin of the reaction is determined. Particles that reach the detector wall are identified by constructing the experimental E- ΔE plots from a combined measurement of the energy deposit in the silicon wall detectors and the energy loss in the gas. The extracted information allows for a kinematic reconstruction of the reactions. Both conventional elastic and inelastic scattering as well as inelastic scattering followed by the break-up of an excited ^{12}C nucleus are observed. As a last step the Q-value of the reactions is calculated, resulting in the construction of ^{12}C excitation spectra. The first two member states of the ground state rotational band of ^{12}C at energies of 4.44 MeV and 9.64 MeV are reproduced. A sign of the cluster states is found but they couldn't be identified.

Since this was the first in-beam experiment with the ACTAR TPC Demonstrator, the thesis concludes with an evaluation of its performance in this particular physics case. Since we were not able to identify cluster states in ^{12}C , improvements to the set-up are proposed to make it possible in the future.

Vulgarising summary

Atoms, the building blocks of our universe, exist of a central core which is called the nucleus and is surrounded by a cloud of electrons. The nucleus, which comprises almost all of the atom's mass, is built up of even smaller particles that we call protons and neutrons, or generally nucleons. Usually these protons and neutrons are closely packed and the nucleus is formed as a whole. However, in certain light isotopes an 'exotic' phenomenon can occur involving the nucleons to form little sub-particles or clusters inside the nucleus. This only happens when the nucleus finds itself in a higher energy state, because in this case it becomes energetically favourable for it to adopt a sub-unit structure. The clusters typically consist of two protons and two neutrons and we call this an α -particle. ^{12}C , an isotope of the element carbon, exhibits this cluster phenomenon. When it is given a certain minimal amount of energy, its nucleus will adopt a structure of three α -particles. This state in which ^{12}C finds itself then, is being referred to as the Hoyle state, named after its discoverer Fred Hoyle.

There is a lot of interest in the Hoyle state, not only because of its special structure, but also because of its importance in the nucleosynthesis of the elements. After all, the existence of this specific energy state in ^{12}C allowed for the production of carbon and all heavier elements in stars. Because carbon forms the basis for all organic life, we can say that we owe our existence to the presence of the Hoyle state!

By means of this experiment, we want to learn more on the exact structure of the Hoyle state. Speculation exists for example on a linear chain of α -particles or a triangular configuration. In this respect, it is important to do an exact energy measurement of the Hoyle state and other cluster states in ^{12}C that are correlated with it. The extra energy that is needed to bring ^{12}C in one of its cluster states, is supplied with the help of a nuclear reaction. Such a reaction is induced by making ^{12}C nuclei collide at high velocity with other atoms, with which they can exchange energy. Due to the short lifetime of the cluster states, they will practically immediately break up in the three α -particles of which they were composed. The nuclear reaction and the break up of the ^{12}C nucleus is being measured using a prototype of the ACTAR TPC, a new type of detector being developed to study exotic nuclei. This detector employs a gas volume in which the trails of the different particles leaving the reaction become visible. In this way the reaction can be visually reconstructed. With the information that we retrieve from this and an individual energy measurement of the α -particles, the original energy of the cluster states should be able to be determined.

Due to some unfortunate shortcomings in the set-up of the experiment, we have not completely succeeded in our goal of finding the Hoyle state energy. In another respect however, the experiment can be called a success because it demonstrated what improvements need to happen in the further development of the ACTAR TPC detector.

Vulgariserende samenvatting

Atomen, de bouwstenen van ons heelal, bestaan uit een atoomkern met daarrond een wolk van elektronen. De atoomkern, die bijna alle massa van het atoom bevat, is opgebouwd uit nog kleinere deeltjes die we protonen en neutronen, of algemeen nucleonen, noemen. Gewoonlijk zitten deze protonen en neutronen dicht opeengepakt en vormt de kern één geheel. In bepaalde lichte isotopen kan er echter een ‘exotisch’ fenomeen optreden waarbij de nucleonen subdeeltjes of clusters vormen in de kern. Dit gebeurt enkel wanneer de kern zich in een hogere energietoestand bevindt, omdat het dan energetisch voordeliger wordt om deze structuur aan te nemen. De clusters bestaan typisch uit twee protonen en twee neutronen en dit geheel noemen we een α -deeltje. ^{12}C , een isotoop van het element koolstof, vertoont dit clusterfenomeem. Wanneer het een bepaalde minimum hoeveelheid energie krijgt aangebracht, kan zijn kern een structuur van drie α -deeltjes aannemen. Deze toestand waarin ^{12}C zich dan bevindt wordt naar verwezen als de Hoyle toestand, genoemd naar zijn ontdekker Fred Hoyle.

Er is veel interesse in de Hoyle toestand, niet alleen omwille van zijn speciale structuur, maar ook omwille van zijn belang in de nucleosynthese van de elementen. Het bestaan van deze specifieke energietoestand in ^{12}C heeft namelijk de productie van koolstof en alle zwaardere elementen in sterren mogelijk gemaakt. Omdat koolstof de basis vormt van al het organisch leven, kunnen we zeggen dat we ons bestaan te danken hebben aan de Hoyle toestand!

Aan de hand van dit experiment willen we meer te weten komen over de exacte structuur van de Hoyle toestand. Mogelijkheden waarover gespeculeerd wordt zijn bijvoorbeeld een lineaire ketting van α -deeltjes of een driehoekige configuratie. In dit opzicht is het belangrijk om een exacte energiebepaling te doen van de Hoyle toestand en andere clustertoestanden in ^{12}C die ermee gecorreleerd zijn. De extra energie die nodig is om ^{12}C in één van zijn clustertoestanden te brengen, wordt aangebracht met behulp van een kernreactie. Hierbij worden ^{12}C kernen aan een hoge snelheid tot een botsing gebracht met andere atomen, waarmee ze energie kunnen uitwisselen. Door de korte levensduur van de clustertoestanden, zullen ze vrijwel onmiddellijk opbreken in de drie α -deeltjes waaruit ze waren opgebouwd. De kernreactie en het opbreken van ^{12}C wordt gemeten met behulp van een prototype van de ACTAR TPC, een nieuw type detector ontwikkeld voor het bestuderen van exotische kernen. Deze detector bestaat uit een gas volume waarin de paden van de verschillende deeltjes die uit de kernreactie komen zichtbaar worden. Op deze manier kunnen we de reactie visueel reconstrueren. Met de informatie die we hieruit halen en een individuele energiemeting van de α -deeltjes, moet de originele energie van de clustertoestand achterhaald kunnen worden.

Omwille van enkele onfortuinlijke tekortkomingen in de opstelling van het experiment, zijn we niet geheel in onze opzet geslaagd om de energie van de Hoyle toestand te bepalen. In een ander opzicht kunnen we het experiment wel een succes noemen, omdat het heeft aangetoond welke verbeteringen er moeten gebeuren in de verdere

ontwikkeling van de ACTAR TPC detector.

List of Abbreviations

ACTAR TPC Active Target Time Projection Chamber

ADC Analog-to-digital converter

AGET ASIC for General Electronics for TPCs

ALTO Linear Accelerator and Tandem at Orsay

AsAd ASIC support and analog-digital conversion

CM Center of mass

CoBo Concentration board

DSSD Double-sided silicon strip detector

FWHM Full width half max

GET General Electronics for TPCs

keV Kiloelectron volt

LAB Laboratory

MeV Megaelectron volt

pps Particles per second

SCA Switched capacitor array

Si Silicon

Contents

Dankwoord	i
Summaries	ii
List of Abbreviations	vi
1 Motivation and Physics Case	1
1.1 Nuclear structure	1
1.2 Clustering in light nuclei	3
1.3 The Hoyle state in ^{12}C	5
1.3.1 Discovery and relevance	5
1.3.2 Hoyle band structure	7
1.3.3 Break-up process	10
1.4 Goal of the experiment	11
2 Interactions of Nuclei with a Target Material	13
2.1 Nuclear reactions	13
2.1.1 Notation and types	13
2.1.2 Observables	14
2.1.3 Laboratory vs. Center of mass description	16
2.2 Energy loss of charged particles	17
3 The Experiment at ALTO	20
3.1 Experimental set-up	20
3.1.1 Beam acceleration and intensity reduction	21
3.1.2 Active Target Time Projection Chamber	23
3.1.3 GET electronics	27
3.2 Physics of the ^{12}C experiment	30
3.2.1 Expected reactions	30
3.2.2 Reaction kinematics	31
3.2.3 Energy loss in the He: C_4H_{10} gas mixture	32
4 Data Analysis	34
4.1 Signal processing	34
4.2 Calibration of the detectors	38

4.2.1	Silicon detectors calibration	38
4.2.2	Pad alignment	42
4.3	Event reconstruction	43
4.4	Particle identification	48
4.5	Kinematic reconstruction	52
4.6	^{12}C excitation spectra	57
4.6.1	Ground state band	57
4.6.2	Hoyle band	59
5	Conclusion and Outlook	62
Bibliography		64
Appendix A Calibration Parameters		70
A.1	Double-Sided Silicon Strip Detectors (DSSD)	70
A.2	Maya-Si detectors	76

Chapter 1

Motivation and Physics Case

1.1 Nuclear structure

The origin of nuclear physics can be dated back to Rutherford's famous backscattering experiment in 1911 [1]. In this experiment the structure of the atom as existing of a solid core, the nucleus, surrounded by a cloud of electrons, was demonstrated for the first time. The nucleus is built up of two types of nucleons: positively charged protons and neutrons which have no charge. Each element is characterized by a specific number of protons (Z), while the number of neutrons (N) can vary. Such nuclei with an equal number of protons but a different number of neutrons, are called isotopes. The notation ${}^A_Z X_N$ is used for an isotope of element X with Z protons and N neutrons. A is the mass number and represents the total number of nucleons $Z+N$ in the nucleus.

All isotopes are collected in the nuclear chart, as is done in Figure 1.1, where the vertical axis indicates the proton number and the horizontal axis the neutron number. The isotopes of a certain element can be stable or unstable depending on their number of neutrons. The repelling Coulomb force acting between the positively charged protons tends to break the nucleus apart. Therefore the neutrons are necessary to provide enough attractive nuclear force to counteract this repulsion. When these forces are in equilibrium the nucleus is said to be stable. In the nuclear chart these stable isotopes are coloured in black. The deviation from the $N=Z$ axis shows that heavier nuclei require more neutrons to maintain stability.

Unstable nuclei have a N/Z ratio that deviates from stability values and as a result they have a finite lifetime. In their striving for stability, they will undergo a series of transitions, typically in which nucleons are emitted or protons are converted into neutrons or vice versa. These different types of transitions are known as radioactive decay processes. The experimentally known unstable nuclei are indicated in yellow.

The further away from stability, the shorter the lifetime of the isotopes becomes. The boundaries of the nuclear chart are determined by the proton and neutron drip lines. Neutrons or protons can be added to the nucleus until the neutron or proton separa-

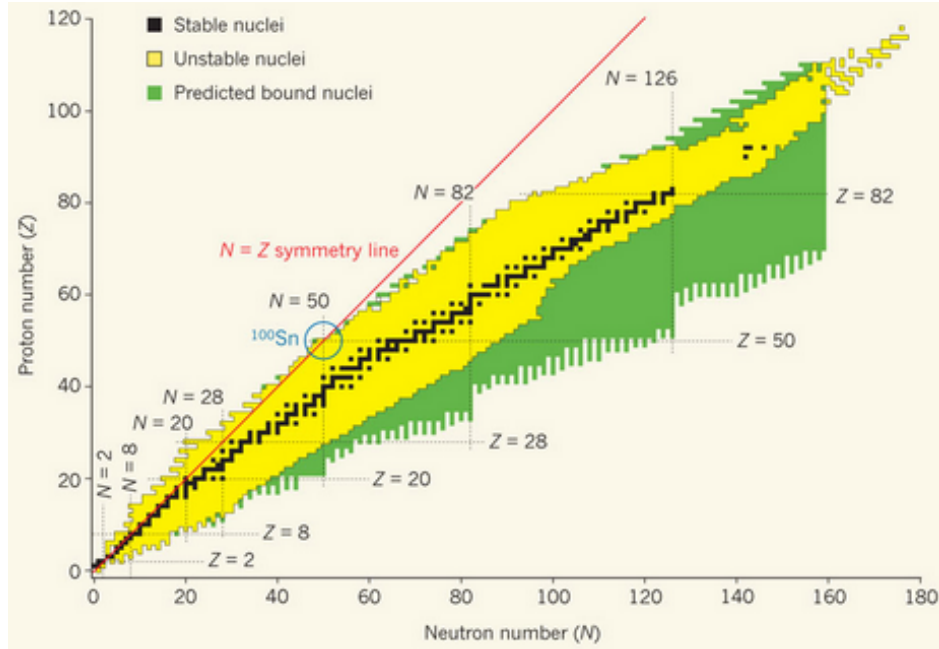


Figure 1.1: The nuclear chart collects all bound nuclei as functions of their proton (Z) and neutron (N) number. Stable nuclei are indicated in black, known unstable nuclei in yellow and unknown but predicted nuclei in green. Dashed lines are drawn at magic proton and neutron numbers, where shell closures occur. Crossings of these lines correspond to doubly magic nuclei. Figure from Ref. [2].

tion energy - the energy required to respectively remove a neutron or a proton from the nucleus - becomes negative. In this case the nucleus will spontaneously decay by nucleon emission. Consequently nuclei beyond the drip lines become unbound and can only exist as resonances. In total, about 7000 nuclei are estimated to exist in between the drip lines. Most of them have not yet been studied and only 254 of them are stable.

Over the past century, extensive studies of isotopes in different regions of the nuclear chart have been performed. One of the main objectives for nuclear physicists is to find predictive models for nuclear structure that reproduce the experimental observations. The important observation of the so called ‘magic numbers’ (Z or $N = 2, 8, 20, 28, 50, 82, 126$) led to the idea that nucleons are arranged in shells, in a similar way as the arrangement of electrons around the nucleus. At these magic proton and neutron numbers a remarkable increase in binding energy¹ appears. They represent the filling of major shells and lead to more stable nuclei. From this idea the Shell Model [3, 4] for nuclear physics was born. This model makes the assumption that a single nucleon moves in a potential created by all of the other nucleons and that no collisions occur between nucleons. By solving the Schrödinger equation with the Shell Model potential while taking into account the spin-orbit interaction, a prediction of the energy levels

¹The binding energy is the energy required to decompose the nucleus into its constituent nucleons. It is equal to the mass difference of the nucleus and the sum of the individual masses of the protons and neutrons that constitute it.

of the different shells/orbitals is obtained. In the ground state of the nucleus, the nucleons fill up the orbitals of lowest energy. When one or more nucleons jump to higher energy orbitals, we speak of an excited nucleus.

For nuclei around shell closures and close to stability, the Shell Model is a very reliable theoretical model. It correctly predicts almost all nuclear features as observed in experiments: the appearance of the magic numbers, the energies, spins and parities of ground and excited nuclear states, nuclear moments, etc. However, as experiments shifted more towards nuclei close to the drip lines, the Shell Model started to fail. Magic numbers changed or disappeared and new striking phenomena occurred, that were never observed before in the vicinity of the valley of stability [5]. Because of this reason these nuclei are referred to as ‘exotic’ nuclei; they exhibit exotic phenomena. Exotic nuclei can be strongly deformed, in contrast to the spherical shape of the near-closed shell nuclei. Consequently the assumption of spherical symmetry that is used for the Shell Model potential is not valid anymore. To describe the exotic features new theoretical models are needed. Of course these models need to be verified by experimental results and thus an extensive and systematic study of exotic isotopes is essential. As exotic nuclei are typically very short-lived, very fast measuring techniques are required. Therefore in today’s nuclear physics there is a strong focus on researching and developing innovative experimental techniques for this purpose.

1.2 Clustering in light nuclei

Exotic phenomena are not only found near the drip lines, they also appear in stable nuclei in the bottom part of the nuclear chart, where the light nuclei are situated. Some particular phenomena, such as cluster and halo structures, occur typically in light nuclei with mass number below 30. A first sign of the existence of this type of nuclei with special nucleonic composition was found in scattering experiments from which the radius of nuclei could be determined [6, 7]. For some nuclei huge matter radii were observed that would be expected for nuclei with mass number higher than 200. This anomaly could be explained by so called halo and cluster nuclei. In halo nuclei [8, 9] typically one or more neutrons are in an orbit with large radius around the rest of the nucleus. In cluster nuclei, groups of nucleons form little conglomerates that interact with each other. These phenomena are characteristic for light nuclei, in which the shell structure is loosened up or dominated by few-body or few-cluster effects.

The idea of clustering in nuclei first arose with the discovery of α -decay in heavy nuclei. In this process a ${}^4\text{He}$ nucleus, which is referred to as an α -particle, is emitted after being preformed in the nucleus. The α -particle, composed of two protons and two neutrons, was observed to be much more stable than any other light nucleus. Because of its high binding energy, a large amount of energy is needed to decompose it into its constituent nucleons. From this observation, it was deduced that it would be energetically favourable for nucleons to arrange themselves in groups of two neutrons and two protons and form α -particles inside the nucleus. This assumption was confirmed

by an experimental study of the binding energies of light nuclei [10]. As can be seen in Figure 1.2, a maximum in binding energy per nucleon appears for nuclei with even and equal number of protons and neutrons. These are exactly the nuclei that would be composed of 1 α -cluster (^4He), 2 α -clusters (^8Be), 3 α -clusters (^{12}C) and so on (^{16}O , ^{20}Ne , ^{24}Mg , ^{28}Si).

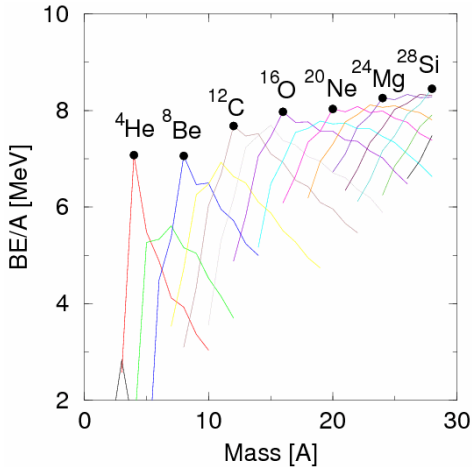


Figure 1.2: *Binding energies per nucleon in light nuclei. The lines connect isotopes of the same Z-value and reach a maximum for nuclei with even and equal numbers of protons and neutrons (=4n nuclei). Figure from Ref. [11].*

According to Hafstad and Teller [12], cluster structures should appear in the ground states of these nuclei. Their assumption was based on the discovery of a linear dependence between the number of inter α -particle bonds in a nucleus and its binding energy. Later it was clarified that this is actually only true for ^8Be [13]. On the contrary, states with an α -cluster character typically manifest themselves in excited states at energies close to the alpha decay threshold of the nucleus. This idea was formulated by Ikeda in the 1960s and summarized in the Ikeda diagram [14] (see Figure 1.3). The threshold energy for alpha decay corresponds to the mass difference between the mass of the parent nucleus and the sum of the masses of the daughter nucleus and the α -particle. When the nucleus finds itself in an excited state just above this threshold level, it is able to lower its energy by the ejection of an α -particle. As a consequence the nucleus feels the tendency to break-up and it puts its internal energy into the formation of the α -cluster before emitting it.

For nuclei with some additional nucleons on top of the 4n-type nuclei in the Ikeda diagram, like for example ^9Be ($^8\text{Be} + \text{n}$) and ^{14}C ($^{12}\text{C} + 2\text{n}$), similar predictions can be made for cluster excitation thresholds. This type of nuclei adopt a ‘molecular’ configuration at those thresholds, in which the valence nucleons exist in molecular orbits around the α -cluster core [15].

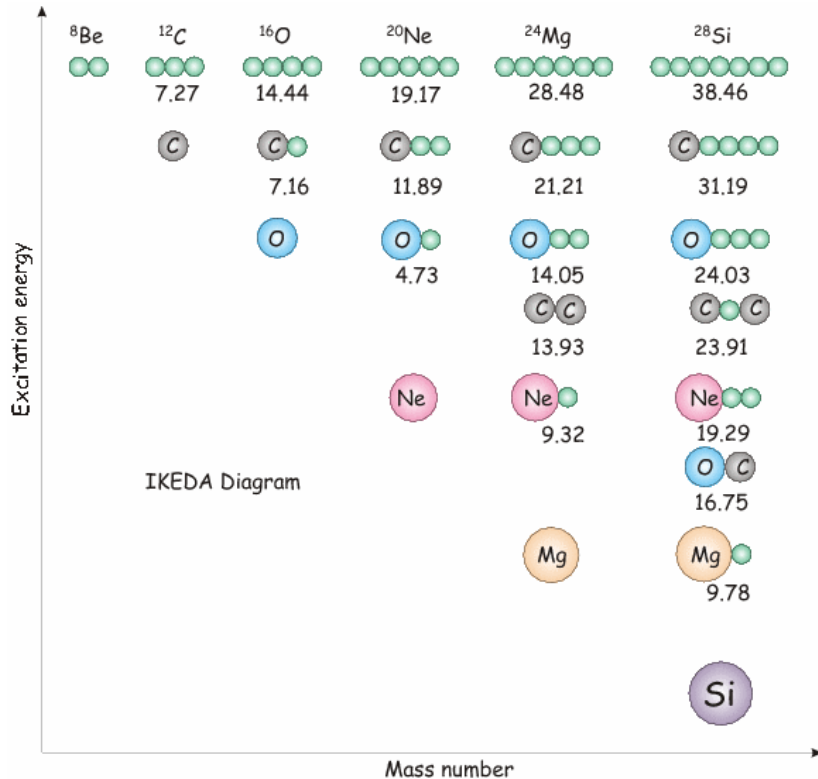


Figure 1.3: *The Ikeda diagram. The cluster structures of the six lightest $4n$ -type nuclei are shown. They are predicted to appear just above the α -decay threshold energies, which are indicated in MeV. Figure from Ref. [14].*

1.3 The Hoyle state in ^{12}C

1.3.1 Discovery and relevance

Carbon is the key element for the origin of organic life. Just like all elements lighter than Fe, it is produced in fusion processes in stars. The main stage of the life of a star consists of hydrogen burning leading to the formation of ^4He . This process generates heat and once the star has reached a critical temperature (about 10^8 K) the ^4He nuclei start to fuse together into ^8Be . The consecutive capture of multiple α -particles then leads to the production of elements with heavier mass (with mass number A+4 after each capture process).

Due to the extremely tight binding of ^4He , ^8Be is unstable and tends to disintegrate into two α -particles. Its ground state energy lies 92 keV above the alpha decay threshold and therefore it decays with a lifetime of only $6.7 \cdot 10^{-17}$ seconds [16]. To enable the production of ^{12}C , the ^8Be must capture a ^4He before it decays into two α -particles. Because of its short lifetime, this actually requires a collision of three ^4He nuclei. This reaction is referred to as the triple alpha process and it proceeds through the continuum of ^{12}C as follows [17],

$$3 \ ^4\text{He} \leftrightarrow ^{12} \text{C}^* \rightarrow ^{12} \text{C} + \gamma. \quad (1.1)$$

Since a three particle collision is a very low probability reaction, it is unlikely that a large amount of ^{12}C and heavier elements are produced in stars. This is in contradiction with the observed natural abundances of the light elements, in particular ^{12}C and ^{16}O , the latter produced by the capture of an α -particle by ^{12}C . To explain this inconsistency, F. Hoyle suggested the existence of an excited state in ^{12}C slightly above the threshold for decay into ^8Be and an α -particle [18]. The presence of such a state would create a resonance causing the capture reaction rate to increase by a factor of $10^7 - 10^8$. To account for the observed absolute abundance of ^{12}C and relative abundances of ^{12}C and ^{16}O , Hoyle predicted the state to appear at an energy of 7.65 MeV [18]. In 1953 a group of physicists at Caltech (California Institute of Technology) were the first to confirm Hoyle's predictions. They measured the $^{14}\text{N}(\text{d},\alpha)^{12}\text{C}$ reaction using a high resolution spectrometer and observed a state at 7.68 MeV [19]. A few years later this value was refined to an energy of 7.653 MeV by observing the α -particle emission following the β decay of ^{12}B . This experiment enabled the assignment of spin and parity $J^\pi = 0^+$ to the so-called Hoyle state [20].

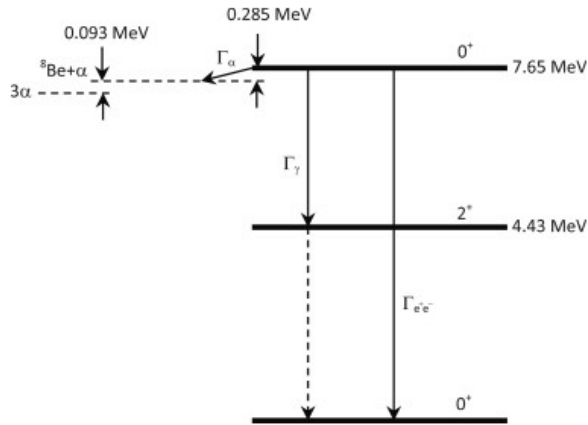


Figure 1.4: Decay scheme of the 0^+ Hoyle state in ^{12}C . Either a decay into three α -particles, or an electromagnetic decay (double γ -decay or pair production) to the ^{12}C ground state is possible. Figure from Ref. [21].

Not only can the Hoyle state explain the natural abundance of ^{12}C , it also has the perfect conditions to adopt an α -cluster structure according to Ikeda's theory. Its energy lies only 0.285 MeV above the alpha decay threshold, corresponding to a state in which the ^8Be -nucleus and the α -particle are separated. Since ^8Be is unbound in its ground state, the 3α decay threshold is in turn only slightly lower in energy by an amount of 93 keV, as illustrated in Figure 1.4. As a consequence, the Hoyle state will use its internal excitation energy as binding energy for clusters and it will adopt a sub-unit structure consisting of three α -particles. This hypothesis was checked by Chernykh et al. [22] in electron scattering experiments performed on ^{12}C in its ground and to the Hoyle state. The data clearly indicate a dilute density of the Hoyle state with a root mean square radius 1.5 times bigger than that of the ground state, which is in accordance with an α -cluster structure. The fact that the Hoyle state is situated higher in energy

than the 3α decay threshold, makes that it is unbound. A decay by break-up in three α -particles is highly favoured as a result of its cluster structure. Yet there remains a small probability for an electromagnetic decay to the ^{12}C ground state. There are two radiative branches contributing to this process: either two consecutive gamma decays with the first excited 2^+ state (4.44 MeV) as intermediate state, or pair production² directly to the ground state (see Figure 1.4).

Now it becomes clear that the link between clustering and thresholds has played a crucial role in the synthesis of the elements in stars. It has provided ^{12}C with a state that allowed the production of a sufficient amount of carbon to develop organic life.

In addition to experiments, theorists also strive to unravel the exact structure of the Hoyle state. Shell model calculations have failed to reproduce an energy state in the correct energy region [23]. Hence, since the mid-twentieth century a variety of other models have been developed for theoretical calculations of the Hoyle state and cluster states in general. A few examples of the most successful theories are The Alpha Cluster Model [24, 25], Alpha Condensate and THSR wave function [26, 27], Antisymmetrised Molecular Dynamics (AMD) [28], Fermi-Molecular Dynamics (FMD) [29] and ab initio approaches [30]. The common feature that these theories agree on is a strongly developed cluster structure of the Hoyle state with significant inter- α correlations. To reach a decisive answer to which is the best theory, precise and accurate measurements of the decay modes and excited states related to the Hoyle state are needed.

1.3.2 Hoyle band structure

Now that it is known that the Hoyle state is built up of three α -particles, a new question arises: How are these particles ordered/organized inside the nucleus? Some possibilities that have been proposed are a chain-like structure, a triangular structure or a gas-like structure of α -particles resembling a Bose-Einstein condensate [26]. An investigation of the higher-energy excited states correlated to the Hoyle state in ^{12}C could help finding the answer to this question.

Deformed or non-spherical nuclei are known to be accompanied by a band of rotational excited states. The rotational states are built upon a low-lying deformed state with angular momentum (spin) 0 and have increasing angular momenta J as we go to the next excited state. The energy of a rotational state with angular momentum J is given by

$$E_{rot} = \frac{\hbar^2}{2I} J(J+1) \quad (1.2)$$

and is dependent on the moment of inertia I of the nucleus. The ground state rotational band of ^{12}C has been experimentally established and consists of states with $J^\pi = 0^+, 2^+, 3^-, 4^\pm$ and 5^- (see Figure 1.5) [31, 32, 33]. This particular series of states is a

²An electron-positron pair is created, carrying away the excess in excitation energy.

strong signature of a D_{3h} symmetry, corresponding to a equilateral triangle symmetry of the ground state.

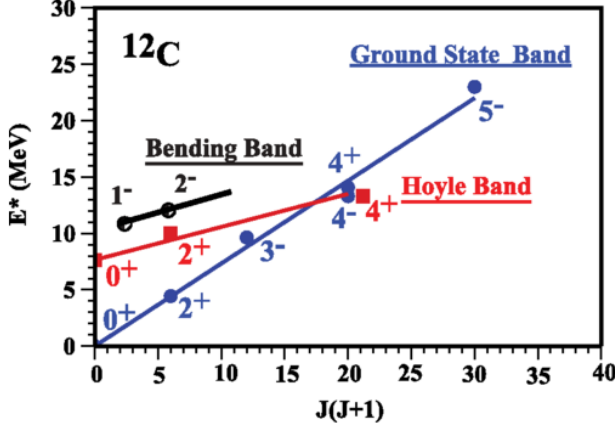


Figure 1.5: *The different rotational band structures in ^{12}C . The smaller slope of the Hoyle band curve with respect to the ground state band indicates a more extended structure. Figure from Ref. [33].*

In an analogous way, the non-spherical Hoyle state is expected to possess such a rotational band of excited cluster states. Haruhiko Morinaga was the first to express this idea in 1956 [34]. Using a model that supposed a chain-like configuration of 3 α -particles, he predicted the first two excited states, the 2^+ and 4^+ , to appear at energies around 9.70 MeV and 14.16 MeV respectively. By experimentally probing the energies of these excited states the moment of inertia of the Hoyle state can be determined. According to Equation (1.2), the slope of the excitation energy versus $J(J + 1)$ curve is inversely proportional to the moment of inertia of the configuration. This important quantity provides valuable information about the degree of deformation and the ordering of the α -particles in the nucleus.

A typical experiment to probe these excited states consists of two steps. First of all ^{12}C has to be produced in one of its excited states above the 3α decay threshold. This can be the Hoyle state, a state belonging to its rotational band or just an excited state of the ground state. There are two methods that are commonly used to access these interesting resonances in ^{12}C : either via decay (α -, β - or γ -decay), or via a scattering process or nuclear reaction (for example transfer reaction). By measuring the energies of the decay or reaction products and using the kinematic laws, the original excitation energies of the ^{12}C nucleus before decay are obtained.

Many of these spectroscopy experiments have been performed over the past 50 years to explore the energy region above the 3α decay threshold. The experimental techniques have advanced over the years but the different results did not always show consistency. Freer et al. [35] and Itoh et al. [36] performed inelastic scattering experiments respectively using the $^{12}C(p, p')^{12}C^*$ and $^{12}C(\alpha, \alpha')^{12}C^*$ reactions. In both cases the

spectrum is dominated by two sharp peaks, corresponding to a 3^- state at 9.64 MeV and a 1^- state at 10.84 MeV. Additionally a very broad 0^+ state is observed in the 10 MeV region. This broad 0^+ contribution was suppressed by measuring at particular angles and after a fit of the data, a 2^+ state could be extracted in both experiments. This is illustrated in the energy excitation spectrum from a proton inelastic scattering experiment by Freer et al., as shown in Figure 1.6. The respective energies measured for the 2^+ states are 9.75(0.15) MeV for Freer and 9.84(6) MeV for Itoh, both about 2 MeV above the Hoyle state. Since the observed width of the 2^+ peak (750(150) keV and 1.01(0.15) MeV respectively) is consistent with that of an α -cluster state and it was found in the same energy region as theoretically predicted, it was considered a good candidate for the 2^+ state of the rotational band built upon the Hoyle state.

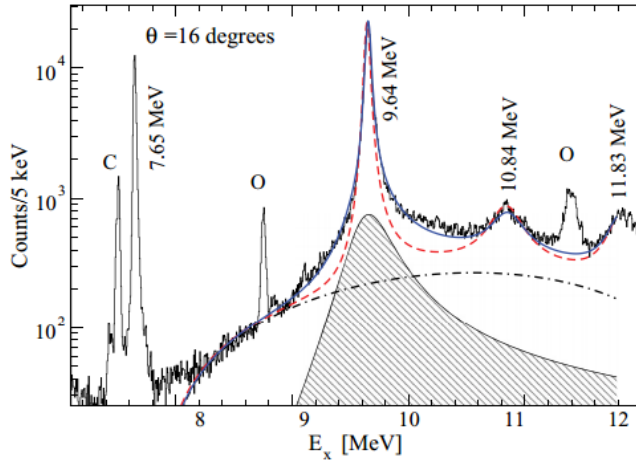


Figure 1.6: Example of a ^{12}C excitation spectrum obtained from a proton inelastic scattering experiment with a beam energy of 66 MeV and a scattering angle of 16° . The Hoyle state at 7.65 MeV and the 3^- and 1^- states at 9.64 MeV and 10.84 MeV are clearly visible as peaks in the spectrum. The dot-dashed line corresponds to the broad 0^+ state. The red dashed fit curve is obtained from all known ^{12}C states. For the blue curve an additional 2^+ contribution (hatched region) at an energy of 9.75 MeV is included and a much better fit to the data is obtained. Figure from Ref. [35].

In β -decay experiments [37] however, no indication of a 2^+ state in that energy region was found. Spectra obtained from ^{12}B and ^{12}N decay measurements show a dominant 0^+ component, as seen in the scattering experiments in the 10 MeV region, with a broad width of approximately 3 MeV. The lack of a significant 2^+ state can possibly be explained by no or little overlap/similarity between the parent nuclei (^{12}B and ^{12}N) and the excited α -cluster state. The transition is therefore strongly inhibited.

Zimmerman et al. [38] confirmed the existence of the 2^+ state found in the inelastic scattering experiments by observing the photo-disintegration of ^{12}C in the reaction $^{12}\text{C}(\gamma, \alpha)^{8}\text{Be}$. By using γ -rays to excite the ^{12}C nuclei, states with $J^\pi = 0^+$ cannot be reached because photons carry at least 1 unit of angular momentum. In this way the

broad 0^+ peak is eliminated from the spectrum and the 2^+ state is easily identified at an energy of 10.03(11) MeV, with a total (α -decay) width of 800(130) keV.

The recent search for the 3rd member of the rotational band has also yielded some positive results. Different inelastic scattering experiments with α -particles revealed a new broad state at an approximate energy of 13.3 MeV, which most likely has spin and parity of 4^+ [39, 40]. This indeed corresponds to the energy region where the 4^+ state would be expected from an extrapolation of the energy of the 2^+ state, assuming a linear chain/bent arm configuration.

With the experiments that have been performed thus far, the existence of a 2^+ state approximately 2 MeV above the Hoyle state has been well established. Its alpha decay width strongly indicates a well-developed α -cluster structure. The current experimental $0^+ - 2^+$ separation excludes a linear arrangement of α -particles, and points more in the direction of a bent chain/triangular structure [35]. Another possibility is a bose-Einstein condensate of spin 0 α -particles, where the model puts the 2^+ 2.3 MeV [22] above the Hoyle state, very close to the present observation. The 4^+ state in the 13-14 MeV region needs further investigation to confirm its existence with certainty. The difficulty of the ^{12}C spectroscopy lies in the presence of a number of strong broad states in the energy region of interest. In this respect there is a need for highly sensitive detection equipment and ways to suppress the influence of non-cluster excited states to improve the results.

1.3.3 Break-up process

As mentioned before the Hoyle state is unbound and because of its well-developed α -cluster structure, decays preferentially by break-up in three α -particles. Due to some disagreements in previous studies [41, 42, 43, 44], it is still under debate whether the decay proceeds as a sequential two-step process via the ground state of ^8Be or if there is an appreciable amount of simultaneous decay in three α -particles. A decisive answer to this question can be important for our understanding of the structure of the Hoyle state and the triple- α reaction rate.

In a recent study [45] this topic was further investigated by probing the decay properties of the Hoyle state in the inelastic $^{12}\text{C} + ^{12}\text{C}$ reaction and in $^{24}\text{Mg}^*$ decay. An important result is the Dalitz-plot shown in Figure 1.7 which is created by comparing the kinematics of the three α -particles from the Hoyle state break-up in the $^{12}\text{C} + ^{12}\text{C}$ reaction. The experimental Dalitz-plot on the left is compared to the results of different decay models. The HF ℓ^3 model [46] which is based on a sequential decay mechanism and shown in the middle, is found to be compatible with the data. In the right panel the results for two types of simultaneous 3 α -decay modes are presented on top of the HF ℓ results: the blue squares assume three α -particles of equal energy and relative angles of 120° (DDL); the green squares assume two α -particles emitted back to back and the

³Hauser-Feshbach sequential evaporation model.

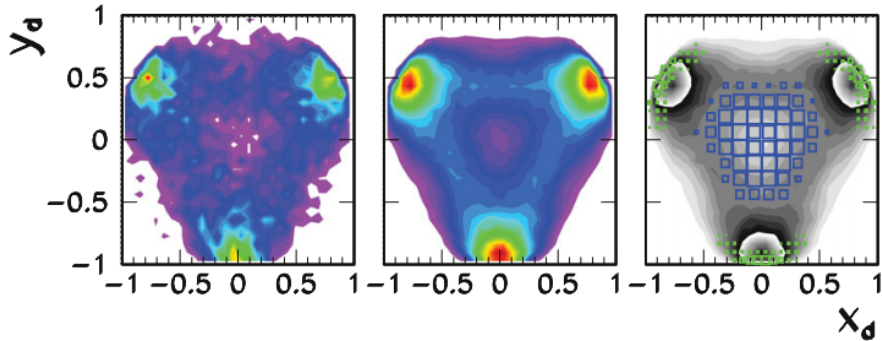


Figure 1.7: *Left panel:* Experimental energy Dalitz-plot obtained from a $^{12}\text{C}+^{12}\text{C}$ peripheral scattering reaction. *Middle panel:* $\text{HF}\ell$ Dalitz-plot. *Right panel:* Predictions for direct decay with equal energies (DDL; blue squares) and direct decay in linear chain (DDE; green squares), superimposed on the $\text{HF}\ell$ prediction. The x - and y -coordinates are defined as $x_d = \sqrt{3}(e_i - e_j)$ and $y_d = 2e_k - e_i - e_j$, where $e_{i,j,k} = E_{i,j,k}/(E_i + E_j + E_k)$ are the normalized α -particle energies in the ^{12}C rest frame. Figure from Ref. [45].

third one at rest in the ^{12}C frame (DDE). Both of these regions are not particularly populated in the data. In the case that the Hoyle state is populated via the decay of $^{24}\text{Mg}^*$ which is formed in $^{12}\text{C}+^{12}\text{C}$ central collisions, a similar agreement with $\text{HF}\ell$ predictions is found. The study concludes on no sizeable deviations (1.1% for DDL and $< 0.02\%$ for DDE) from the sequential decay mechanism with the ^8Be ground state as intermediate stage.

1.4 Goal of the experiment

Because of its unusual α -cluster structure and its key role in the synthesis of the elements, the Hoyle state in ^{12}C has been the focus of lots of experimental activity. Since the mid 1950s, physicists have striven to unravel its precise configuration. At the same time explaining the appearance of the Hoyle state at its particular energy has been a major theoretical challenge. Up to today research is still ongoing about the details of its decay properties and the exact energies of its rotational band members, in order to reach a complete understanding of this interesting ^{12}C resonance.

The goal of this experiment is to measure known and possibly new excited states in ^{12}C using the Active Target Time Projection Chamber (ACTAR TPC) Demonstrator. Based on ^{12}C scattering reactions, excitation spectra of ^{12}C will be constructed with a special interest in cluster states that could be members of a rotational band built on the Hoyle 0^+ state. If the energy of these states can be determined, an estimate of the moment of inertia of the Hoyle state can be made, giving interesting structure information. ACTAR TPC is a new type of gas detection system, in which particle's ionization tracks are detected, allowing the reconstruction of the reaction point in three dimensions. To probe cluster states in ^{12}C the tracking of three α -particles from the cluster break-up following the reaction will be pursued. Therefore this experiment

will allow to assess ACTAR TPC's possibility of tracking multiple particles and its applicability to similar break-up reactions. Indeed, because the Demonstrator is a prototype of the actual ACTAR TPC detector and it is the first time it is used in experiment, its overall performance will have to be evaluated. This includes its ability to identify different particles, measure multiple track events and reconstruct reaction kinematics. Evaluating the newly developed electronics system GET, coupled to this particular set-up, is another purpose of the project. The results of this study will be important in validating the active target concept and proposing possible improvements for the future ACTAR TPC.

Chapter 2

Interactions of Nuclei with a Target Material

2.1 Nuclear reactions

Nuclear reactions serve as a powerful tool to study the structure of (exotic) nuclei. Information on excitation levels and spin assignments of the produced nuclei can be retrieved from energy and angular distribution measurements of the reaction products. To understand and interpret the results of the experiment, some theory about nuclear reactions is needed. The most important and relevant quantities and aspects concerning nuclear reactions will be introduced. The discussion will be focused on direct reaction mechanisms. This type of reactions happens on a very short timescale allowing for an interaction of a single nucleon only. The general ideas in this chapter are taken from [47].

2.1.1 Notation and types

A nuclear reaction takes place when two particles are brought in close contact with each other. It is graphically represented in Figure 2.1 and written down as



In this notation a is the projectile, X the target nucleus, and Y and b the reaction products, respectively called recoil nucleus and ejectile. In a typical experiment, a is a light ion which is accelerated towards a stationary and heavier target X to induce the nuclear reaction. In this case we speak of *direct kinematics*. When the roles are reversed and the heavier particle is used as the projectile, we speak of *inverse kinematics*. This type of experiment is especially interesting when one works with very exotic isotopes. Typically they can not be produced as a target because of their short lifetime and must be used as a beam. Another conventional way to write down the reaction is



where the particles in brackets are the projectile and ejectile respectively.

For two initial particles there are usually different possibilities of the reaction products. A constraint that must be satisfied is the conservation of proton and neutron number: $Z_a + Z_X = Z_Y + Z_b$ (and equivalently for N). The different outcomes of the reaction are called *reaction channels*. When incoming and outgoing particles are the same and stay in their ground state, the reaction is called elastic scattering and can be written as $X(a, a)X$. When one/both of these reaction products is excited to a higher energy state, it is called inelastic scattering. The excited nucleus is indicated as X^* . It is also possible that a nucleon (proton or neutron) or a cluster of nucleons (typically an α -particle) gets transferred from target to projectile or vice versa. In such transfer reactions the composition of the particles changes and new isotopes are created. In any reaction the recoil nucleus Y can be left in an excited state. It will decay in a certain amount of time after the reaction according to its lifetime. Decay possibilities are α -, β -, γ -decay or break-up, depending on the type of nucleus.

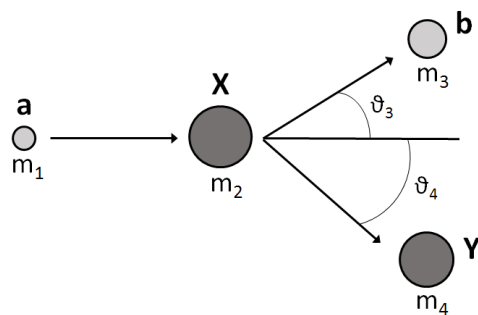


Figure 2.1: Schematic diagram of a nuclear reaction.

2.1.2 Observables

Q-value

In nuclear reaction kinematics, conservation of total relativistic energy holds. In other words, the total energy before the reaction is equal to the total energy after the reaction. The total energy has contributions from the mass of the particles and from their kinetic energies, $E = mc^2 + K$. Since these two quantities are not separately conserved, the Q -value can be introduced to quantify their change in the reaction. It is defined as the initial mass energy minus the final mass energy. If we apply the mass notations as in Figure 2.1, it can be written as

$$Q = (m_1 + m_2 - m_3 - m_4)c^2. \quad (2.3)$$

Of course, since the total energy must be conserved it is at the same time equal to the difference in final and initial kinetic energy. So equivalently,

$$Q = K_3 + K_4 - K_1, \quad (2.4)$$

since X is assumed at rest. A positive Q -value indicates that part of the mass/binding energy is converted to kinetic energy. When the Q -value is negative, kinetic energy is lost to create more heavy particles. In this case there is a threshold energy, equal to minus the Q -value, that is needed for the reaction to happen. Either way, the change in mass is balanced out by the change in kinetic energy.

When an excited state of the final nucleus Y is reached in the reaction, the Q -value will change accordingly. Since the mass energy of this component is now equal to $m_3 + E_{\text{exc}}$, the Q -value decreases with respect to the ground-state case Q_0 :

$$Q = Q_0 - E_{\text{exc}}. \quad (2.5)$$

Consequently, by experimentally measuring the Q -value of a reaction, the excitation spectrum of the partaking nucleus can be obtained.

To get the Q -value from experiment, it is sufficient to measure the information of only one of the reaction products. This follows from conservation of linear momentum. It relates the kinetic energies of the particles to the outgoing angles. Incorporating this law in (2.4), gives the following expression for Q

$$Q = K_3 \left(1 + \frac{m_3}{m_4} \right) - K_1 \left(1 - \frac{m_1}{m_4} \right) - \frac{2}{m_4} (m_1 K_1 m_3 K_3)^{1/2} \cos \theta_3. \quad (2.6)$$

It contains only the kinetic energy and outgoing angle of the ejectile particle b. When the identities of all the participating particles (m_a , m_b , m_Y) and the initial beam energy (T_a) are known, the Q -value can be obtained from the energy and angle of one of the products. So in the case one of them is not detected, the energy release in the reaction can still be determined.

Cross section

The cross section of a reaction is a measure of the relative probability of the reaction to take place. If the outgoing particles of a particular reaction channel appear at a rate R , and I is the beam intensity and N the number of target nuclei per unit area, the cross section σ is defined as

$$\sigma = \frac{R}{IN}. \quad (2.7)$$

It has the dimension of area, but represents a probability. The cross section can be highly dependent on the energy of the incoming particle or emission angle of the products. A resonance reaction for example has a sharp peak in its reaction cross section at a certain beam energy. Typically in an experiment, it is not the total cross section that is measured but the cross section at a particular angle at which the detector is placed. Measurements of the angular distribution of the cross section can provide valuable information for spin and parity assignments of ground and excited states.

The Rutherford cross section describes the cross section for the most basic type of reaction, namely elastic Coulomb scattering. It assumes an interaction solely due to

electrostatic Coulomb forces, which is valid as long as the reacting particle's wave functions don't overlap in the collision. From the following expression for the Rutherford cross section as a function of angle,

$$\frac{d\sigma(\theta)}{d\Omega} = \left(\frac{Z_1 Z_2 e^2}{4\pi\epsilon_0} \right)^2 \left(\frac{1}{4E} \right)^2 \frac{1}{\sin^4(\theta/2)}, \quad (2.8)$$

its properties become clear; it strongly increases with Z-value and strongly decreases with energy and scattering angle. Cross sections for other types of reactions are usually expressed relative to the Rutherford cross section. With an expression for the cross section, the expected yield Y of particles in a certain solid angle Ω can be estimated,

$$Y = I \Delta t N \Delta x \int \frac{d\sigma(\theta)}{d\Omega} d\Omega, \quad (2.9)$$

where I is the beam intensity, Δt the measurement time and N and Δx the respective atomic density and thickness of the target.

2.1.3 Laboratory vs. Center of mass description

Up to now, the reaction kinematics have been described in the laboratory (LAB) frame. In this description the observables have values as seen by a stationary observer. All initial momentum and kinetic energy is carried by the projectile as it moves towards the stationary target. Another way to describe the reaction is from the center of mass (CM) point of view, where the observer is moving along with the center of mass of the system. In this framework the total momentum of the system vanishes. Projectile and target move towards each other with equal and opposite momenta, $m_1 v'_1 = -m_2 v'_2$. The velocities in both frames can be related to each other via the velocity of the center of mass v_{CM}

$$v_1 = v'_1 + v_{CM}. \quad (2.10)$$

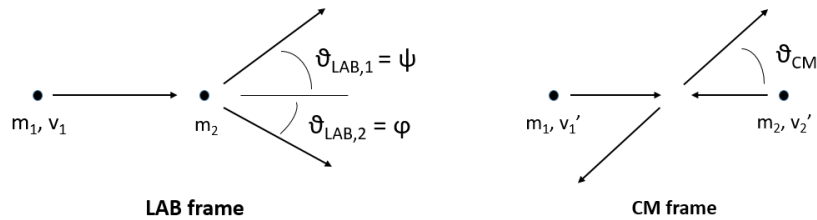


Figure 2.2: Reaction scheme: Laboratory (LAB) frame vs. center of mass (CM) frame.

The reaction observables - such as energy and angle - have different values in the LAB and CM frame. The LAB energy is simply equal to the projectile kinetic energy, $E_{lab} = \frac{1}{2}m_1 v_1^2$. In the CM frame, both initial particles are in motion and the energy

is the sum of their kinetic energies, $E_{\text{CM}} = \frac{1}{2}(m_1 v_1'^2 + m_2 v_2'^2)$. Both quantities can be related to each other in the following way,

$$E_{\text{CM}} = \left(\frac{m_2}{m_1 + m_2} \right) E_{\text{LAB}}, \quad (2.11)$$

and thus $E_{\text{CM}} \leq E_{\text{LAB}}$. The center of mass energy can be regarded as the total available energy for excitations. When the total amount of it goes to excitations of the final nuclei, no kinetic energy is left and both particles are at rest after the reaction in the CM frame. The LAB and CM angles are defined as the angles of the outgoing particles with respect to the original travelling direction in the respective frames (see Figure 2.2). With some simple goniometry and application of the conservation laws in both frames, it is found that

$$\tan \psi = \frac{\sin \theta_{\text{CM}}}{\cos \theta_{\text{CM}} + x} \quad \text{with} \quad x = \left(\frac{m_1 m_3}{m_2 m_4} \frac{E_{\text{CM}}}{E_{\text{CM}} + Q} \right)^{1/2}. \quad (2.12)$$

Differentiating this expression with respect to θ_{CM} , the following condition for the maximum lab scattering angle can be obtained in the case of elastic scattering ($Q = 0$, $m_1 = m_3$ and $m_2 = m_4$) and $m_1 > m_2$,

$$\tan \psi_{\max} = \frac{m_2/m_1}{\sqrt{1 - (m_2/m_1)^2}}. \quad (2.13)$$

For inelastic scattering the maximum angle will only decrease. Since this maximum value is always less than $\pi/2$, there is no backward scattering in inverse kinematics. In direct kinematics ($m_1 < m_2$), no such maximum exists and the scattering in the laboratory covers all angles up to π .

2.2 Energy loss of charged particles

A charged particle travelling through any kind of medium loses energy as a consequence of the interaction with the medium's atoms. This energy loss has contributions of two types of interactions: electronic and nuclear. In the electronic interactions, the ions pass part of their energy to the bound electrons. They can be set free or excited to a higher orbit, leaving behind ionized and excited atoms in the target material. The nuclear part of the energy loss is due to elastic and inelastic collisions with the nuclei of the target. The total depth the particle can travel before it has lost all its energy and is stopped in the material is called the range. It is a very specific property to each particle and can be used as a means of identification.

The *energy loss* or *stopping power* is defined as the energy loss per unit path length dE/dx . It depends on the mass and energy of the particle and on the properties of the medium it is travelling through. According to the original Bethe-Bloch[48] formula for energy loss,

$$\frac{dE}{dx} \sim \frac{Z_1^2 Z_2 \rho}{M_2 E} \ln E, \quad (2.14)$$

with index 1 referring to the travelling particle and index 2 to the target material atoms, E the energy of the particle and ρ the density of the material. In Figure 2.3 the energy loss of carbon, helium and protons in a He:C₄H₁₀ gas mixture is shown as a function of energy as calculated by SRIM [49]. The strong Z_1 and E dependence are clearly outspoken. At intermediate and high energies the energy loss is almost solely due to electronic interactions; the nuclear energy loss is negligible. Only at very low energies ($\lesssim 0.01$ MeV in the case of ¹²C) the nuclear loss is dominating. In each of the curves a

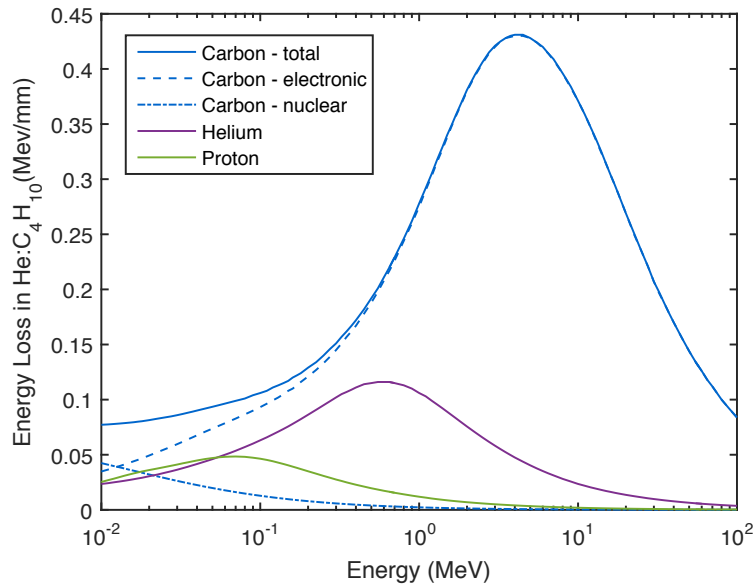


Figure 2.3: *Energy loss curves as a function of energy of carbon, helium and protons in a He:C₄H₁₀ gas mixture with a density of 0.391 mg/cm³. For carbon the separate contributions of electronic and nuclear energy loss are added. Simulated with SRIM [49].*

peak in energy loss can be observed, shifting to higher energies for heavier particles. As a consequence of this shape, the energy loss of the particle, as it slows down along its path, will slightly increase. When its energy reaches the region of the peak formation, it will deposit a relative large part of its energy in a small distance. When it's almost stopped the energy loss decreases again to smaller values. This process results in a characteristic form of the energy loss versus depth curve, as shown in Figure 2.4. The sharp peak at the end of the range is called the Bragg peak.

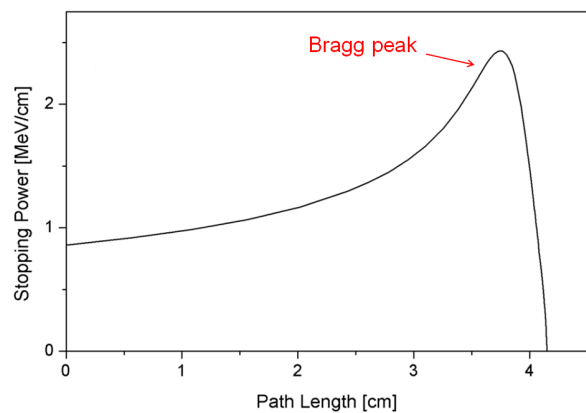


Figure 2.4: *Characteristic shape of an energy loss curve versus depth, with indication of the Bragg peak at the end of the range.*

Chapter 3

The Experiment at ALTO

In this chapter the experiment, which consists of ^{12}C scattering on a target mixture of He:C₄H₁₀, is described. The experiment is performed at the ALTO facility (Linear Accelerator and Tandem at Orsay), which is part of the Institut de Physique Nucléaire d'Orsay (IPNO) situated in France. The ALTO facility is equipped with a linear accelerator, the Tandem accelerator, which provides the ^{12}C ion beam for the scattering experiment. After bending the beam through the Bacchus spectrometer, the reaction takes place at the detection station where the Active Target Time Projection Chamber (ACTAR TPC) Demonstrator is mounted.

3.1 Experimental set-up

ACTAR TPC is a new-generation gas-filled detection system developed to study exotic nuclear reactions [50]. The difference with conventional gas detectors is that, besides being responsible for the detection of particles, the gas medium also acts as the reaction target. A big advantage of this set-up is the capability of reconstructing the reaction point by tracking the outgoing particles in the gas. ACTAR TPC is designed to exploit the most exotic beams that will be produced at second generation Radioactive Ion Beam facilities. The approach that is used gives the unique advantage of measuring nuclear reactions with good efficiency, even with beams whose intensity is of the order $10^2 - 10^3$ pps¹. However, the device's maximum acceptance rate is limited to about 10^6 pps. Since stable beam currents at facilities like ALTO are normally of the order of 10^{10} pps, the attenuation of the beam intensity is needed. For the present experiment this was achieved by placing a primary target in the beam line right after the acceleration stage and selecting scattered ions over a small solid angle, as well as selecting a specific charge state.

A lot of important parameters of ACTAR TPC - such as dynamic range², number

¹particles per second.

²The dynamic range is defined as the ratio between the smallest and largest detectable charges in the gas volume.

of tracks that can be detected, timing and energy resolution, and acceptance rate for events - depend on the electronics that are used. To improve the performances with respect to previous active targets (e.g. the Maya detector [51]), a new electronics system was developed in the framework of the international collaboration GET (General Electronics for TPCs [52]). The main goal of the GET project is the development of an electronic system that is applicable to different types of TPCs. More specifically, it is designed to be compatible with different detector configurations and different gases so that many different experimental approaches can be covered (e.g. decay spectroscopy, nuclear reactions, etc.).

The different parts of the set-up, from acceleration to detection, will be discussed in detail in the following paragraphs.

3.1.1 Beam acceleration and intensity reduction

Van de Graaff generator

Accelerated ion beams can be obtained by injecting ionized atoms in an electrostatic field, created by a Van de Graaff generator. This type of generator was designed by the American physicist Robert Van de Graaff in 1931 and voltages up to several MegaVolts can be produced with it. This is done by transporting charges on a continually moving insulating belt and collecting them on a large spherically shaped electrode (Figure 3.1). The charge is supplied to and removed from the belt by two pointy conductors, called ‘combs’. The lower comb is grounded and drains the belt from negative charges. The

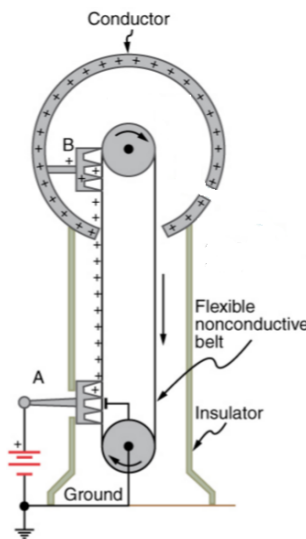


Figure 3.1: *Working principle of a Van de Graaff generator as used in the Tandem accelerator. Figure from Ref. [53].*

positive charge that remains is removed at the top of the belt by the second comb which is connected to the collecting sphere. A large amount of positive charge will be

stored on its outer surface, creating a strong electrostatic field in which particles can be accelerated.

Tandem accelerator

The Tandem accelerator employs the working principle of a van de Graaff generator to create a double acceleration stage. It consists of a long tube with a terminal in the middle where the positive high-voltage Van de Graaff electrode is situated. Negative ions provided by an ion source get accelerated through the first part of the tube towards the terminal. Arrived there, the negative ion beam passes through a stripper device (usually a gas or thin foil), where the electrons are removed from the ions. The negative ion beam is turned into a positive ion beam which is on his turn accelerated away from the large positive charge at the terminal through the second part of the tube. The terminal voltage of the ALTO Tandem accelerator amounts to 13 MV and with this double acceleration mechanism can provide ion beams of energies up to more than hundred MeV according to their charge state [54].

The ion beam as delivered by the Tandem accelerator is guided towards the actual set-up, which is illustrated in Figure 3.2. Beam attenuation is achieved in the reaction chamber and the Bacchus spectrometer, before entering the active target gas.

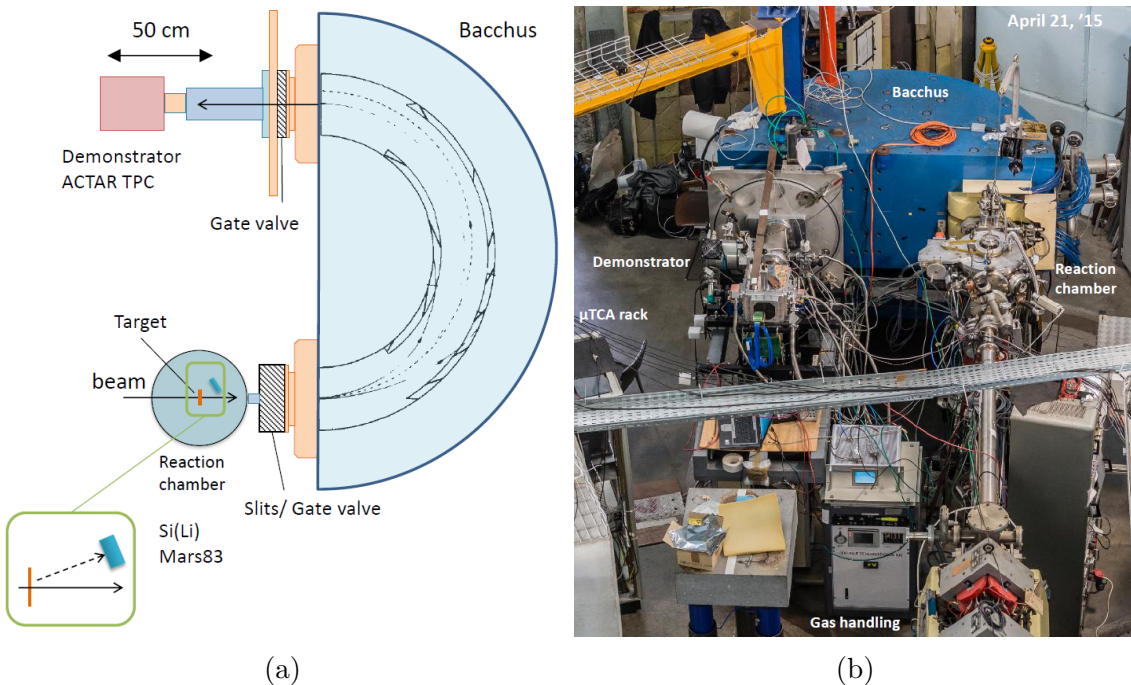


Figure 3.2: *a)* Schematic illustration of the experimental set-up. The beam first passes through the reaction chamber where its intensity is reduced and monitored by the Mars83 detector. By passage through the Bacchus spectrometer a certain charge state is selected and the intensity is further reduced to a desirable value before entering the ACTAR TPC demonstrator. In *(b)* the experimental station located at the ALTO facility is shown.

Reaction chamber

The beam intensity is monitored in the reaction chamber, where a lead target ($900 \mu\text{g}/\text{cm}^2$) is placed in the beam line. Elastically scattered ions are detected at an angle of 20° by a silicon detector (Mars83). From the counts in this lithium doped silicon detector and the known Rutherford cross section for elastic scattering, the beam intensity can be calculated. Typically it amounts to around 10^{10} pps. As already mentioned ACTAR TPC requests a maximal intensity of 10^6 pps, and thus the stable beam intensity has to be reduced. In the first place, this is done by shifting the split openings in front of the Bacchus spectrometer such that its acceptance angle changes from 0° to a few degrees. In this way only beam particles that have elastically scattered on the lead target in a small solid angle are able to enter the dipole magnet. As a result the beam intensity will be reduced by a factor determined by the Rutherford cross section at the selected angle.

Bacchus spectrometer

By passage of the beam through the 180° dipole magnetic spectrometer Bacchus, further reduction of the beam intensity is obtained. In an earlier section, it was explained that in the accelerating stage the ions were stripped from their electrons, making them positively charged. As the number of stripped electrons can vary, the beam leaves the stripping device consisting of ions of different charge states. In the magnetic spectrometer these different charge states q will be bent differently since the magnetic force acting on them is given by $F = qmv$. By tuning the magnetic field one specific charge state can be selected to pass through. The other ones are forced on a different path; they will collide with the spectrometer walls and get absorbed. Alignment of the beam will cause an additional loss of intensity. Two collimators are placed before and after the Bacchus spectrometer with respective apertures of $100 \mu\text{m}$ and 1 mm . Only the ions that are well aligned with the beam direction will reach the end of the collimator. Taking all the attenuation contributions into account, we end up with a desirable beam intensity of about $10^4 - 10^5$ pps.

3.1.2 Active Target Time Projection Chamber

The active target time projection chamber combines the idea of particle tracking, which was first used in the bubble chamber³, with the working principle of a time projection chamber. Charged particles leave an ionization trace in the detection gas from which the electrons are collected on a segmented plane. This combination of target and detector offers great advantages in nuclear reaction experiments, especially for the use of heavy radioactive beams to study exotic nuclei. These types of experiments are performed in inverse kinematics, where the light recoil particle typically emerges with very low energy. With a conventional solid target a very small target thickness

³The bubble chamber, who's invention dates back to 1952 [55], can be considered as the first type of active target. Liquid hydrogen is used as target and at the same visualizes the particle tracks as it gets vaporized and bubbles are formed.

is required to maintain a reasonable resolution. In the active target set-up however, the reaction vertex can be reconstructed from the tracks and one can compensate for the energy loss before the reaction in the kinematic reconstruction. Hence, a large target thickness will not lower the energy resolution. The use of such large target thicknesses also leads to a higher luminosity, which is a great advantage when working with radioactive beams with low production rates.

Detection principle

Beam particles entering the active volume, interact with the nuclei of the gas and reactions occur. Both beam particle and reaction products will ionize gas atoms along their path. An electric field is applied in such a way that the freed electrons drift towards the bottom of the chamber. There they pass an amplification region, where their number is multiplied by a factor of $10^3\text{-}10^5$, and are collected on a segmented detection plane which consists of $2 \times 2 \text{ mm}^2$ squared pads. From the induced signal on the pads a two dimensional projection of the particle tracks becomes visible. The third dimension of the tracks is obtained by measuring the times of arrival of the electrons on the plane. In this way a direct and accurate 3D reconstruction of the reaction vertex is possible, as illustrated in Figure 3.3.

As the particles lose a part of their kinetic energy in each ionization they will be slowed down along their path. From their range and specific energy loss, determined from the recorded ionization signal on the pad plane, different particles can be distinguished from each other. This ability to identify all the particles that take part in the reaction is a very important feature of the ACTAR TPC. Particles that are not stopped in the gas volume will be detected by auxiliary silicon detectors that are placed around it. Their range is not known, but by combining the energy information from the pads and the auxiliary detectors they can also be identified.

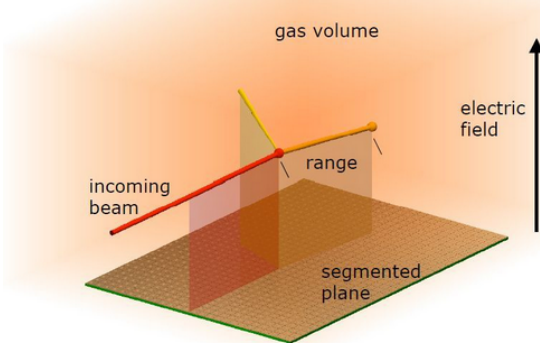


Figure 3.3: *Schematic view of the detection technique of the Active Target and Time Projection Chamber. Ionization electrons formed along the particle tracks are accelerated towards and collected on a segmented detection plane. Figure from Ref. [56].*

Design of the demonstrator

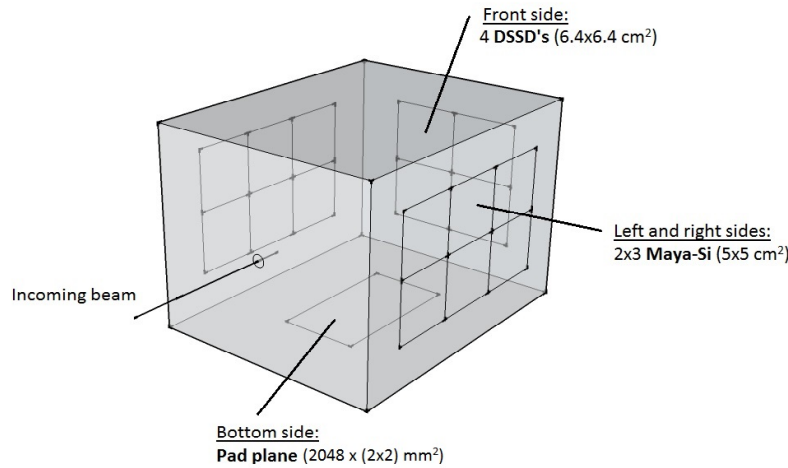
The demonstrator is a first prototype developed in the ACTAR TPC project and is a small-scale version of the final detector. The supporting chamber is made out of aluminum and has internal volume dimensions of $24 \times 19 \times 21 \text{ cm}^3$ (length \times width \times height). The active volume is defined by the field cage inside the chamber, which generates the drift field of $1.23 \cdot 10^4 \text{ V/m}$ for the ionization electrons. The cage is 13.8 cm in length, 7.4 cm in width and the total vertical drift height amounts to 17 cm. The Micromegas amplification stage (see below) and the $12.8 \times 6.4 \text{ cm}^2$ pad plane are located at the bottom of the field cage (see Figure 3.4). The pad plane consists of 64×32 pads of $2 \times 2 \text{ mm}^2$. This results in a total of 2048 signals from the pads that will be read out by the GET electronics, which is discussed in more detail in the next section. To exclude the beam signal from the pad plane, an aluminum foil is covering the four central rows in the pad plane. In this way the trigger signal only starts to build once a reaction has taken place and particles deviate to the left or right part of the pad plane.

Micromegas amplification

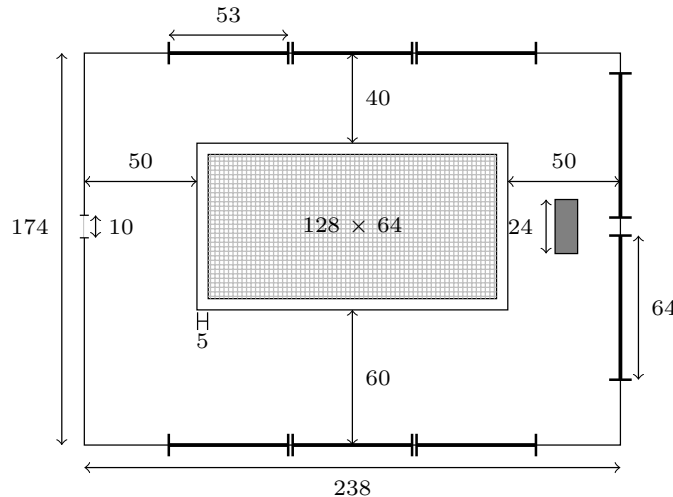
An important component of the detection process in the ACTAR TPC is the electron amplification stage because it determines the spatial and energy resolution and the counting rate for events. The technology that is used is called Micromegas [57] which stands for micromesh gas amplifier. It consists of a small amplification gap, typically 3 mm wide, which is defined by a thin ($5 \mu\text{m}$) metallic micromesh⁴ and the pad plane. A typical Micromegas configuration is shown in Figure 3.5.

In the case of the ACTAR TPC the pad plane is referred to as the anode and it is grounded. In the amplification region a very large electric field is required to produce an avalanche of electrons that will be detected by the anode. Typically, the signal will be spread out over 3-4 pads, resulting in a spatial resolution smaller than the pad size ($< 2 \text{ mm}$). The high amplification field is achieved by applying a voltage to the micromesh. To the drift electrode, which in our set-up is the cathode of the field cage, a higher voltage (i.e. more negative) is applied to achieve the drift field of $\sim 1 \text{ kV/cm}$. For an optimal transmission of the drift electrons through the mesh, Giomataris et al. [57] found that the ratio of E_{amp} to E_{drift} must be as high as possible. They reached electron gain factors close to 10^5 before breakdown. At the same time the high electric field ratio ensures that the positive ions created in the avalanche are fastly collected on the micromesh and evacuated from the detector. This provides a high rate capability of 1 kHz. J. Pancin et al. [58] tested the performance of the Micromegas coupled to a $2 \times 2 \text{ mm}^2$ pad plane. They found an angular resolution of 1° FWHM for short traces (4 cm) and an energy resolution better than 5% for 5.5 MeV α -particles.

⁴A micromesh is a thin metallic grid, typically $5 \mu\text{m}$ thick, with openings of about $20 \mu\text{m}$.



(a) 3D illustration of the Demonstrator chamber with indication of the different detectors.



(b) Top view of the chamber with dimensions in mm. The pad plane has a structure of 64 by 32 pads of 2×2 mm². The outermost border around the pad plane represents the electric field cage. The grey filled rectangle represents the diamond detector.

Figure 3.4: Schematic view of the ACTAR TPC Demonstrator.

Auxiliary silicon detectors

The beam can enter the chamber through a beam aperture centered in the entrance wall with a diameter of 1 cm. To retrieve energy information of particles that would escape the gas, the front and side walls of the chamber are covered with auxiliary silicon (Si) detectors. In this type of detector the energy of a charged particle is measured by the number of charge carriers set free in the detector material. By the electrodes that are placed on either side of the detector a current of the freed electrons and holes

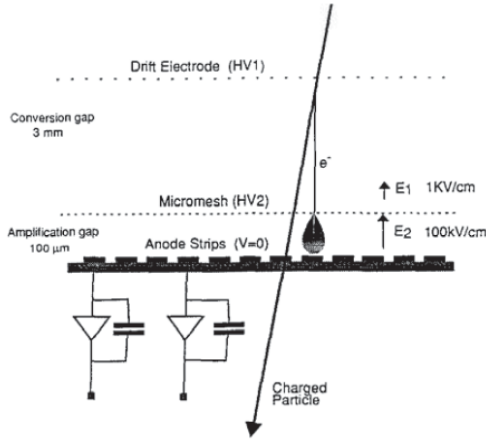


Figure 3.5: Schematic overview of a typical Micromegas configuration. The micromesh separates the low field conversion gap and the small high field amplification gap. In our set-up the conversion gap is actually the full drift space, which is 17 cm wide, and the drift electrode is the upper cathode of the field cage. Figure from Ref. [57].

is induced. This current is measured and is proportional to the deposited energy.

On the front wall four double-sided silicon strip detectors (DSSD, $6.4 \times 6.4 \text{ cm}^2$) are installed in a square configuration. The front and back of each DSSD consist each of 32 detector strips which are placed orthogonally with respect to each other. The strips on the front are positively doped (p-side), while the strips on the back are negatively doped (n-side). In this way both the energy and the two dimensional coordinate of an incident particle can be obtained. On the left and right walls a configuration of 2 by 3 silicon detectors (not segmented), each with dimensions of $5 \times 5 \text{ cm}^2$, is placed. They are called the Maya detectors and they will detect the particles that are scattered at large angles. Unaffected beam particles fly straight through the chamber and are collected by a diamond detector, which is placed in the center on the front wall. This diamond detector is only used as a counter, no energy information is retracted from it. It has dimensions of $2.4 \times 2.4 \text{ cm}^2$ and is blocking the inner corners of the DSSDs.

3.1.3 GET electronics

Figure 3.6 shows a schematic diagram of the GET electronics system [52] that is used. The detection signal from the TPC is fed to the AsAd (ASIC⁵ Support & Analog-Digital conversion) cards, which form the front-end part of the system. The AsAd cards are equipped with four AGET (ASIC for General Electronics for TPCs) chips [59], whose purpose is the amplification and analog storage of the signal. Each of them is supplied with a 12-bit analog-to-digital converter (ADC), which samples the continuous detector signal in time and amplitude. The digitized output of the ADCs is

⁵ASIC stands for application-specific integrated circuit. It is a chip that is designed for a specific use/function.

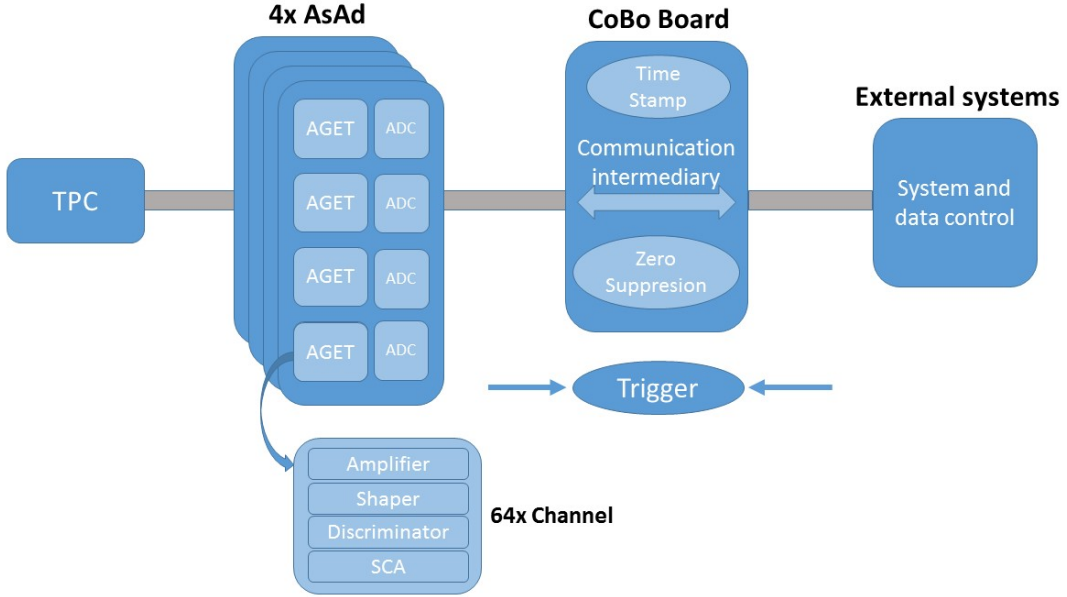


Figure 3.6: *Schematic representation of the GET system.*

transmitted via the Concentration Board (CoBo) to external systems where the data are processed and analyzed. Information is also travelling the other way. The settings for the AsAd are controlled from outside and are passed on via the CoBo. The CoBo acts, so to speak, as a communication intermediary between the AsAd and the world outside.

The CoBo is connected to four AsAd cards, each one hosting four AGET chips. An AGET chip contains 64 channels, which each receive the signal from one detector pad. So, in total one CoBo is responsible for 1024 channels. The main components of a channel are a charge-sensitive amplifier (CSA), an analog filter, a discriminator and an analog memory.

The CSA converts the signal from charge to voltage with a variable gain such that dynamic ranges of 10^3 can be achieved. Afterwards the signal is shaped in the analog filter and sent to the analog memory, which is based on a Switched Capacitor Array (SCA) structure. The SCA is a storage device that saves the analog signal until it can be read out by the ADC. It consists of a circular buffer with 512 cells in which the signal is constantly sampled and stored. The sampling frequency can vary from 1 to 100 MHz; in this experiment the total information stored in the 512 samples of the buffer corresponds to $10 \mu\text{s}$. Once a trigger is received, the sampler is stopped and the stored signal is sent to the ADC to be digitized.

For the system to be triggered, the signal must exceed a certain minimal value. This condition is tested for each channel in the channel discriminator. The amplitude of

the shaped signal is compared with a programmable threshold value. If the threshold is crossed the discriminator sends out a logical signal equal to 1 (0 otherwise). These logical signals of all 64 channels are summed up to form a multiplicity trigger signal. The amplitude of the trigger signal is equal to the number of hit channels on the AGET and is called the trigger multiplicity. The trigger can also be set on the micromesh; in this case the trigger is satisfied when the total amount of charge collected on the mesh is higher than a threshold value.

The demonstrator set-up uses a small-scaled version of the GET electronics with 4 concentration boards. This amounts to a total of 4096 channels. CoBo 0 and CoBo 1 are responsible for the 2048 channels of the pad plane. The four DSSDs are connected to CoBo 2. Since each DSSD has 64 detector strips, a total of 256 channels is needed. They fit together on one AsAd card. The Maya detectors occupy only 12 channels on CoBo 3. The detector-electronics connections are summarized in Table 3.1.

Table 3.1: *The number of channels and electronic connections of the different detectors of the ACTAR TPC.*

Detector		# channels	Location
Pad plane	left side	1024	CoBo 0
	right side	1024	CoBo 1
DSSDs	1+2 p-side	64	CoBo 2 AsAd 0 AGET 0
	3+4 p-side	64	CoBo 2 AsAd 0 AGET 1
	1+3 n-side	64	CoBo 2 AsAd 0 AGET 2
	2+4 n-side	64	CoBo 2 AsAd 0 AGET 3
Maya-Si	left	6	CoBo 3 Asad 0 AGET 0
	right	6	CoBo 3 Asad 0 AGET 3

3.2 Physics of the ^{12}C experiment

For our experiment, a ^{12}C ion beam is produced by the Tandem accelerator at an energy of 80 MeV. The gas medium in the ACTAR TPC chamber consists of a mixture of 90% helium (He) and 10% isobutane (C_4H_{10}). The polyatomic isobutane molecules act as a quencher. They absorb the photons created from de-excitations to prevent them from causing additional ionizations that might lead to too many free electrons. The pressure inside the chamber is maintained constant at a value of ~ 1 atm, resulting in a density of 0.391 mg/cm³ at room temperature.

3.2.1 Expected reactions

The incoming ^{12}C ion has the possibility to interact with one of the three atoms that constitute the target: ^{12}C , ^4He (or α) and H (or p for proton). All target atoms are lighter or as light as the ^{12}C projectile, which means we are mostly in the case of inverse kinematics. The different nuclear reactions that can take place are summarized in Table 3.2. ^{12}C can scatter elastically and inelastically on all three target atoms.

Table 3.2: *The possible nuclear reactions of the ^{12}C beam with the $\text{He:C}_4\text{H}_{10}$ target mixture.*

Target nu- cleus	A	Z	relative # atoms	CM energy (MeV)	Reactions	Q-value (MeV)
^{12}C	12	6	0.17	40	$^{12}\text{C}(^{12}\text{C},^{12}\text{C})^{12}\text{C}^{(*)}$ $^{12}\text{C}(^{12}\text{C},^{12}\text{C})3\alpha$	0, -4.4 - Hoyle energy
^4He	4	2	0.38	20	$^{12}\text{C}(\alpha,\alpha)^{12}\text{C}^{(*)}$ $^{12}\text{C}(\alpha,\alpha)3\alpha$	0, -4.4 - Hoyle energy
p	1	1	0.45	6.2	$^{12}\text{C}(\alpha,^3\text{He})^{13}\text{C}$ $^{12}\text{C}(\text{p},\text{p})^{12}\text{C}^{(*)}$	-15.6 0, -4.4

In elastic scattering both energy and mass are conserved and the Q-value is equal to zero. For inelastic scattering part of the beam kinetic energy is needed to excite the final nucleus. The Q-value is exactly equal to the excitation energy of the state that is populated. To reach one of the cluster states in ^{12}C a minimal excitation energy of 7.27 MeV, equal to the energy of the 3α break-up threshold, is required. Both the ^{12}C - ^{12}C and ^{12}C - α reaction channels have a sufficient CM energy to allow the formation of the Hoyle state or one of its band members at higher energy. Such a reaction is followed by the immediate break-up of the excited ^{12}C in three α -particles, and is therefore referred to as a break-up reaction. The CM energy of ^{12}C scattering on p is only high enough to reach the first excited state of ^{12}C at an energy of 4.4 MeV. Apart from the scattering processes, a transfer reaction between ^{12}C and ^4He is also possible. The ^4He

nucleus transfers one of its neutrons to ^{12}C , resulting in the formation of ^{13}C and ^3He . Because of the high negative Q-value this reaction will be less probable.

3.2.2 Reaction kinematics

The fact that we're working with inverse kinematics doesn't imply any change in the physics of the reaction we want to study with respect to direct kinematics. In the center of mass the two are completely equivalent, it is only in the laboratory frame that significant changes occur.

In direct kinematics, where a light projectile is fired upon a heavy target, the light ejectile can be scattered in all directions ($0 - 180^\circ$). In inverse kinematics however, the large amount of momentum carried by the heavy projectile forces the reaction products to more forward angles. This is advantageous in view of efficiency because particles scattered in the forward hemisphere will be most easily detected by the Si detectors in our set-up. Also the energy with which the reaction products emerge is different: the light He and p nuclei can recoil with very little energy at large scattering angles.

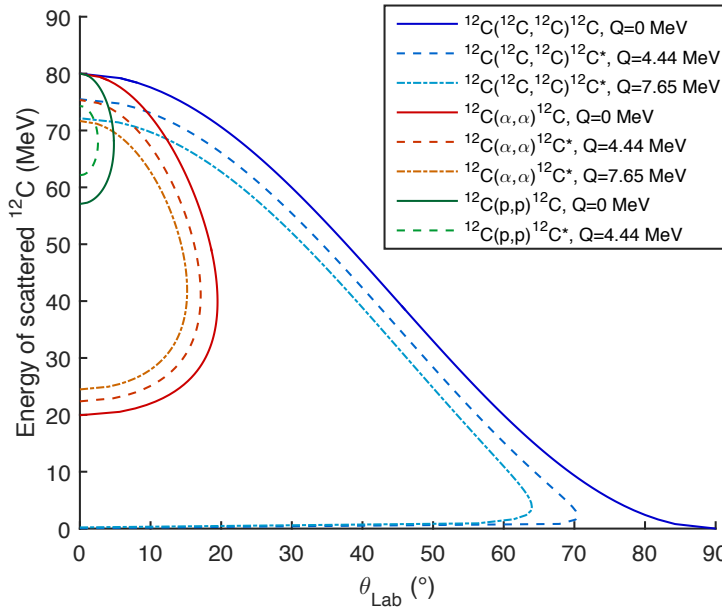


Figure 3.7: Energy of the scattered ^{12}C nucleus as a function of lab angle for the different elastic and inelastic reactions for a beam energy of 80 MeV. The double-valued solution for some lab angles is a particular feature of inverse kinematics. Obtained with Catkin [60].

Figure 3.7 shows the kinematics of the different elastic and inelastic reactions that take place. The energy of the scattered ^{12}C beam particle is plotted against its angle in the LAB frame. We see that at certain LAB angles, the outgoing ^{12}C ion has two possible values of its energy. This is a feature that arises for inverse kinematics. The maximum

scattering angle is highly dependent on the mass of the target atom the ^{12}C has reacted with. In the case of He or p scattering the ^{12}C is highly focused at forward angles. It will be detected by the DSSDs on the front wall of the chamber if it escapes the gas volume. In the more symmetric C-C scattering events, the maximum angle can go up to $\sim 65^\circ$ in case of Hoyle excitation and up to 90° in case of elastic scattering. The ^{12}C has a high chance to be detected by the sideways Maya detectors.

In Figure 3.8 the kinematics of ^{12}C , α and p, as reaction products of elastic scattering are compared. Common to all three is a strong decrease in energy with scattering angle up to the maximal scattering angle of 90° . For higher Q-value reactions there is less kinetic energy available after the reaction. As a result the curves will shift down in energy and the maximal scattering angle will decrease (as already shown in Figure 3.7).

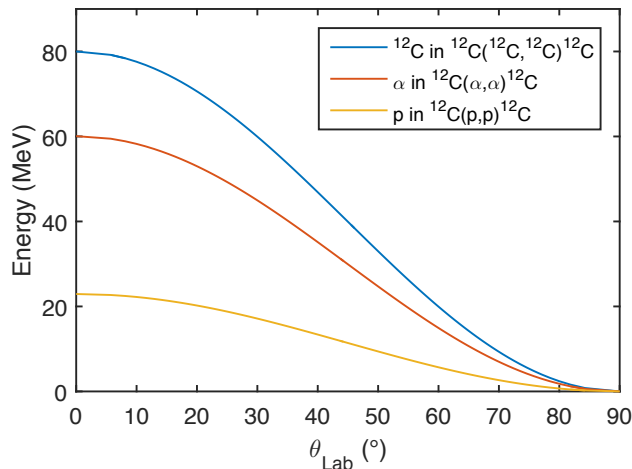


Figure 3.8: *Energy of the reaction products, ^{12}C , α and p, as a function of lab angle in the case of elastic scattering with a ^{12}C beam energy of 80 MeV. Obtained with Catkin [60].*

3.2.3 Energy loss in the He: C_4H_{10} gas mixture

The ^{12}C beam ions that enter the He: C_4H_{10} gas volume will lose energy due to interactions with the gas atoms as described in section 2.2. As a result the beam energy is not constant but degrades from 80 MeV to about 50 MeV at the end of the chamber. Hence, the energy available in the reaction varies with the reaction vertex position. For the reacted particles, which also lose energy along their path, it depends on the type of reaction and the outgoing angle whether they will reach the Si detectors. In Table 3.3 some ranges of ^{12}C , α and p in the He: C_4H_{10} gas composition are tabulated. The significantly higher energy loss of carbon with respect to helium and protons, which was illustrated in Figure 2.3, translates into much smaller ranges for carbon. The first row gives the range for each of the particles at their maximal possible energy. These

Table 3.3: Some ranges of ^{12}C , α and p in the $He:C_4H_{10}$ gas composition.

^{12}C		α		p	
E (MeV)	Range	E (MeV)	Range	E (MeV)	Range
80	47.4 cm	60	5.96 m	20	10.07 m
50	22.1 cm	10	24.8 cm	2.5	24.5 cm
30	10.3 cm	6	10.6 cm	1.5	10.0 cm

ranges largely exceed the length of the chamber (24 cm). Therefore, looking back at the kinematics in Figure 3.8, small-angle large-energy scattered particles are always expected to reach the forward placed DSSDs. The following rows give the energies of the particles at which their range becomes comparable to the chamber's dimensions. For each of the particles these energies only result from scattering at quite large LAB angles (see Figure 3.8). Overall the majority of the reaction products is expected to reach the detector walls and thus the Si detectors. For reactions with higher (more negative) Q-values or a reaction vertex further in the gas the probability for particles to be stopped in the gas will of course increase, especially in the case of carbon.

Chapter 4

Data Analysis

The data were gathered by performing beam runs of approximately one hour over a period of 3 days. In switching from one run to the next, changes in the set-up parameters could be done to optimize the set-up. For example, the mesh and cathode voltages, the Bacchus settings and the type of trigger are varied during the experiment. The data can be divided into three big sets of runs according to the above-mentioned settings (see Table 4.1). Data set 1 can be regarded as the ‘trial’ stage; it contains a lot of changes in the detectors settings to find the optimal working conditions of the detection system. We chose to focus the data analysis on set 3 because it contains the largest amount of data with the same settings to be summed and it has the trigger on all three detectors such that all kinds of events are included. Due to instabilities of the acquisition system some of the runs are shorter than the foreseen time of one hour. Calibration runs were also performed for the different detectors before, during and after the experiment. The analysis is carried out using MVisu, a specific data processing package based on ROOT [61], a data analysis framework developed by CERN.

4.1 Signal processing

Trigger and event building

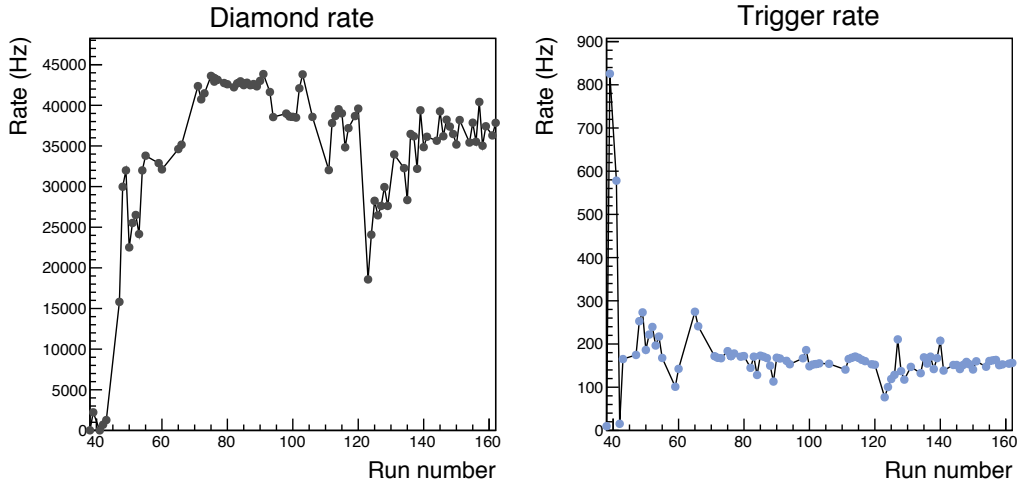
The trigger condition in the GET electronics determines when a physical event of interest has taken place. In our case such an event would be a nuclear reaction between the beam and one of the target atoms. For data set 3 (see Table 4.1), when a trigger is received in either one of the three detectors (DSSD, Maya or mesh) an event will start to build. For data sets 1 and 2, the mesh signal is excluded from the trigger and a hit signal in one of the Si detectors is necessary. Once the trigger condition is satisfied, the read-out of the AGET signals stored in the SCA structures starts. For each trigger, an event is created containing the information of all CoBos and their AGETs.

In Figure 4.1 the trigger rate and count rate in the diamond detector are summarized for all data runs. The particles reaching the diamond are mostly unreacted beam particles, hence the diamond rate is a reasonable estimate for the beam intensity. Overall, the

Table 4.1: *Data summary: Three big sets of runs can be distinguished.*

	Runs	Trigger	Bacchus settings	Mesh voltage	Cathode voltage
Set 1	38-66	DSSD or Maya	Selecting $^{12}\text{C}(5^+)$ Dipole slits at 5 mm	-420 to -430 V	-2000 to -2500 V
Set 2	73-106	DSSD or Maya	Selecting $^{12}\text{C}(6^+)$ Dipole slits at 2 and 5 mm	-410 V	-2500 V
Set 3	106-162	DSSD or Maya + mesh	Selecting $^{12}\text{C}(6^+)$ Dipole slits at 2 and 5 mm	-410 V	-2500 V

trigger and diamond rate are quite constant over the whole set of data runs (within an order of magnitude). The trigger rate amounts to about 150 Hz, which results in approximately $5.4 \cdot 10^5$ events per hour. Only for the first few runs, the values differ significantly due to a strong misalignment of the beam. Beam particles are missing the diamond detector and instead are hitting the DSSD. As a result the beam is triggering the electronics, however no reaction event has taken place.

Figure 4.1: *Diamond and trigger rates summarized for all the data runs.*

Baseline subtraction

Due to electronic noise, the GET signal is superimposed on a electronic background which is referred to as the baseline. To retrieve the exact height of the signal this baseline needs to be subtracted in some way. There are different ways to proceed and depending on the signal shape the best method will be selected. For the signals on the front strips of the DSSDs a linear baseline subtraction is needed because of the

anomalous decreasing trend of the baseline. The baseline average of 100 samples right before and right after the peak are taken (see Figure 4.2a). With these values (y_1 and y_2) a linear background is constructed between the points x_1 and x_2 , which is subtracted from the signal. For the back DSSD signals this method is not appropriate because of an undershoot in the signal right after the peak, as visible in Figure 4.2b. Therefore an average baseline subtraction is used, where the average is taken in the pre-peak region (first 180 samples). The obtained value is subtracted from the peak maximum to get the real signal height. The signal of the Maya detectors is similar to that of the front DSSDs, except that the baseline is typically much more unstable, as illustrated in Figure 4.3a. Therefore the same linear subtraction method is used to take care of the baseline, but the range for the averages is extended to 180 samples to get a better averaging over the instabilities. An example of a signal on the pads is given in Figure 4.3b. A baseline is absent here, so the peak maximum is used directly. For the pads the timing of the signal is of great importance to reconstruct the vertical dimension of the tracks. The position of the peak maximum is used to assign a time to the signal.

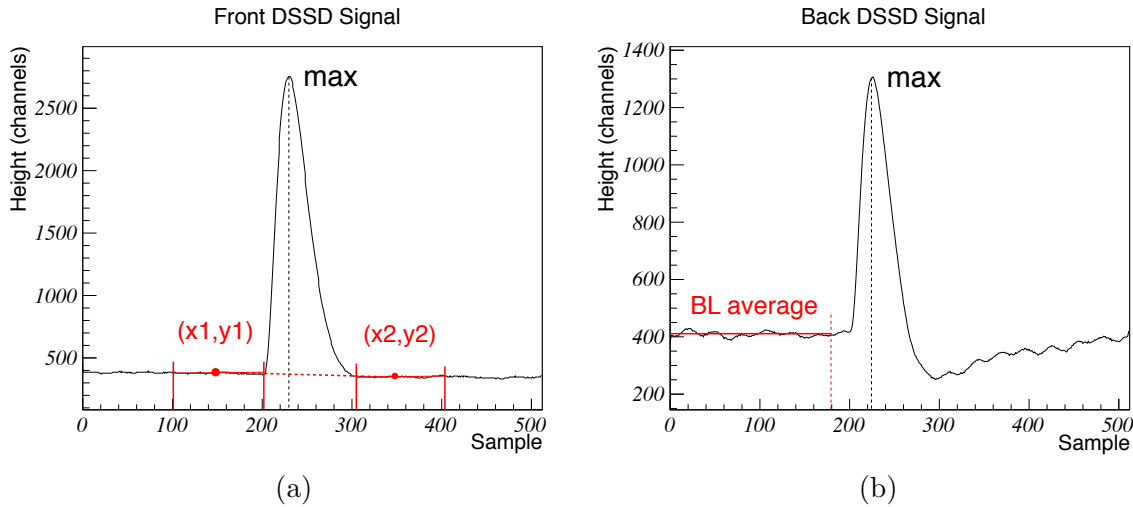


Figure 4.2: Examples of a signal in (a) one of the front and (b) one of the back strips of the DSSDs. For the front signal a linear baseline constructed from an average before and after the signal peak is subtracted. Due to the undershoot in the back signal, only the average baseline from before the peak is calculated and subtracted from the signal.

As a means of comparison, a calibration of the front DSSD strips was carried out three times, each time treating the baseline in a different way. The obtained strip resolutions for DSSD 4 are put together in Figure 4.4 for a calibration without baseline subtraction, with an average baseline subtraction and with a linear baseline subtraction. The linear subtraction method is clearly superior to the average subtraction. On average it offers an improvement of the resolution by about 1 channel. Because of variations in the baseline level, we would expect removal of the baseline to globally result in a better resolution. Apparently this is not the case: for some strips there is an improvement,

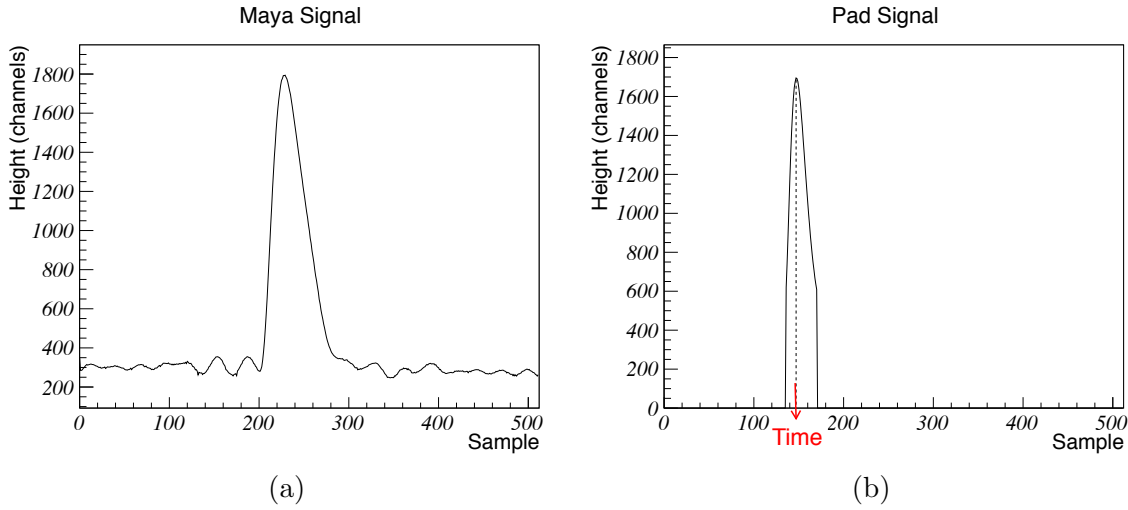


Figure 4.3: (a) Example of a signal in Maya. The baseline shows some variations. (b) Example of a signal in the pads, for which a baseline is absent. For the time of the signal, the value where the maximum of the peak occurs is used.

for others a deterioration, but overall there isn't really a positive effect.

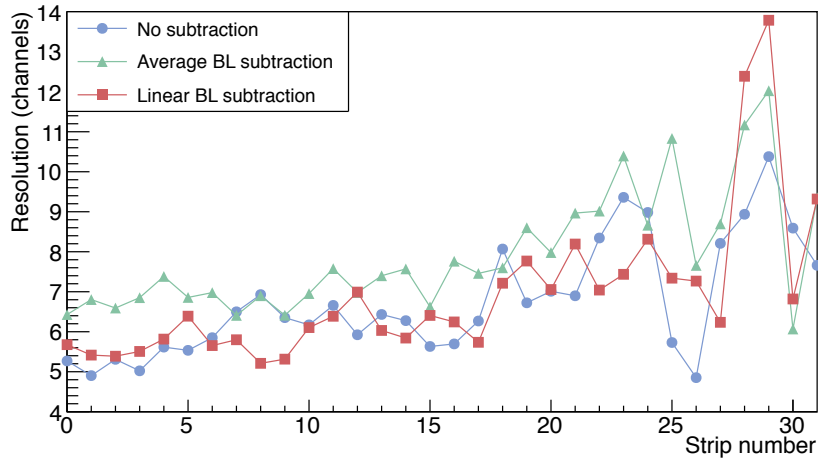


Figure 4.4: A comparison of the DSSD resolution for different ways of handling the baseline. The errors bars have been omitted for clarity.

Saturation problem

A significant amount of the recorded signals is saturating the electronics. The saturation originates in the analog to digital conversion of the signal. The input acceptance of the 12-bit ADC that is used, is limited to a maximum value. Consequently, signals that are exceeding this value and entering the ADC will be truncated to the maximum allowed value. As a result these signals appear as if their peak is chopped off to a flat

plateau.

The maximum of these signals can not be trusted as the actual energy value. Hence in the further analysis the energy information of saturated signals will be ignored, however the fact that there is a hit on the particular DSSD strip or Maya detector can be used. As a result of the saturation, the maximum energies that can be measured in the DSSDs and Mayas are respectively ~ 21 MeV and ~ 25 MeV. The amount of saturation in the different Si detectors is expressed in Table 4.2 as a percentage of the total amount of hit signals in the respective detectors.

Table 4.2: *Saturation rates in the different Si detectors (based on runs 111-116).*

DSSD 1	15.6 %
DSSD 2	13.9 %
DSSD 3	14.2 %
DSSD 4	13.4 %
Maya Left	6.1 %
Maya Right	6.5 %

4.2 Calibration of the detectors

To convert the signal heights in channels to a value in energy, a calibration of the different detectors is necessary.

4.2.1 Silicon detectors calibration

The energy calibration of the silicon wall detectors was performed by mounting a radioactive α -source inside the chamber. The source consisted of a mixture of three α -emitters of which the α -energies of their main decay branches are well known and summarized in Table 4.3. The chamber was kept under vacuum to make sure the alpha particles deposit their total energy in the Si detectors. In the ideal case each of the α -particles produces a Gaussian-shaped peak in the energy spectrum. In reality however, a low-energy tail is observed due to incomplete charge collection events¹. To

¹As the emitted alpha travels through the source material before escaping, it loses part of its energy.

Table 4.3: *Decay energies of the α -emitters present in the source.*

Isotope	α energy (MeV)
^{239}Pu	5.1566
^{241}Am	5.486
^{244}Cm	5.8048

take this effect into account, G. Bortels and P. Collaers [62] proposed a convolution of a Gaussian with a left-sided exponential as the best representation. In our case, the spectrum contains three peaks and the fitting function can be written as

$$F(u) = \sum_{i=1}^3 \frac{A_i}{2} \left\{ \left(\frac{1-\eta}{\tau_1} \right) \exp \left(\frac{u-\mu_i}{\tau_1} + \frac{\sigma^2}{2\tau_1^2} \right) \operatorname{erfc} \left[\frac{1}{\sqrt{2}} \left(\frac{u-\mu_i}{\sigma} + \frac{\sigma}{\tau_1} \right) \right], \right. \\ \left. + \frac{\eta}{\tau_2} \exp \left(\frac{u-\mu_i}{\tau_2} + \frac{\sigma^2}{2\tau_2^2} \right) \operatorname{erfc} \left[\frac{1}{\sqrt{2}} \left(\frac{u-\mu_i}{\sigma} + \frac{\sigma}{\tau_2} \right) \right] \right\} \quad (4.1)$$

This gives a total of 10 parameters that are varied in the fitting procedure. The mean of each peak μ_i is estimated as the most probable value of the channel/energy. The value of σ is related to the FWHM (Full Width Half Max) of the peaks as $\sigma \approx \text{FWHM}/2.355$ and is a measure for the energy resolution of the detector. The remaining parameters represent the area under each peak, A_i , two exponential lifetime parameters, τ_1 and τ_2 , and a weight factor, η .

For the calibration of the DSSDs the source was placed on the back of the diamond detector. In this way it is facing the DSSD wall at a distance of approximately 2 cm. The measured spectrum with the three peaks is shown in Figure 4.5 for a front and back strip on DSSD 2. The calibration is carried out by plotting the tabulated energy values (Table 4.3) versus the peak positions. A linear curve can be fitted to the points and provides us the channel-to-energy conversion coefficients. For the particular strip plotted in Figure 4.5a the obtained relation is

$$\text{Energy (keV)} = 5.28(\pm 0.01) \cdot \text{Channel} + 238(\pm 11). \quad (4.2)$$

For each of the 32 front and 32 back strips of each of the 4 DSSDs a separate calibration is performed, of which the parameters are tabulated in Appendix A.1. The differences in the energy spectra as measured by the front and back detector strips are striking, as one can see in Figure 4.5. In the front strip spectrum the peaks are sharper and have more counts. On the back strip the low-energy background is much higher. The exponential tail part of our fitting function is much more pronounced and is necessary to produce a good fit. The better signal to noise ratio in the front strip spectrum allows a more accurate fit, resulting in a more precise energy calibration. Therefore the energy values as measured by the front strips will be used in the analysis.

As mentioned before, the width of the peaks is a measure of the resolution σ of the detector. A value for the resolution expressed in channels is provided by the peak-shape fit. Using the calibration parameters this value can be converted to energy units. In Figure 4.6 the energy resolution and the error for all the strip detectors on the different DSSDs are collected. The vertical front strips are numbered from 0 to 31 and the horizontal back strips from 32 to 63 (see Figure 4.6a). Common to all four DSSDs is an ascending trend in resolution as the strip number increases, both for the front and back detectors. This can be explained by the fact that the source is located on the back of the diamond detector, which sits in the center of the DSSD configuration.

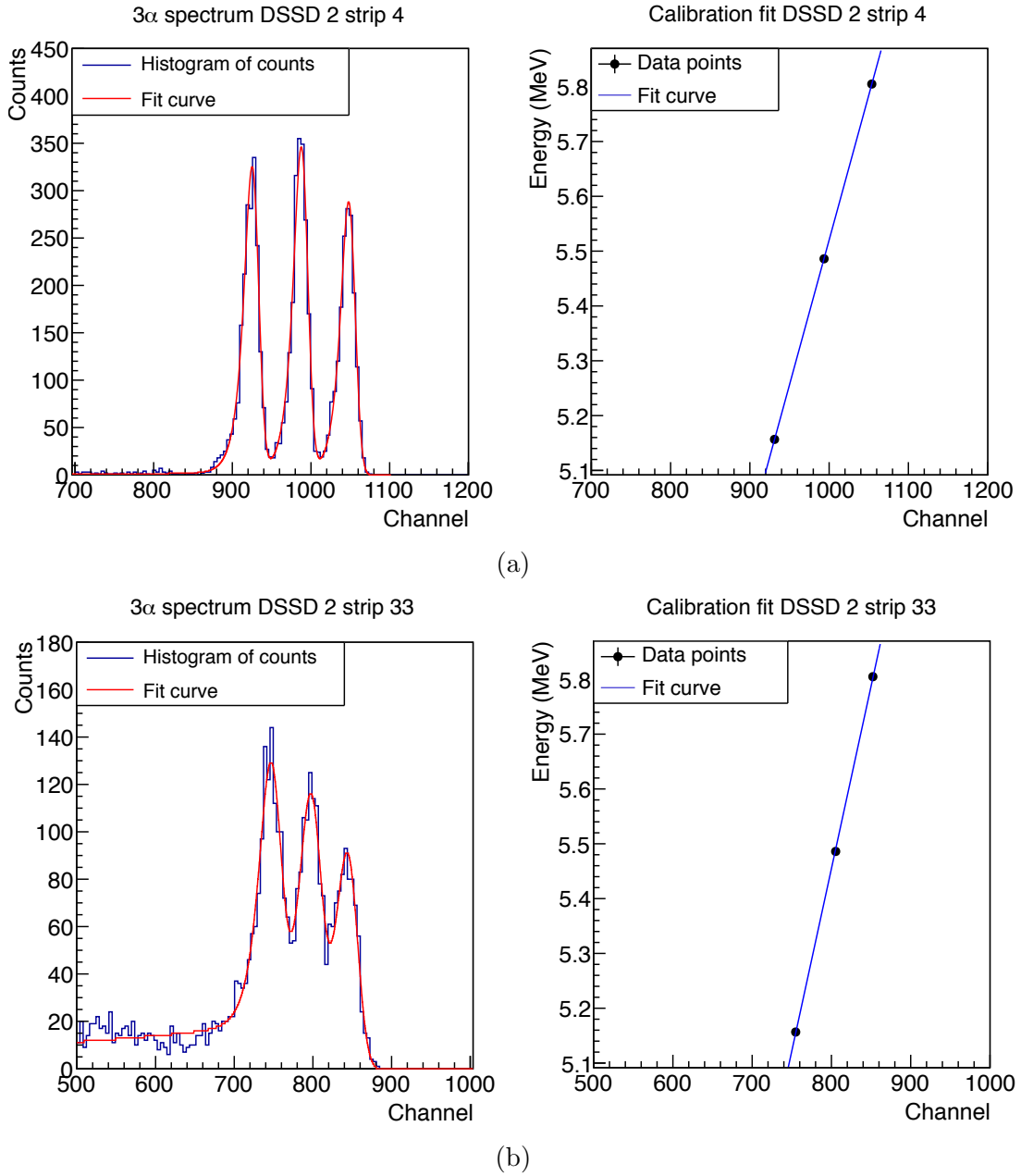


Figure 4.5: (a) In the left figure the source energy spectrum is shown as measured by one of the front strips on DSSD 2. The three peaks of the different α energies are clearly visible. The red curve is the Gaussian \otimes Exp fit to the histogram. On the right the α energies from Table 4.3 are plotted against the mean channel of each peak (as obtained from the fit). The slope and intercept of the blue linear fit curve determine the calibration of this particular strip. (b) The same is plotted for one of the back strips on DSSD 2. Worse resolution and more background is immediately noticeable. The error bars on the channel values are calculated as σ/\sqrt{N} but in both cases they are too small (< 1 channel) to be visible (with N the number of counts under the peak).

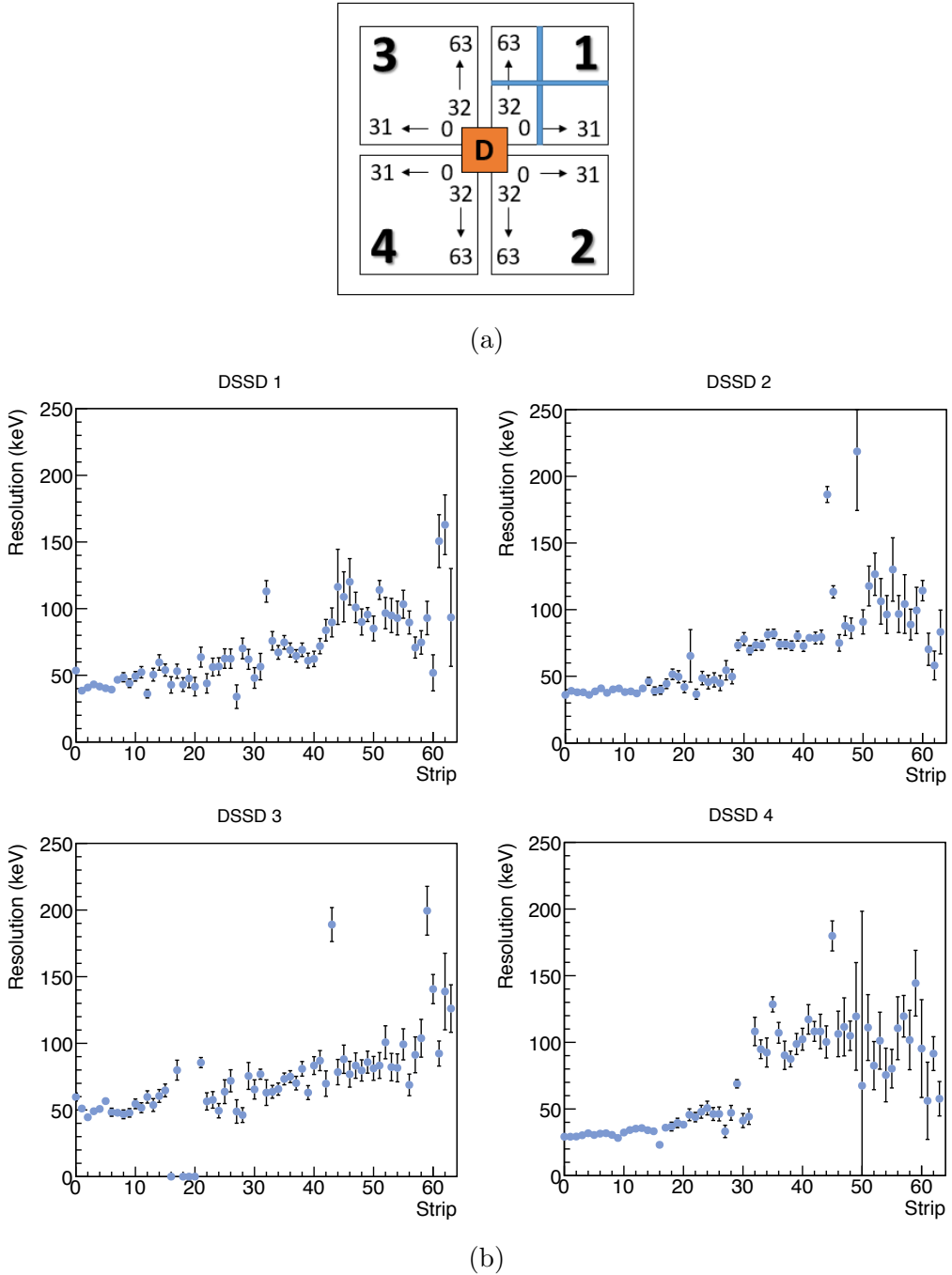


Figure 4.6: (a) Numbering and ordering of the DSSDs and its detector strips. The vertical front strips are numbered from 0 to 31 and the horizontal back strips from 32 to 63. The source is located on the back of the diamond detector, which is represented by the orange square in the middle. (b) Energy resolution (in keV) of the 64 strips on each of the four double-sided silicon detectors.

The strips closest to the center will receive the most α -particles and thus have more statistics. In addition, the shallow angle of incidence of α -particles traveling towards

the outer strips, increase the possibility of penetrating two adjacent strips. In this case the full energy is divided between the two strips and they both get a low-energy background count. Also striking is the significant worse energy resolution on the back strips of the DSSDs. Especially for the most outer strips, which sometimes have only a few hundreds counts in total, the peaks were hard to identify and fit. That's also why you see an increase in error bar as the strip number increases.

For the calibration of the Maya detectors the source was attached to the top center of the chamber. Two Maya calibration runs were performed, one with the source facing Maya left, the other one with the source facing Maya right. The same calibration procedure is followed for the 12 Maya silicon detectors as in the case of the DSSDs (see Appendix A.2). Only the exponential tail was removed from the fitting function because the Gaussian shapes were sufficient to reproduce the spectra well. Figure 4.7 shows an energy spectrum of one of the Mayas on the left and a summary of the energy resolution on the right. The Maya detectors are numbered in such a way that 0 corresponds to the bottom most upstream one and 5 to the upper most downstream one. For all of them the energy resolution lies around 70-80 keV.

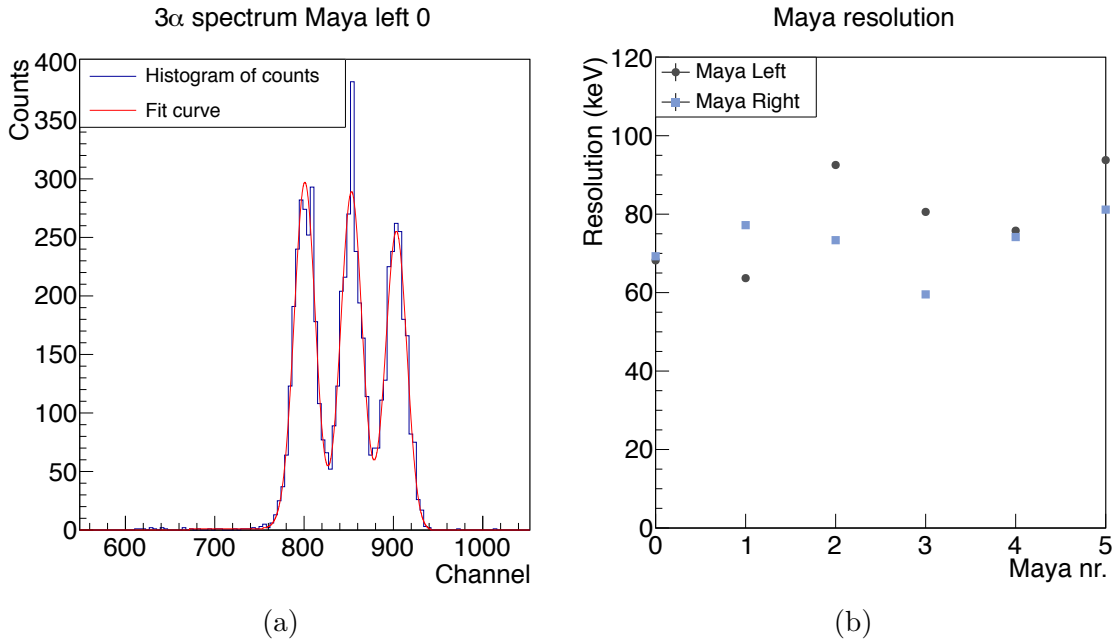


Figure 4.7: *Maya calibration.* (a) *Fitted energy spectrum as measured by one of the left Maya-Si pads.* (b) *Energy resolution (in keV) of the left and right Maya detectors.* The error bars are too small to be visible.

4.2.2 Pad alignment

The channels of the 2048 pads on the pad plane are not converted to energy, but it is sufficient to align them with respect to one reference pad. The absolute pad signals are

not of importance, only the relative signals on the different pads need to be considered.

The alignment of the pads is carried out by applying a pulser signal to the micromesh. A pulser delivers electronic pulses of variable height at a frequency of 1.5 Hz. The pulses are negatively polarized and have a sharp rise time of 20 ns. The pulser is set to six different heights, each of which is applied for a time of two minutes. The mesh and pad plane act as a capacitor and the induced charge on the pad detectors is read out. This results in a six peak pulse spectrum as shown in Figure 4.8. The exact positions of the peaks are determined by six Gaussian fits. One of the pads is chosen as reference pad and its peak positions are used as reference values, in analogy to the α energy values in the Si calibrations. For each of the 2048 pads, the peak positions are plotted to the reference values and a linear fit is carried out to complete the alignment process.

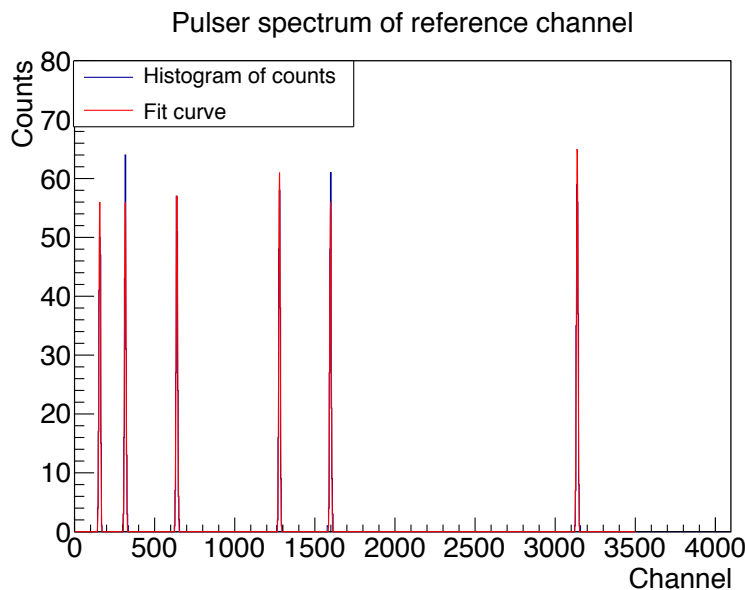


Figure 4.8: *Pulser spectrum of the reference pad (nr. 226).* The 6 peaks correspond to the 6 pulse heights that were applied each for a time of 2 minutes at a frequency of 1.5 Hz.

One of the AGETs on CoBo 1 was found to be defective, resulting in the loss of the signal of 64 pads. These pads make up a region of $8 \times 32 \text{ mm}^2$, which is located in the right upper corner of the pad plane (looking upstream the beam direction, see white corner in Figure 4.12).

4.3 Event reconstruction

For each of the channels on all AGETs, it is checked if the signal exceeds a threshold value. If it is the case, a hit is registered on that channel. After calibrating the

DSSD and Maya signals to energy and aligning the signals on the pads, the relevant information is stored per event. For DSSD and Maya hits, the deposited energy and the exact strip or pad on which the hit was recorded are saved. For each of the pads which receive a sufficient signal, the deposited charge (in channels) and the time of arrival is stored.

Determination of the reaction vertex

From the pad information the tracks left by the charged particles can be reconstructed in three dimensions. The pattern of fired pads reveals the 2D projection of the tracks on the bottom xy-plane. The time of arrival of the signal on each pad is a measure for the vertical distance the electrons had to travel to reach the mesh. Hence, with an estimated drift velocity² of 25.5 mm/ μ s the time can be converted to an exact vertical coordinate. An example of the visualization of a reaction event is shown in Figure 4.9. The ^{12}C beam is coming in from the left. Four tracks can be distinguished, all tracing back to the same reaction vertex. The point of origin of the reaction is cut out because of the aluminum mask shielding the middle of the pad plane. The energy loss along each track is visualized with the help of a color scale.

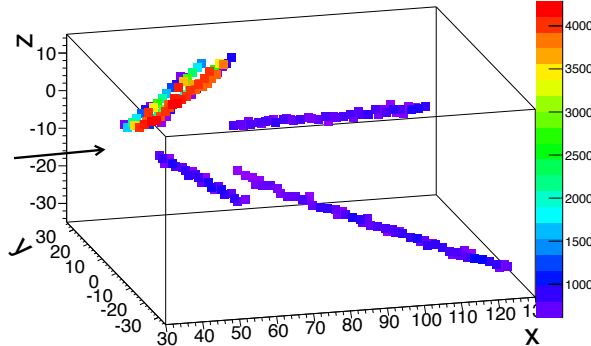


Figure 4.9: Three-dimensional track reconstruction of a reaction event with dimensions given in mm. The arrow represents the incoming ^{12}C beam. The colors indicate the amount of charge deposition along the tracks.

To determine the exact vertex position of the reaction each of the tracks is fitted to a straight line. The fitting procedure is based on the 3D linear regression method described in [63] and minimizes the sum of the squares of the orthogonal distances. The centres of the pads are used as the x- and y-coordinates, and for the z-coordinates the time values are used. Each of the points is weighted with the amount of charge deposition on the corresponding pad to get the most accurate fit.

²From the hit position in the DSSD we know the vertical distance z the particle has traversed. From the timing information on the pads the time difference Δt between the beginning and end of the track can be determined. The drift velocity is then estimated by $v_d = z/\Delta t$.

Since the left and right part of the pad plane³ are separated by the aluminum mask, tracks going to left and right are easily fitted separately. However when two or more particles are traveling in the same direction, the assignment of the fired pads to a track is not trivial. In this case there are two ways in which the tracks can be discriminated from each other. Either a timing difference between the tracks or the amount of non-fired pads in between the tracks can be used. For each of these cases an example is shown in Figure 4.10. To visualize the events in a proper way, the xy- and xz-projection of the deposited charge and the xy-projection of the time on the pads are shown respectively from left to right. In the upper event, the two tracks on the right slightly overlap and from the charge deposition we can't say which pads belong to which track. Though, the time projection clearly shows the difference between the tracks by their color, due to their separation in the z-direction. In this way the energy loss due to the two particles can be distinguished. In the second event the timing of

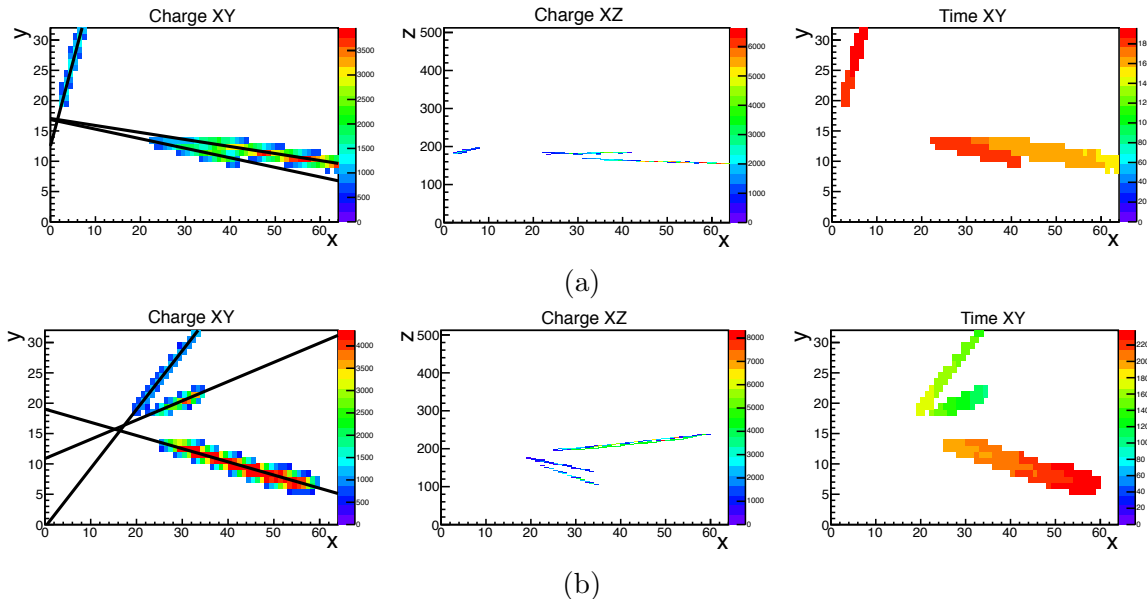


Figure 4.10: *Two examples of reaction events, visualized by plotting the xy- and xz-projection of the deposited charge and the xy-projection of the time on the pads, respectively from left to right. The beam is every time coming in from the left. On the left plots the projections of the fit lines are added. In (a) the tracks are differentiated on their timing difference, while in (b) the tracks are differentiated by the gap that is opening up in between.*

the two tracks on the left is almost the same, so they can't be distinguished on this. However, here the tracks separate as they move further away from the vertex point. The gap forming between the two tracks can in this case be used to assign the right charges to the right tracks. The general fitting algorithm is implemented with these two methods of discriminating between tracks. For most events this algorithm gives a

³Left and right with respect to the beam direction. In the xy projections, particles traveling to the left appear in the upper part, particles traveling to the right in the lower part.

good fit result, like the ones in Figure 4.10 where the fit lines intersect at one point. Only a portion of 1% of events do not allow a good fit. The “goodness” of the fit is checked by the mean quadratic distance⁴ δ_m between the data and the fit lines; if it is higher than a certain value, the fit is assumed not accurate enough and the event is thrown away. This is mainly the case for events with high overlap between the tracks both in the x and the z direction.

If the fit is accepted based on the δ_m value, the vertex position of the reaction is determined as the intersection point of the fitted tracks. For more than two tracks the means of the x-, y- and z-coordinates of the intersection points between each pair of fit lines is taken. If the reaction vertex is located outside the chamber’s dimensions, the event is not used in the further analysis.

It is possible that after the system is triggered a second event is recorded within the same event acquisition window. In this case the tracks that are visible on the pad plane belong to two different events. Most of the times, this second event is just a beam particle that is deviating and coming out of the masked region. Because these secondary tracks are not originating from the same vertex as the primary event, they can be traced on the basis of this and removed from the event.

Track multiplicity

Once the ‘bad’ events - events that can’t be fitted properly, don’t have a well defined vertex position or do not reproduce a physical reaction⁵ - have been discarded, about 80 % of total events remain. The track multiplicity histogram in Figure 4.11 indicates that for the biggest part of the events no or just one track is observed. In the case

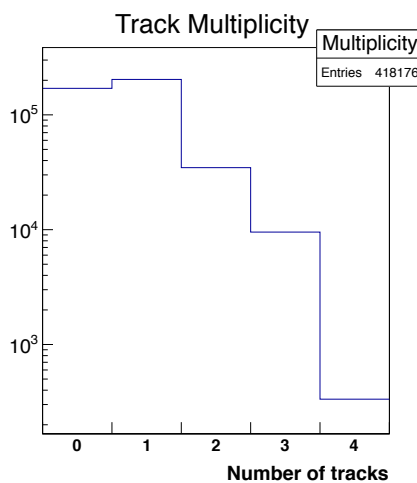


Figure 4.11: *Histogram of track multiplicities in run 114.*

⁴A good fit typically has a δ_m value close to or lower than 1 pad.

⁵For example an event with two tracks emerging to the left and none to the right does not conserve linear momentum and is thus not a physically possible reaction.

of no tracks the electronics must have been triggered solely by a hit in one of the Si detectors. This is understandable as the pad plane is not covering the full bottom of the chamber. The huge amount of events with track multiplicity 1 is striking. They can possibly be explained by beam particles coming out of the masked beam region, or resulting from a reaction where the other reaction products are shielded by the mask or don't reach the pad plane. This will be analysed in more detail later. As the track multiplicity increases the amount of events gets scarcer. For track multiplicity 4 there are only a few hundred events per run. In principle none of the possible reaction channels would result in 3 reaction products. Hence, the multiplicity 3 events must be actual multiplicity 4 events with one of the particles shielded. It's also possible that two particles are travelling very close together and their tracks are fitted as one.

Correcting the beam misalignment

From the total amount of accumulated charge on the pads, shown in Figure 4.12, an asymmetry with respect to the central beam direction can be noticed. This indicates that the beam is not perfectly aligned with respect to the chamber and this needs to be taken into account in the analysis. The angles of the outgoing particles as determined from the fit need a correction to compensate for this. To estimate the

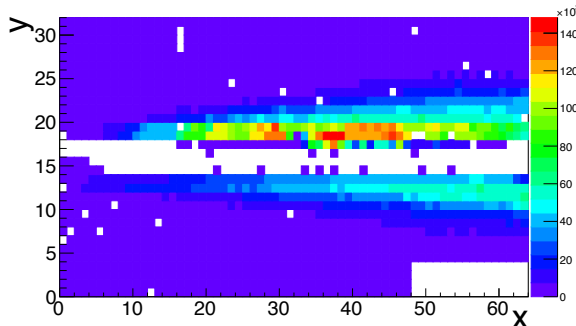


Figure 4.12: *Accumulated charge on the pads off all events in run 116. From the charge distribution a misalignment of the beam slightly to the left can be deduced. The pads in the middle of the plane are shielded by an aluminum mask.*

beam misalignment, a look is taken at the distribution of hits on the DSSD strips from saturated signals. These saturated signals can be induced either by direct beam particles or small-angle high-energy scattered ^{12}C or α . In both cases the hits will have a distribution around the beam impact point. The horizontal and vertical strips can be converted to corresponding angles in the xy and xz plane. We will refer to these angles as η and φ respectively. The distribution of hits as a function of these angles are shown in Figure 4.13 for run 116. The mean values of a Gaussian fit to the histograms gives an estimate for the misalignment of the beam. For this particular run, we find $\bar{\eta} = (0.08 \pm 0.01)^\circ$ and $\bar{\varphi} = (-0.34 \pm 0.01)^\circ$, indicating a slight misalignment of the beam down and to the left. This estimation is repeated every few runs, to account for small changes in the beam deflection. The corrected angles are now given by $\eta_{\text{cor}} = \eta - \bar{\eta}$ and $\varphi_{\text{cor}} = \varphi - \bar{\varphi}$.

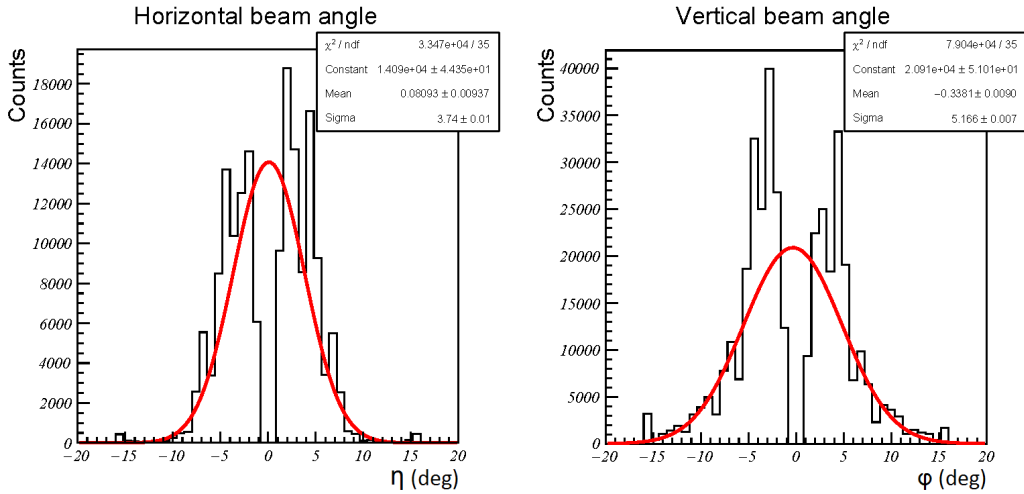


Figure 4.13: *Histograms of saturated DSSD hits on the vertical front strips (left) and the horizontal back strips (right) for run 116. The strip numbers on the x-axis are converted to angles with respect to the chamber entrance. The mean values of the Gaussian fits (red curves) give an estimate of the horizontal and vertical misalignment of the beam.*

4.4 Particle identification

Particle identification is mandatory for the kinematical reconstruction of the events. This is achieved via measuring the particle's energy loss in the gas. In section 3.2.3 we saw that the energy loss of a particle is highly dependent on its Z-value and is thus element specific. Therefore the energy loss along the ionization tracks, as measured on the pad plane, can be used to identify the particle creating it. With the energy information in the Si detectors, we can build the experimental energy loss curves as a function of deposited energy, the so-called E- ΔE spectra. By comparison with the calculated curves the identification will be possible.

Track-Si correlation

Before we can do this, the particle tracks need to be correlated with the signals in the Si detectors. This is done by extrapolating the linear track fits to the position of the detectors and checking if there is a corresponding detector hit, as illustrated in Figure 4.14. For the DSSDs a hit is determined by a front and a back strip with more or less the same energy deposition. There may be some difference due to the error of the calibration. The horizontal and vertical hit coordinates are then known up to 2 mm, the width of a detector strip. In some cases the energy deposited on the back side is divided over two adjacent strips and the mean position of the two is used. In the Maya detectors the hit position is much less accurately known, due to the large pad size of $5 \times 5 \text{ cm}^2$. If the expected hit position calculated from the fit extrapolation coincides up to 1 cm difference with a hit in one the Si detectors, we link the track and Si hit to each other.

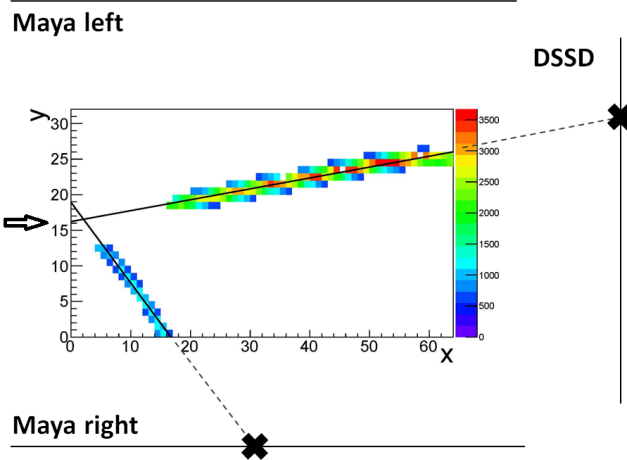


Figure 4.14: *The tracks are correlated with the hits in the Si detectors by extrapolating the fit lines to the positions of the detectors.*

E- ΔE spectra

An E- ΔE spectrum is constructed by plotting the energy loss versus the energy of the observed particles. For the latter the energy deposited in the Si detectors is used. The energy loss is calculated from the deposited charge on the pad plane. Because tracks can be originating from different positions they do not all travel the same distance along the pad plane. Therefore, to get comparable values of the energy loss, it is not the total deposited charge along the whole track that is used, but rather the charge summed over a certain region of the pad plane. For particles traveling towards the DSSDs, the last eight pad columns (i.e. perpendicular to the beam direction) are chosen. For particles traveling towards the Mayas, two equivalent regions of 8 pad rows (i.e. parallel to the beam direction) are chosen on the left and right side, such that the non-working pad region in the upper right corner is avoided⁶. The obtained energy loss values need a correction for the distance traveled inside the selected regions. This is obtained by multiplying with $\cos \theta$ for particles in the DSSDs or $\sin \theta$ for particles in the Mayas, where θ is the angle of the track with respect to the beam direction.

The above method leads to the E- ΔE spectra shown in Figure 4.15 for the DSSDs and Figure 4.16 for the Maya detectors. They are constructed from all data runs in Set 3. In all spectra we see two lines appearing, indicating the observation of two different particles in the gas. The upper line is dominating in the DSSDs, while in the Maya detectors the lower line is more vividly present. Since ^{12}C is preferentially scattered at low angles and the lighter α -particles have a higher tendency to be scattered at large angles, we suspect that the upper line belongs to ^{12}C and the lower one to α .

⁶Trying to avoid this region for the particles in the DSSDs by choosing 8 different columns accordingly, drastically worsened the resolution. Of course now some particles in the DSSDs on the right of the beam line are lost, but the statistics is high enough to allow this.

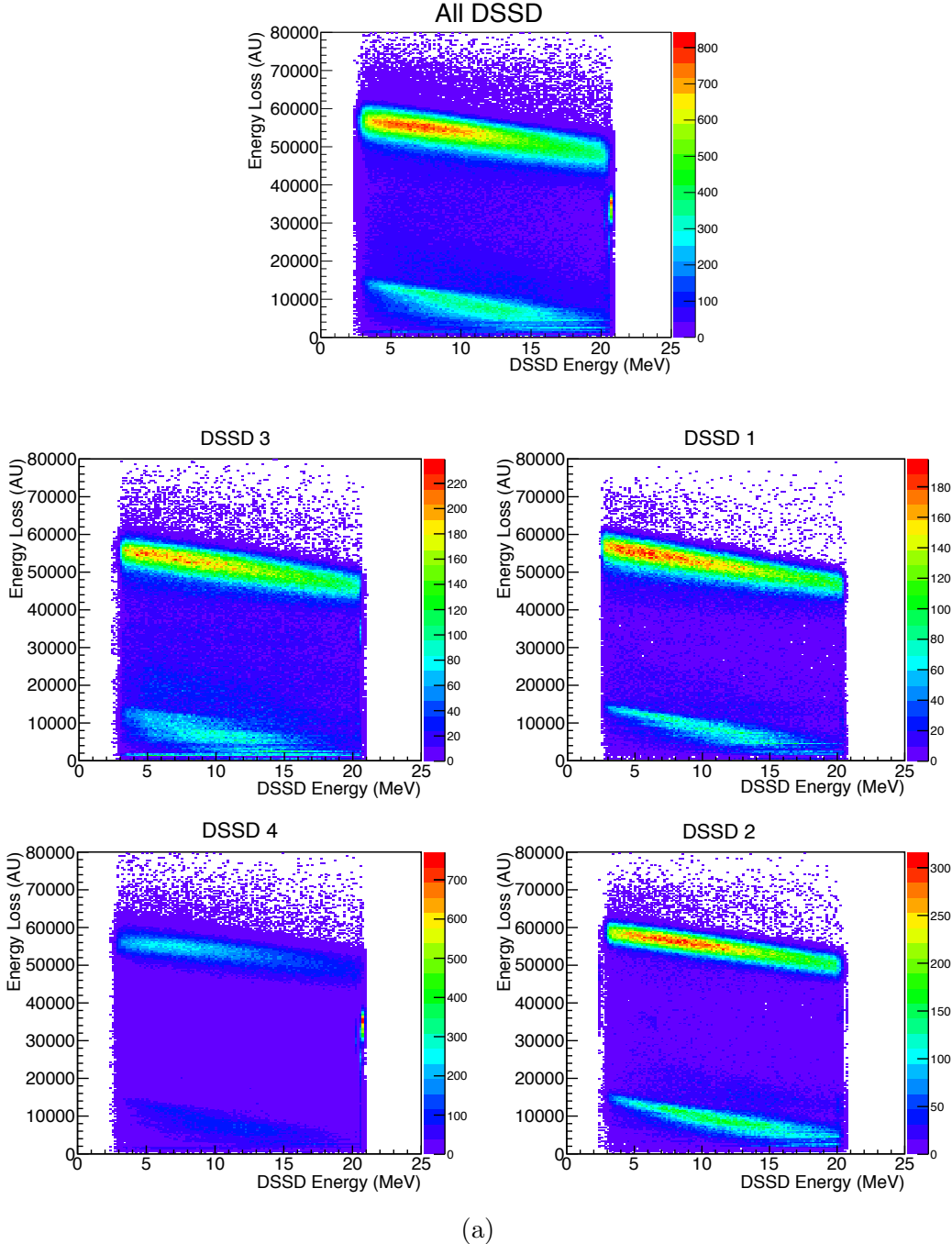


Figure 4.15: $E-\Delta E$ in the DSSDs. In the upper panel the contributions of the four separate DSSDs are summed up. The energy loss is calculated from the charge deposition on the pads and is expressed in arbitrary units. The two lines appearing in all spectra correspond respectively to ^{12}C (upper) and α (lower).

A comparison with the simulated energy loss curves in Figure 4.17 strongly confirms this assumption. Since the experimental energy loss and energy are not calculated at the same point along the track, the experimental and theoretical plots differ by some

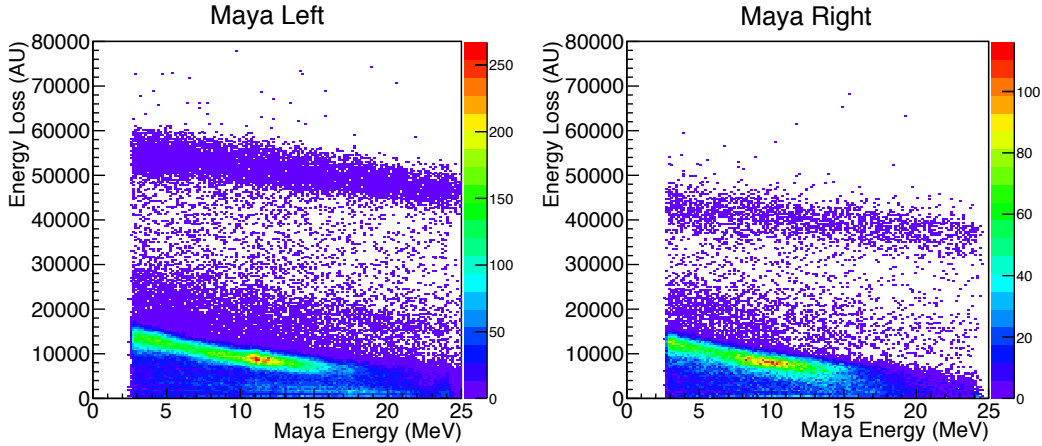


Figure 4.16: $E-\Delta E$ in the Maya detectors. The energy loss is calculated from the charge deposition on the pads and is expressed in arbitrary units. Just like in the spectra of the DSSDs, the upper line, which is a lot less intense here, belongs to ^{12}C and the lower line to α .

shift along the energy axis. Taking this into account, the relative heights match. The very low lying proton line is not appearing in the experimental spectra. We suspect that the proton's charge deposit is below the detection threshold of the pads and hence not producing any visible tracks.

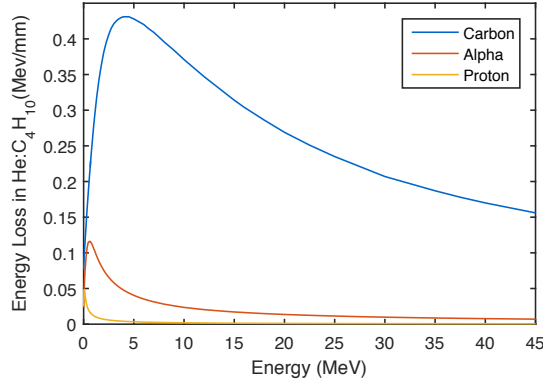


Figure 4.17: Simulated energy loss (SRIM) for carbon, α -particles and protons in $\text{He:C}_4\text{H}_{10}$ (90:10).

The broadness of the lines is a measure for the resolution. Since the Si detectors have a resolution of lower than 100 keV, this broadening is mainly caused by the determination of the energy loss. Because of some non-working pads and the presence of gaps in some tracks due to non-firing pads, this value is not always correct and lower than it should be. This is probably also part of the reason for the data points in between the two lines, together with wrong track-Si correlations.

The cut-off at an energy of ~ 21 MeV in the DSSDs and ~ 25 MeV in the Mayas is a consequence of the saturation in the electronics as described before. This implies the loss of a lot of interesting carbon information. If we look back at Figure 3.7, we see that ^{12}C scattered at forward angles on each of the three possible target atoms loses very little energy in the scattering. Hence, knowing that ^{12}C loses about 30 MeV over the total length of the chamber, we expect the scattered ^{12}C to reach the DSSDs with energies of about 35-50 MeV. What we observe however in the E- ΔE spectra, is a huge amount of unsaturated carbon signals in the DSSDs, which is impossible to explain from this kinematic reasoning. Therefore a closer look was taken at these carbon events. The distribution of their vertex positions and the fact that no recoil particles are detected (track multiplicity 1), suggest that they originate from scattering on the field cage wires. The large amount of this type of events will partly inhibit the probability to detect the desired reactions on target atoms.

In the sideways Maya detectors the saturation problem is less paramount. ^{12}C scattered at larger angles ($\gtrsim 30^\circ$) loses more energy in the reaction (see also Figure 3.7) and thus will reach the detector wall with less energy. The fact that Maya left has approximately three times more counts than Maya right can be explained by the asymmetry in the geometry. Maya right is placed two centimetres further away from the center of the pad plane (see Figure 3.4b) and hence a larger traveling distance and angle are required to reach it. The slight down shift of the carbon line can also be related to this.

4.5 Kinematic reconstruction

As a next step in the analysis we'll try to identify the different reactions that are taking place. From the measured angles and energies the kinematics of the reactions will be reconstructed.

Angle Correlation

To start, we'll focus on two track events, i.e. events with two particles leaving the interaction point. These comprise elastic and inelastic scattering reactions occupying “conventional” excited states in ^{12}C that do not decay via break-up but rather via gamma decay. An angle correlation plot can be constructed for these events setting out the angles of the two reaction products against each other. A requirement that we set for this plot is that one of the particles is identified as carbon⁷ and its angle is placed on the x-axis as θ_3 . The outgoing angle of the second particle, that may be identified or not, is placed on the y-axis as θ_4 . For tracks with correlation in the DSSDs its exact hit position can be used to determine the track's angle more accurately. For tracks with correlation in Maya we only depend on the fit line to calculate the angle.

⁷Saturating carbon is also used. In principle they can't be identified from the E- ΔE spectra, but by requiring the correlated track to have a high enough energy loss we can be sure that they are carbon.

According to the kinematic conservation laws the angles of the outgoing particles are fixed with respect to each other. Hence, in an angle correlation plot each reaction is characterized by its own kinematic line. In Figure 4.18 the kinematic lines for the $^{12}\text{C}(^{12}\text{C}, ^{12}\text{C})^{12}\text{C}$ and $^{12}\text{C}(\alpha, \alpha)^{12}\text{C}$ reactions are drawn and compared with the data. For elastic scattering, the angle vs. angle plot has the advantage of being independent of the beam energy at the scattering position, in contrary to the energy vs. angle plots that will be constructed later. In the case of inelastic scattering there is a dependence but it's rather weak. For ^{12}C on α scattering the elastic and first inelastic line - corresponding to excitation of ^{12}C to its first excited state at 4.44 MeV - can be distinguished in the data. The minima and maxima along the lines are probably owing to variations in reaction cross section with angle. The $^{12}\text{C}(^{12}\text{C}, ^{12}\text{C})^{12}\text{C}$ scattering is

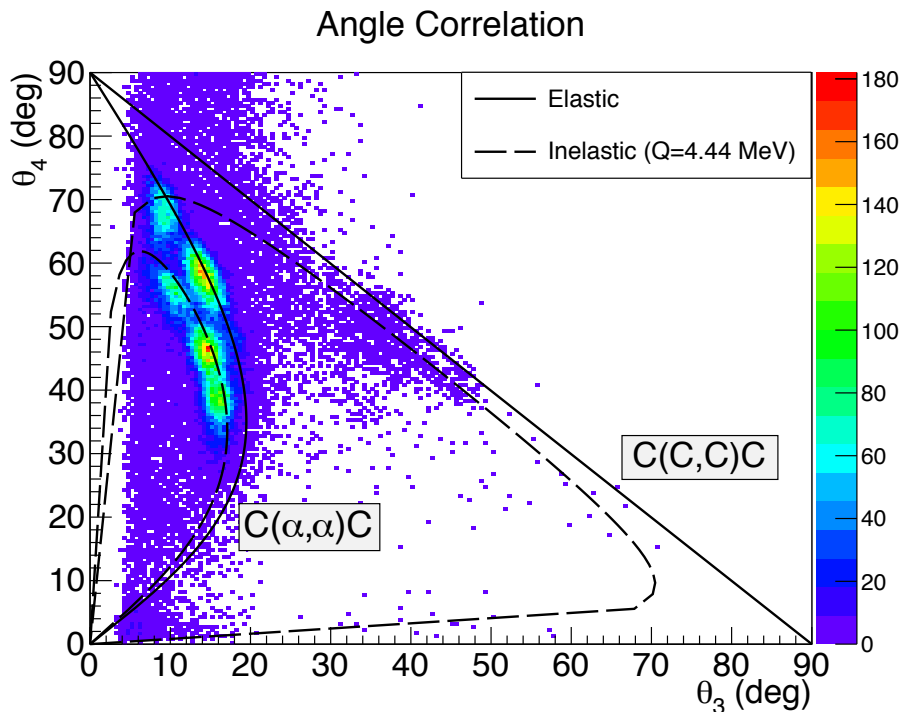


Figure 4.18: Angle correlation plot. For the two-body scattering reactions in the data the angles of the outgoing particles, θ_3 and θ_4 , are plotted against each other. As a means of comparison the kinematic lines for the $^{12}\text{C}(^{12}\text{C}, ^{12}\text{C})^{12}\text{C}$ and $^{12}\text{C}(\alpha, \alpha)^{12}\text{C}$ elastic and first excited inelastic line (for a ^{12}C beam energy of 80 MeV) are added.

much less prominently present. Most $^{12}\text{C}(^{12}\text{C}, ^{12}\text{C})^{12}\text{C}$ reactions that are observed are the ones where both ^{12}C ions are scattered at intermediate angles and detected by the Maya walls, such as the one shown in Figure 4.19a. From cross section considerations however, a strong increase is expected for more peripheral scattering, which is not observed. Using the yield formula in Equation (2.9) with the Rutherford cross section (Equation (2.8)) a comparison of the expected yield of ^{12}C elastically scattered off ^{12}C and ^4He can be made. Since almost all quantities in the formula cancel out, this calculation only depends on the relative number of ^{12}C and ^4He target atoms and their

Z-values:

$$\frac{Y_{\text{C-He}}}{Y_{\text{C-C}}} = \frac{N_{\text{He}}}{N_{\text{C}}} \left(\frac{Z_{\text{He}}}{Z_{\text{C}}} \right)^2 = \frac{2.2}{1} \left(\frac{2}{6} \right)^2 = 0.244. \quad (4.3)$$

With this result, we would expect the elastic $^{12}\text{C}(^{12}\text{C}, ^{12}\text{C})^{12}\text{C}$ to be about four times more intense than the elastic $^{12}\text{C}(\alpha, \alpha)^{12}\text{C}$ line. The reason for the disagreement between the data and the estimated expectations has to be investigated. A possible cause might be that one of the ^{12}C ions is not detected on the pad plane. However, the large-angle scattered ^{12}C emerges with very low energy, but for angles smaller than 80° the particle's range should be large enough to escape the shielded beam area and leave a visible trace. The small-angle scattered ^{12}C might be shielded up to angles of about 5° , but for larger angles it should definitely be detected. Another possible reason is linked to the trigger or electronics settings, that might be preventing these events from being detected.

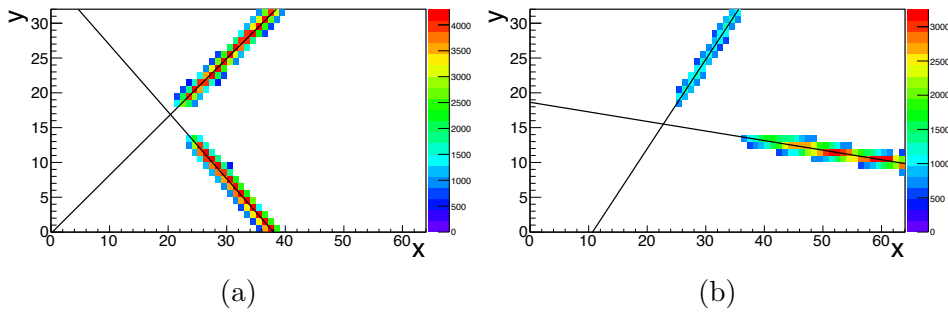


Figure 4.19: Charge deposition on the pad plane of (a) a $^{12}\text{C}(^{12}\text{C}, ^{12}\text{C})^{12}\text{C}$ and (b) a $^{12}\text{C}(\alpha, \alpha)^{12}\text{C}$ scattering reaction.

Energy reconstruction

For the two observed two-body reactions, $^{12}\text{C}(\alpha, \alpha)^{12}\text{C}$ and to a lesser extent $^{12}\text{C}(^{12}\text{C}, ^{12}\text{C})^{12}\text{C}$, we can try to reconstruct the laboratory energy of the reaction products as a function of laboratory angle. The laboratory energy is the energy of the particle right after the reaction and can be calculated as the sum of its deposited energy in a Si detector and its energy loss in the gas from the reaction vertex to the detector wall. The latter one is calculated with the help of SRIM, a program that simulates the stopping and range of ions in matter. Since we need the energy deposited in the Si detectors, saturated signals can't be used. Therefore, for the $^{12}\text{C}(\alpha, \alpha)^{12}\text{C}$ reaction we can only do the reconstruction for the α -particles, because the ^{12}C ions arrive with high energy in the DSSDs. For the same reason, for the $^{12}\text{C}(^{12}\text{C}, ^{12}\text{C})^{12}\text{C}$ reaction, we can only use the ^{12}C ions that go into the Maya wall detectors. The results are shown in Figure 4.20 together with the kinematic lines for a reaction energy of 80 MeV, the original beam energy. For the α -particles from $^{12}\text{C}(\alpha, \alpha)^{12}\text{C}$ the elastic and first inelastic line with a Q-value of 4.44 MeV are visible on a large background, just like it was the case in the angle correlation plot (Figure 4.18). The broadening under the kinematic lines, is a result of the spread on the beam energy as the reaction

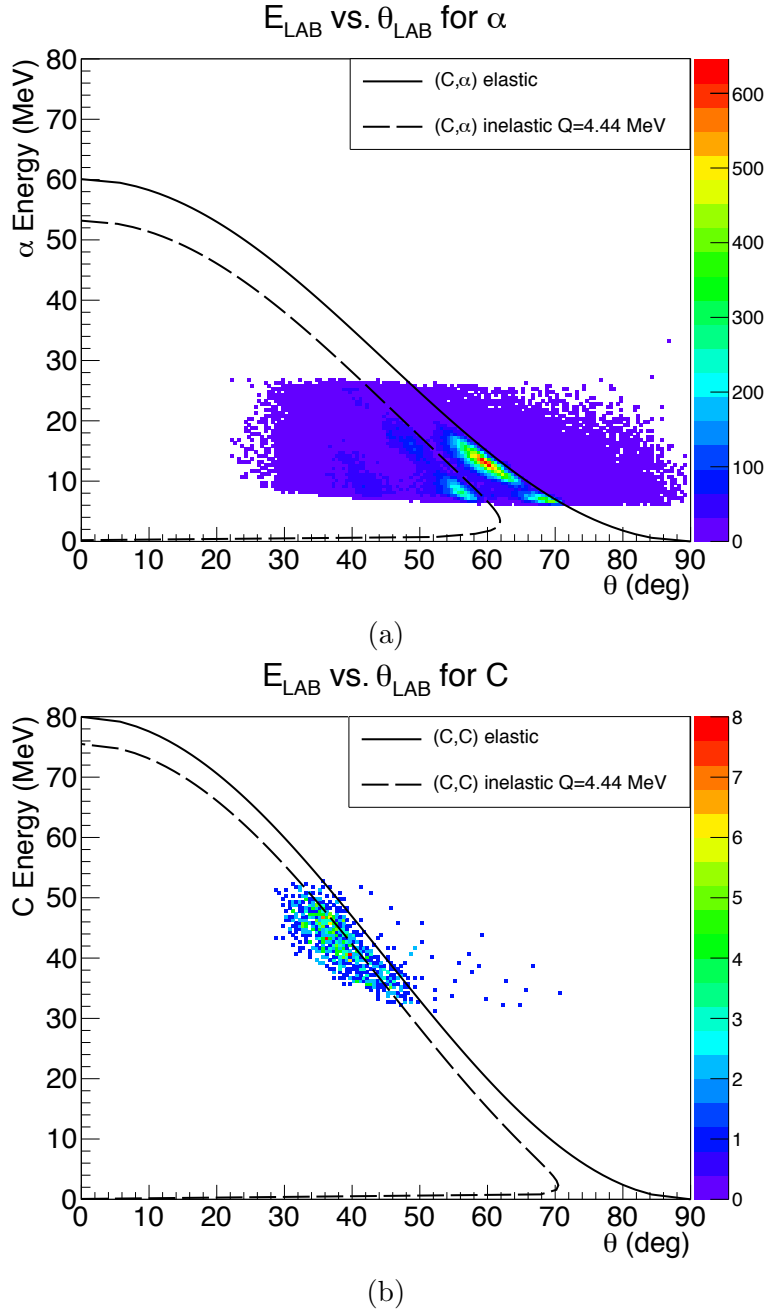


Figure 4.20: Plots of energy versus angle for (a) the outgoing α -particle in $^{12}C(\alpha,\alpha)^{12}C$ and (b) the outgoing ^{12}C in $^{12}C(^{12}C,^{12}C)^{12}C$. The kinematic lines for the elastic and the first excited inelastic reaction with a Q -value of 4.44 MeV are added for a beam energy of 80 MeV for comparison. Since the beam energy degrades as the vertex position moves further in the gas, the experimental data are spreading out below the curves.

vertex varies along the length of the chamber. A third blob seems to be appearing, which might indicate the excitation of a higher energy state in ^{12}C in the reaction. Since the cross section for $^{12}C(^{12}C,^{12}C)^{12}C$ scattering into the Mayas is very low, the

statistics for the reconstruction of the lab energy versus angle of ^{12}C aren't very good. The elastic and inelastic lines can't be distinguished in the data but at least the data appear in the right position, with again some broadening as a result of the spread in beam energy.

Break-up reaction

In addition to the two-track reactions, events with four tracks with one nicely determined vertex are observed in the data, such as the one shown in Figure 4.21. They indicate the presence of break-up reactions where the excited ^{12}C decays into three α -particles. Since these reactions originate from scattering on ^{12}C or α , the fourth track is created by the recoil particle. Unfortunately, never all of the four tracks have correlation in the Si detectors. The particles that don't reach the detector wall are usually stopped in the region between the pad plane and the Si wall and are thus unusable. Other particles are lost in the gap between the DSSDs and the Maya detectors, or are travelling up or down where there are no detectors. On top of this there is quite a lot of missing correlation; meaning that for particles that are expected in the Si, no corresponding hit signal was recorded/found. Consequently, in a lot of the cases the particles are identified by their relative energy loss with respect to each other, without information of their energy.

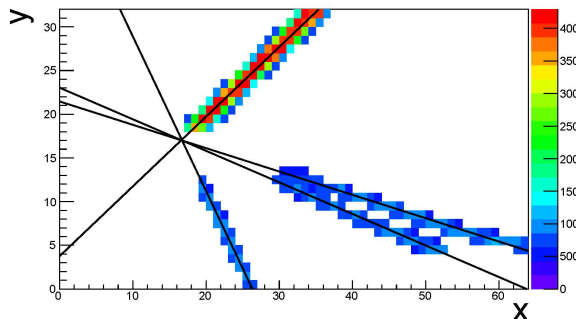


Figure 4.21: *Charge deposition on the pad plane of a break-up reaction event. From the difference in energy loss the upper particle can be identified as ^{12}C and the three lower ones as α -particles from the break-up of a second excited ^{12}C .*

A common feature in a lot of the observed break-up reactions is that two of the α -particles travel fairly close together. The third one is usually somewhat more separated from them, like in the event shown in Figure 4.21. This consistency in the kinematics indicates that the break-up proceeds through the ground-state of ^8Be as an intermediate stage. The two α -particles that make up the ^8Be stay bound a little bit longer and therefore stay closer together. The separation with respect to the third α -particle can be a measure for the excitation energy of the original ^{12}C nucleus. This can be explained by the fact that in the break-up the internal excitation energy is converted to kinetic energy of the constituents.

4.6 ^{12}C excitation spectra

To construct an experimental excitation spectrum of ^{12}C , we need the Q-value of the reaction, which was defined in Equation (2.5) as the mass difference of the part-taking particles minus any excitation energy of the final nuclei. Since we only deal with scattering reactions, the mass is conserved and

$$Q = -E_{\text{exc}}. \quad (4.4)$$

According to the expression for Q given in Equation (2.6), for binary reactions it is sufficient to know the information, more specifically the energy and angle, of one of the reaction products, in addition to the energy before the reaction. As mentioned before, the energy of a reaction product is calculated as the sum of the energy it deposits in the Si wall and its total energy loss in the gas. The energy before the reaction is just equal to the beam energy, if the gas atoms are assumed stationary. From the vertex position, we know the distance the ^{12}C beam particle has traveled in the gas before it collided. This distance and the simulated energy loss of ^{12}C allows us to calculate the beam energy right before the reaction. Eventually the calculation of the Q-value is straightforward.

In Figure 4.22 the low-lying energy levels of ^{12}C are drawn to give an overview of the states we are looking for and to eventually compare our experimental results with the literature values.

4.6.1 Ground state band

The ground state rotational band of ^{12}C can in principle be probed via elastic and inelastic scattering of the beam on each of the three target atoms. In the inelastic case, the excited ^{12}C should stay bound after the reaction and decay back to the ground state via γ -decay. Because proton tracks are not detected and the carbon is highly saturating the Si, the excitation spectrum is constructed from the $^{12}\text{C}(\alpha,\alpha)^{12}\text{C}^{(*)}$ reaction. The scattered ^{12}C ion in this reaction is useless because of the saturation, but for the α -particle which is scattered at rather large angle, we have the required energy information in the Maya detectors. Hence, the kinematic information of this latter one is used for the calculation of the Q-value. With (4.4), the energy spectrum shown in Figure 4.23 is obtained.

Three peaks can be clearly identified in the spectrum. The elastic peak at 0 MeV corresponds to the ground state of ^{12}C . The positions of the two other peaks coincide with the literature energy values of the first and second member of the ground state rotational band, which are respectively 4.44 MeV and 9.64 MeV. The third peak confirms the suspicion about the third line that is weakly visible in the plot of energy versus angle for the α -particles (see Figure 4.20a). It is particularly important to see this peak at 9.64 MeV because it gives proof of a γ -decaying state above the break-up threshold which lies at 7.27 MeV. The Hoyle state is not appearing in this

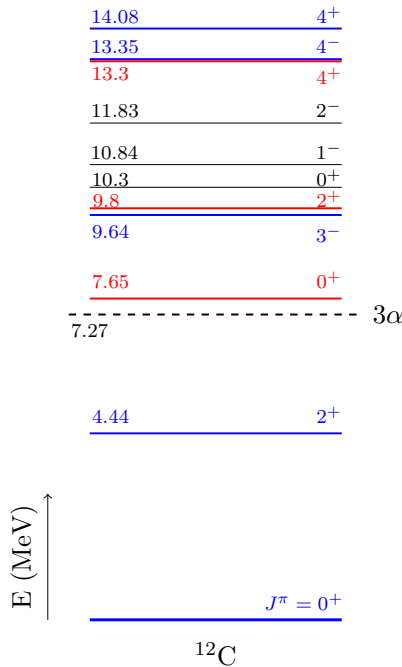


Figure 4.22: Level scheme of ^{12}C showing the low-lying energy levels with their spin and parity. Member states of the ground and Hoyle rotational band are indicated in blue and red respectively. The dashed line corresponds to the minimum threshold for break-up in three α -particles.

excitation spectrum because its γ -decay probability and hence its probability to stay bound after the reaction is too low. According to the center of mass energy of the reaction, we might expect excitations up to 20 MeV, but due to efficiency considerations the maximally probable excitation energy lies around 15 MeV. For higher excitation energies of the ^{12}C , the α -particles are scattered at too small angles to be detected in the Maya walls. They are then more focused towards the DSSDs but their energy is too high to be detected in these and is saturating the electronics, just like the carbon.

The peak shapes are not perfectly Gaussian and there is some asymmetry noticeable. An explanation for this is found when the spectrum is split in the contributions which result from detecting the α -particle in one of the right or one of the left Maya detectors. There is a clear relative shift in their peak positions of about 700-800 keV. Because the amount of counts in Maya right is so much lower this does not result in a splitting of the peak, but rather in the asymmetric Gaussian shape that we see. The origin of this shift is hard to explain. By looking in detail at individual events that contribute to this plot, it doesn't seem to stem from a mistake in the analysis. A possible explanation is a wrong estimate of the exact distances at which the Maya detectors are located. This would result in an over- or underestimation of the energy loss of the α -particle and could then account for the difference in peak positions.

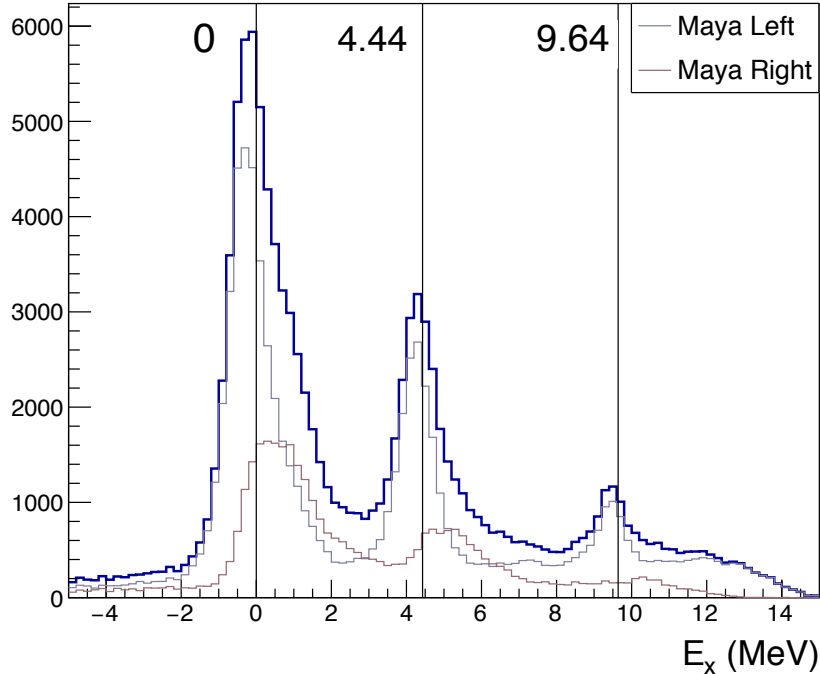


Figure 4.23: *Excitation spectrum of ^{12}C . Ground state band members were probed via the $^{12}\text{C}(\alpha, \alpha)^{12}\text{C}^{(*)}$ reaction. The vertical lines indicate the literature energy values of the ground state and the first two member states of the ground state rotational band. The separate contributions to the spectrum due to α -particles detected in the Maya detectors on the left and right are given.*

4.6.2 Hoyle band

To probe the Hoyle state and the rotational band of cluster states belonging to it, we need excitations of ^{12}C above the break-up threshold at 7.27 MeV (see Figure 4.22). As seen before, scattering of the 80 MeV ^{12}C beam either on ^{12}C or ^4He have a high enough center of mass energy, respectively 40 and 20 MeV, to allow this. If a cluster state gets populated in the scattering process, because of its structure it will preferentially decay by break-up in three α -particles immediately after its formation. For the energy reconstruction of the original excited ^{12}C , the energy information of all three α -particles is necessary. Since this is often not known, we will use the measured energy and angle of the recoiling particle for the calculation of the Q-value. The excitation spectra are created separately for the $^{12}\text{C}(^{12}\text{C}, ^{12}\text{C})3\alpha$ and the $^{12}\text{C}(\alpha, \alpha)3\alpha$ break-up reactions and the results are shown in Figure 4.24.

Immediately noticeable is the low statistics with respect to the excitation spectrum of the ground state members in Figure 4.23. The reason for this is first of all that the reaction is less probable because it requires higher excitation energies. On top of this the fitting of the four-track events is a lot more difficult than the “easy” two-track events. Especially the two α -particles from the break-up of the intermediate ^8Be nucleus rep-

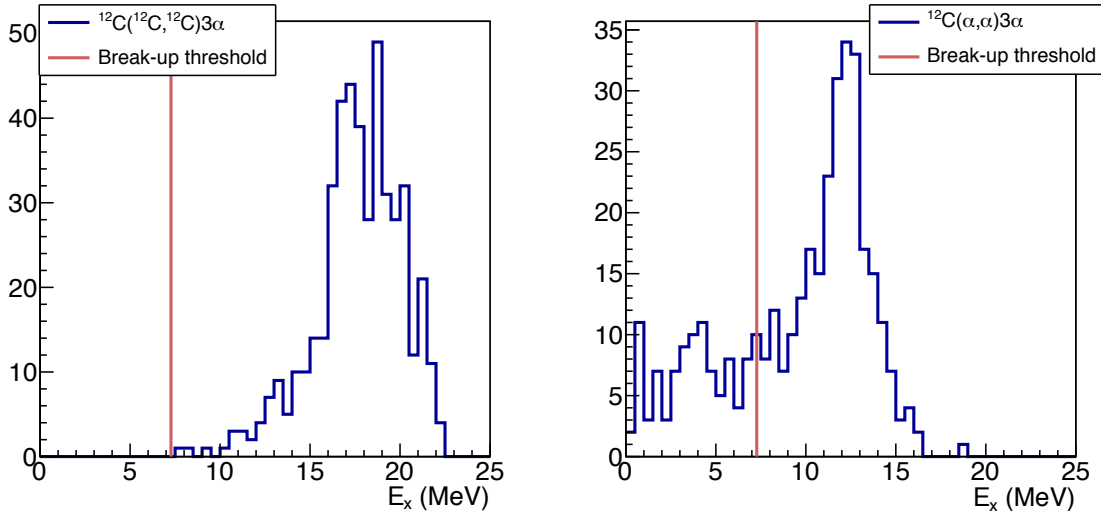


Figure 4.24: *Excitation spectra of ^{12}C . Cluster states, which are possible members of the Hoyle state rotational band, are probed via two different break-up reactions, $^{12}\text{C}(^{12}\text{C}, ^{12}\text{C})3\alpha$ and $^{12}\text{C}(\alpha, \alpha)3\alpha$. The red vertical lines indicate the threshold energy for 3α break-up. The features in the spectra are highly influenced by efficiency problems of the detector.*

resent a challenge for the analysis. Since they usually travel very close together, their charge deposition along the pads can be highly overlapping which makes it difficult to distinguish their tracks. As a result the fitting algorithm often fails to produce a nice track fit for each of the particles and the event is thrown away. Referring back to the track multiplicity plot in Figure 4.11, we see indeed that the amount of well-fitted four-track events is negligible within the full statistics.

Efficiency-wise this small amount of usable events is still reduced due to non-detection of the recoil particle in one of the Si detectors. Because we need its energy information and identity this detection is absolutely necessary. In the case of a break-up reaction due to scattering on ^{12}C , the saturation is again causing the loss of some interesting events. From Figure 4.25 we see that the recoiled ^{12}C leaves the reaction with energies above 60 MeV at small scattering angles for a Q-value around the Hoyle-state energy. Hence, taking into account a maximal energy loss of 30 MeV across the chamber, those carbons are saturating the DSSDs. If they are scattered at larger angles into the Mayas, their energy can be fully detected, but the cross section for this is greatly reduced. This must be the reason why there are so few counts at excitation energies just above the threshold. For higher excitation energies, the energy of the recoil ^{12}C is lowered and it becomes possible to detect it in the DSSDs, explaining the increase in counts.

In the case of break-up following scattering on a ^4He target atom, where all four tracks belong to α -particles, there is an additional difficulty. We need to identify in some way which of the tracks is created by the recoil α and which by the α -oarticles from

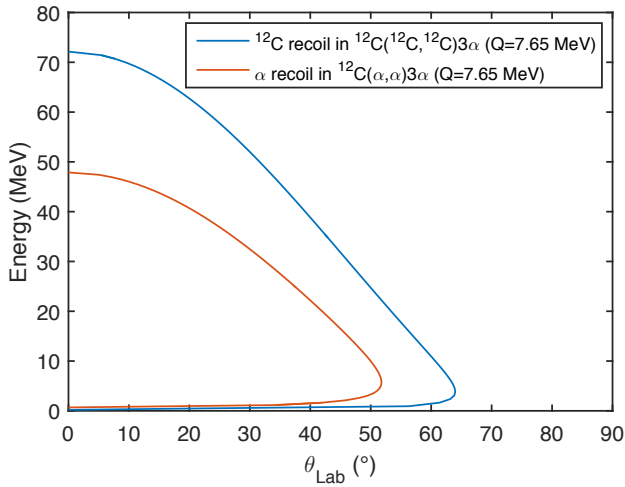


Figure 4.25: *Laboratory energies as a function of laboratory angle of the ^{12}C and α recoil particles respectively resulting from $^{12}\text{C}(^{12}\text{C}, ^{12}\text{C})3\alpha$ and $^{12}\text{C}(\alpha, \alpha)3\alpha$, for a ^{12}C beam energy of 80 Mev.*

break-up. Since the α -particles from break-up tend to travel close together, this is done by assigning the track which is mostly separated from the others to the recoil α -particle. For this the sum of the relative angles with respect to each of the other tracks is maximized. However this method is not always correct, resulting in the background at energies below the break-up threshold. For excitation energies around the Hoyle energy or higher, we see in Figure 4.25 that the recoiled α -particle, which loses maximally 10 MeV in the gas, is also saturating the DSSDs. Hence it can only be detected in the Maya-detectors up to scattering angles of $\sim 50^\circ$. The reason for the cut-off at excitation energies of ~ 15 MeV is then the same as it was for the ground state excitation spectrum: too small scattering angle to be properly detected. For scattering on an α -particle, the excited ^{12}C -nucleus and hence the α -particles in which it breaks up are usually very forward-focused. As a result, we might be losing some of these break-up events due to the fact that one of the α -tracks is shielded in the beam region. This can be yet another cause for the low statistics.

Chapter 5

Conclusion and Outlook

In this thesis scattering reactions with ^{12}C were measured, with the objective to determine the excitation energies of the Hoyle state and other cluster states in ^{12}C . For this purpose the Active Target Time Projection Chamber Demonstrator was used, which allowed us to track the reaction particles and reconstruct the reaction vertex. The main steps in the analysis of the data consisted of calibrating the detectors, fitting the particle tracks, identification of ^{12}C and α -particles and their kinematic reconstruction in some reactions. In the end, excitation spectra of ^{12}C were constructed but no cluster states could be identified.

From the results shown in the previous chapter, some conclusions can be drawn on the performance of the ACTAR TPC in the context of a scattering experiment followed by multiple particle break-up.

Resolution

Analysis of the $^{12}\text{C}(\alpha,\alpha)^{12}\text{C}^*$ and the $^{12}\text{C}(^{12}\text{C},^{12}\text{C})3\alpha$ and $^{12}\text{C}(\alpha,\alpha)3\alpha$ scattering reactions, resulted in respective ^{12}C excitation spectra for the ground-state (Figure 4.23) and possible Hoyle-state rotational members (Figure 4.24). In the former the ground state as well as the two first band members at energies of 4.44 MeV and 9.64 MeV could be reproduced. The width of the peaks gives an estimate of the final resolution, which is larger than 1 MeV. This is not particularly good and can be attributed to the many reconstruction steps which are adding up to the overall error.

The error on the angle, which is obtained from fitting the tracks is difficult to quantify but has a large contribution. There are two causes for this, which are especially important for small angle tracks. First of all, due to transparency of the field cage, the presence of the diamond detector induces a small horizontal electric field component at the forward end of the pad plane. This causes a small bending of the tracks in this region, which is influencing the track fit. On top of that the missing charge at the beginning of the track in the beam region causes an underestimation of the angle. Of course if there is a corresponding hit in the DSSDs this can be compensated for to some extent. The error on the angle is carried over to the vertex position and in a next step

to the energy loss determination. A last contribution comes from the energy resolution of the Si detectors, which are found to be approximately 50 keV for the front strips of the DSSDs and 80 keV for the Maya detectors.

Besides the errors on these different quantities that determine the Q-value, the resolution in the spectrum is also worsened by the shifted contributions of Maya left and Maya right. In further analysis of the data, an explanation should be found for this such that it can be removed or compensated for. The slight shift to the left for each of the peaks with respect to the literature lines, is possibly caused by a poor estimation of the misalignment of the beam. A better way to quantify this would be to make a full simulation of the DSSD impact points reproducing the experimental results, but this goes beyond the scope of this thesis.

Failure to identify cluster states

One of the main objectives of this study was to retrieve the energy levels of the Hoyle state and other cluster states in ^{12}C out of the data. Unfortunately the excitation spectra constructed from the break-up reactions didn't allow to conclude anything on this. A sign of the Hoyle state at an energy of 7.65 MeV is absent and no other states can be identified. Due to the scarce amount of usable events, the obtained statistics is quite low. An update of the fitting algorithm is necessary to improve the simultaneous fitting of four tracks. Loss of correlation in the Si detectors is very unfortunate, in particular for the $^{12}\text{C}(\alpha,\alpha)3\alpha$ reaction. Identification and energy information of all four α -particles is important to allow a full reconstruction of the reaction. In this way the track belonging to the recoil α -particle can be designated with more certainty, eliminating the background due to a wrong Q-value calculation. The saturation of signals higher than ~ 21 MeV in the forward placed DSSDs, caused a major loss of the energy information of the small-angle scattered recoil particles. Consequently, the spectra are for a big part only reliable on the sideways Maya-Si detectors. Especially in the case of the $^{12}\text{C}(^{12}\text{C},^{12}\text{C})3\alpha$ reaction, this drastically reduces the efficiency in the interesting energy region just above the break-up threshold. In the future efficiency simulations will be important to correctly interpret the features in the excitation spectra.

Towards the final detector

As this was the first in-beam experiment with the ACTAR TPC Demonstrator, it is not too surprising that some problems were encountered during the analysis. In fact, the results and findings obtained in this work will be valuable to decide on possible improvements in the set-up of the new ACTAR TPC detector which is currently in development.

As the final detector chamber will be bigger than the Demonstrator and extra sets of CoBo boards will be employed, it will be possible to install a larger pad plane. This should help in resolving tracks of particles that travel close together, which is quite common in this type of sequential break-up reaction. The tracks will be detected over

a larger distance and the chance of them spreading out will be larger. Saturation in the electronics causing the loss of interesting energy information should be avoided in future experiments. In this respect, it is important to understand the physics case that is studied beforehand and to know which energies are expected in the Si detectors. In this way the electronics settings can be adapted to what is suitable. Possibly an ADC with more channels (present was 12-bit) could be introduced so that larger energies can be accepted without losing in quantization resolution. The failure to detect protons on the pad plane wasn't really a problem, but it would have been nice to be able to distinguish a third reaction. It just shows that to cover a variety of particles of different mass, care must be taken in choosing the right gas conditions and gain settings in the electronics. Concerning the efficiency, the placement of the Si detectors provided a good angular coverage for the forward focused inverse kinematics experiment, with the exception of the corners of the chamber. In future experiments changes might be made in order to maximize the efficiency according to the physics of the experiment.

Despite the lack of a ground-breaking conclusion on the structure of the Hoyle state, we'll end on a positive note. The observation of the α -particles from $^{12}\text{C}^*$ break-up and the excitation strength above the break-up threshold are a clear indication for the presence and population of the cluster states in ^{12}C that we searched for. With an improved set-up, taking the above-mentioned comments into account, it should be possible to eventually measure their energies. The great reaction efficiency that was obtained for a low intensity beam makes the ACTAR TPC a very promising device to study the most exotic radioactive ion beams.

Bibliography

- [1] E. Rutherford, “The structure of the atom,” *Nature*, vol. 92, p. 423, 1913.
- [2] D. Bazin, “Nuclear physics: Symmetrical tin,” *Nature*, vol. 486, no. 7403, pp. 330–331, 2012.
- [3] M. Goeppert-Mayer, “Nuclear Configurations in the Spin-Orbit Coupling Model. I. Empirical Evidence,” *Physical Review*, vol. 78, no. 1, pp. 16–21, 1950.
- [4] E. Caurier, G. Martínez-Pinedo, F. Nowacki, A. Poves, and P. A. Zuker, “The shell model as a unified view of nuclear structure,” *Reviews of Modern Physics*, vol. 77, no. 2, pp. 427–488, 2005.
- [5] J. Al-Khalili and E. Roeckl, “The Euroschool Lectures on Physics with Exotic Beams, Vol. III,” *Springer*, vol. 764, no. 2009, pp. 253–282, 2009.
- [6] I. Tanihata, H. Hamagaki, O. Hashimoto, S. Nagamiya, Y. Shida, N. Yoshikawa, *et al.*, “Measurements of interaction cross sections and radii of He isotopes,” *Physics Letters B*, vol. 160, no. 6, pp. 380–384, 1985.
- [7] J. S. Al-Khalili, J. A. Tostevin, and I. J. Thompson, “Radii of halo nuclei from cross section measurements,” *Physical Review C - Nuclear Physics*, vol. 54, no. 4, pp. 1843–1852, 1996.
- [8] P. G. Hansen and B. Jonson, “The Neutron Halo of Extremely Neutron-Rich Nuclei,” *EPL (Europhysics Letters)*, vol. 4, no. 4, p. 409, 1987.
- [9] I. Tanihata, “Neutron halo nuclei,” *Journal of Physics G: Nuclear and Particle Physics*, vol. 22, no. 2, pp. 157–198, 1999.
- [10] W. Tyrrell Jr., K. Carroll, and H. Margenau, “Binding Energies of Light Nuclei,” *Physical Review*, vol. 55, p. 790, 1939.
- [11] M. Freer, “Clusters in nuclei,” *Scholarpedia*, vol. 5, no. 6, p. 9652, 2010.
- [12] L. R. Hafstad and E. Teller, “The alpha-particle model of the nucleus,” *Physical Review*, vol. 54, no. 9, pp. 681–692, 1938.
- [13] J. Blatt and V. Weisskopf, *Theoretical Nuclear Physics*. New York: John Wiley & Sons, 1952.

- [14] K. Ikeda, N. Takigawa, and H. Horiuchi, “The Systematic Structure-Change into the Molecule-like Structures in the Self-Conjugate 4n Nuclei,” *Supplement of the Progress of Theoretical Physics*, vol. Extra Numb, pp. 464–475, 1968.
- [15] W. von Oertzen, M. Freer, and Y. Kanada-En’yo, “Nuclear clusters and nuclear molecules,” *Physics Reports*, vol. 432, no. 2, pp. 43–113, 2006.
- [16] “National Nuclear Data Center (nndc).” <http://www.nndc.bnl.gov/>, 2016.
- [17] E. M. Burbidge, G. R. Burbidge, W. A. Fowler, and F. Hoyle, “Synthesis of the Elements in Stars,” *Reviews of Modern Physics*, vol. 29, no. 4, pp. 547–650, 1957.
- [18] F. Hoyle, “On Nuclear Reactions Occuring in Very Hot Stars .I. the Synthesis of Elements from Carbon to Nickel,” *Astrophysical Journal Supplement*, vol. 1, p. 121, 1954.
- [19] D. N. F. Dunbar, R. E. Pixley, W. A. Wenzel, and W. Whaling, “The 7.68-Mev state in C12,” *Physical Review*, vol. 92, no. 3, pp. 649–650, 1953.
- [20] C. W. Cook, W. A. Fowler, C. C. Lauritsen, and T. Lauritsen, “B 12 , C 12 , and the Red Giants,” *Physical Review*, vol. 107, no. 2, pp. 508–515, 1957.
- [21] M. Freer and H. Fynbo, “The Hoyle state in 12C,” *Progress in Particle and Nuclear Physics*, vol. 78, pp. 1–23, 2014.
- [22] M. Chernykh, H. Feldmeier, T. Neff, P. Von Neumann-Cosel, and A. Richter, “Structure of the Hoyle state in C12,” *Physical Review Letters*, vol. 98, no. 3, pp. 1–4, 2007.
- [23] P. Navrátil, J. P. Vary, and B. R. Barrett, “Properties of 12C in the Ab initio nuclear shell model.,” *Physical review letters*, vol. 84, no. 25, pp. 5728–5731, 2000.
- [24] H. Margenau, “Statistics of Excited Energy States of Nuclei,” *Physical Review*, vol. 59, pp. 627–632, 1941.
- [25] D. Brink and E. Boeker, “Effective interactions for Hartree-Fock calculations,” *Nuclear Physics A*, vol. 91, no. 1, pp. 1–26, 1967.
- [26] A. Tohsaki, H. Horiuchi, P. Schuck, and G. Röpke, “Alpha Cluster Condensation in 12C and 16O,” *Physical Review Letters*, vol. 87, no. 19, p. 192501, 2001.
- [27] Y. Funaki, H. Horiuchi, W. Von Oertzen, G. Röpke, P. Schuck, A. Tohsaki, *et al.*, “Concepts of nuclear α -particle condensation,” *Physical Review C - Nuclear Physics*, vol. 80, no. 6, pp. 1–14, 2009.
- [28] Y. Kanada-En’yo and H. Horiuchi, “Structure of Light Unstable Nuclei Studied with Antisymmetrized Molecular Dynamics,” *Progress of Theoretical Physics Supplement*, vol. 142, no. 142, pp. 205–263, 2001.

- [29] R. Roth, T. Neff, H. Hergert, and H. Feldmeier, “Nuclear structure based on correlated realistic nucleon-nucleon potentials,” *Nuclear Physics A*, vol. 745, no. 1-2, pp. 3–33, 2004.
- [30] E. Epelbaum, H. Krebs, D. Lee, and U. G. Meißner, “Ab initio calculation of the hoyle state,” *Physical Review Letters*, vol. 106, no. 19, pp. 1–4, 2011.
- [31] M. Freer, I. Boztosun, C. A. Bremner, S. P. G. Chappell, R. L. Cowin, G. K. Dillon, *et al.*, “Reexamination of the excited states of C12,” *Physical Review C - Nuclear Physics*, vol. 76, no. 3, pp. 1–9, 2007.
- [32] O. S. Kirsebom, M. Alcorta, M. J. G. Borge, M. Cubero, C. A. Diget, R. Dominguez-Reyes, *et al.*, “Breakup of C12 resonances into three α particles,” *Physical Review C - Nuclear Physics*, vol. 81, no. 6, pp. 1–9, 2010.
- [33] D. J. Marín-Lámbarri, R. Bijker, M. Freer, M. Gai, T. Kokalova, D. J. Parker, *et al.*, “Evidence for triangular D3h symmetry in C 12,” *Physical Review Letters*, vol. 113, no. 1, pp. 1–13, 2014.
- [34] H. Morinaga, “Interpretation of Some of the Excited States of 4n Self-Conjugate Nuclei,” *Physical Review*, vol. 101, no. 1, pp. 254–258, 1956.
- [35] M. Freer, M. Itoh, T. Kawabata, H. Fujita, H. Akimune, Z. Buthelezi, *et al.*, “Consistent analysis of the 2 + excitation of the 12C Hoyle state populated in proton and α -particle inelastic scattering,” *Physical Review C - Nuclear Physics*, vol. 86, no. 3, pp. 8–13, 2012.
- [36] M. Itoh, H. Akimune, M. Fujiwara, U. Garg, N. Hashimoto, T. Kawabata, *et al.*, “Candidate for the 2+ excited Hoyle state at $E_x = 10$ MeV in 12C,” *Physical Review C - Nuclear Physics*, vol. 84, no. 5, pp. 1–6, 2011.
- [37] H. O. U. Fynbo, C. A. Diget, U. C. Bergmann, S. Franchoo, V. N. Fedosseev, B. R. Fulton, *et al.*, “Revised rates for the stellar triple- α process from measurement of 12 C nuclear resonances,” *Nature*, vol. 433, no. January, pp. 1–5, 2005.
- [38] W. R. Zimmerman, M. W. Ahmed, B. Bromberger, S. C. Stave, A. Breskin, V. Dangendorf, *et al.*, “Unambiguous identification of the second 2+ state in C12 and the structure of the hoyle state,” *Physical Review Letters*, vol. 110, no. 15, pp. 1–5, 2013.
- [39] M. Freer, S. Almaraz-Calderon, A. Aprahamian, N. I. Ashwood, M. Barr, B. Bucher, *et al.*, “Evidence for a new 12C state at 13.3 MeV,” *Physical Review C*, vol. 83, no. 3, p. 034314, 2011.
- [40] A. Ogloblin, A. Demyanova, A. Danilov, S. Dmitriev, T. Belyaeva, S. Goncharov, *et al.*, “Rotational band in 12C based on the Hoyle state,” *EPJ Web of Conferences*, vol. 66, no. 66, 2014.

- [41] M. Freer, A. H. Wuosmaa, R. R. Betts, D. J. Henderson, P. Wilt, R. W. Zurmühle, *et al.*, “Limits for the 3α branching ratio of the decay of the 7.65 MeV, 2^+ state in C12,” *Physical Review C*, vol. 49, no. 4, 1994.
- [42] J. Manfredi, R. J. Charity, K. Mercurio, R. Shane, L. G. Sobotka, A. H. Wuosmaa, *et al.*, “ α decay of the excited states in ^{12}C at 7.65 and 9.64 MeV,” *Physical Review C - Nuclear Physics*, vol. 85, no. 3, pp. 85–88, 2012.
- [43] O. S. Kirsebom, M. Alcorta, M. J. G. Borge, M. Cubero, C. A. Diget, L. M. Fraile, *et al.*, “Improved limit on direct α decay of the Hoyle state,” *Physical Review Letters*, vol. 108, no. 20, pp. 1–4, 2012.
- [44] A. R. Raduta, B. Borderie, E. Geraci, N. Le Neindre, P. Napolitani, M. F. Rivet, *et al.*, “Evidence for α -particle condensation in nuclei from the Hoyle state deexcitation,” *Physics Letters, Section B: Nuclear, Elementary Particle and High-Energy Physics*, vol. 705, no. 1-2, pp. 65–70, 2011.
- [45] L. Morelli, M. Bruno, M. D’Agostino, G. Baiocco, F. Gulminelli, U. Abbondanno, *et al.*, “The $^{12}\text{C}^*$ Hoyle state in the inelastic $^{12}\text{C} + ^{12}\text{C}$ reaction and in $^{24}\text{Mg}^*$ decay,” *Journal of Physics G: Nuclear and Particle Physics*, vol. 43, no. 4, p. 045110, 2016.
- [46] L. Morelli, G. Baiocco, M. D’Agostino, F. Gulminelli, M. Bruno, U. Abbondanno, *et al.*, “Thermal properties of light nuclei from $^{12}\text{C} + ^{12}\text{C}$ fusion evaporation reactions,” *Journal of Physics G: Nuclear and Particle Physics*, vol. 41, no. 7, p. 075107, 2014.
- [47] K. S. Krane, *Introductory Nuclear Physics*. John Wiley & Sons, 1987.
- [48] H. Bethe, “Zur Theorie des Durchgangs schneller Korpuskularstrahlen durch Materie,” *Annalen der Physik*, vol. 397, no. 3, pp. 325–400, 1930.
- [49] J. F. Ziegler, M. D. Ziegler, and J. P. Biersack, “SRIM - The stopping and range of ions in matter (2010),” *Nuclear Instruments and Methods in Physics Research, Section B: Beam Interactions with Materials and Atoms*, vol. 268, no. 11-12, pp. 1818–1823, 2010.
- [50] S. Beceiro-Novo, T. Ahn, D. Bazin, and W. Mittig, “Active targets for the study of nuclei far from stability,” *Progress in Particle and Nuclear Physics*, vol. 84, pp. 124–165, 2015.
- [51] C. E. Demonchy, M. Caamano, H. Wang, W. Mittig, P. Roussel-Chomaz, H. Savajols, *et al.*, “MAYA: An active-target detector for binary reactions with exotic beams,” *Nuclear Instruments and Methods in Physics Research, Section A: Accelerators, Spectrometers, Detectors and Associated Equipment*, vol. 583, no. 2-3, pp. 341–349, 2007.

- [52] E. Pollacco, S. Anvar, H. Baba, P. Baron, D. Bazin, C. Belkhiria, *et al.*, “GET: A Generic Electronic System for TPCs for Nuclear Physics Experiments,” *Physics Procedia*, vol. 37, pp. 1799–1804, 2012.
- [53] “College Physics - Applications of Electrostatics.” <http://voer.edu.vn/c/applications-of-electrostatics/0e60bfc6/1990f7c3>.
- [54] M. Vergnes, “Tandem physics in Orsay,” *Nuclear Instruments and Methods*, vol. 146, no. 1, pp. 81–88, 1977.
- [55] D. A. Glaser, “Some effects of ionizing radiation on the formation of bubbles in liquids,” *Physical Review*, vol. 87, no. 4, p. 665, 1952.
- [56] GANIL, “ACTAR TPC Active Target and Time Projection Chamber - Conceptual Design Report.” <http://pro.ganil-spiral2.eu/laboratory/detectors/actartpc/docs/actar-tpc-conceptual-design-report/view>, 2012.
- [57] Y. Giomataris, P. Reboursard, J. Robert, and G. Charpak, “MICROMEGAS: a high-granularity position-sensitive gaseous detector for high particle-flux environments,” *Nuclear Instruments and Methods in Physics Research A*, vol. 376, pp. 29–35, 1996.
- [58] J. Pancin, S. Damoy, D. Perez Loureiro, V. Chambert, F. Dorangeville, F. DrUILLOLE, *et al.*, “Tests of Micro-Pattern Gaseous Detectors for active target time projection chambers in nuclear physics,” *Nuclear Instruments and Methods in Physics Research, Section A: Accelerators, Spectrometers, Detectors and Associated Equipment*, vol. 735, pp. 532–540, 2014.
- [59] P. Baron and E. Delagnes, “AGET , a Front End ASIC for Active Time Projection Chamber Data Sheet.” http://wiki.ganil.fr/gap/ACTAR-TPC/attachment/wiki/AgetChips/2013-01-10_AGET_manual_v5.pdf, 2013.
- [60] W. Catford, “CatKin, the kinematics program in Excel.” <http://personal.ph.surrey.ac.uk/{~}phs1wc/kinematics/>.
- [61] R. Brun and F. Rademakers, “ROOT - An Object Oriented Data Analysis Framework,” *Nuclear Instruments and Methods in Physics Research A*, pp. 81–86, 1997.
- [62] G. Bortels and P. Collaers, “Analytical function for fitting peaks in alpha-particle spectra from Si detectors,” *International Journal of Radiation Applications and Instrumentation. Part*, vol. 38, no. 10, pp. 831–837, 1987.
- [63] J. Jacquelin, “3-D Linear Regression.” <https://fr.scribd.com/doc/31477970/Regressions-et-trajectoires-3D>, 2011.

Appendix A

Calibration Parameters

A.1 Double-Sided Silicon Strip Detectors (DSSD)

DSSD	Strip	a (keV/ch)	b (10^2 keV)
1	0	5.37 ± 0.05	2.5 ± 0.5
1	1	5.40 ± 0.06	2.4 ± 0.6
1	2	5.4 ± 0.1	2.1 ± 1.1
1	3	5.3 ± 0.1	2.9 ± 1.1
1	4	5.391 ± 0.004	2.65 ± 0.03
1	5	5.36 ± 0.03	2.9 ± 0.3
1	6	5.345 ± 0.008	3.27 ± 0.08
1	7	5.4 ± 0.1	2.6 ± 1.2
1	8	5.358 ± 0.002	3.32 ± 0.02
1	9	5.340 ± 0.003	3.60 ± 0.03
1	10	5.4 ± 0.1	3.8 ± 0.9
1	11	5.359 ± 0.008	3.73 ± 0.08
1	12	5.23 ± 0.02	4.8 ± 0.2
1	13	5.3 ± 0.1	4.3 ± 1.1
1	14	5.37 ± 0.02	4.0 ± 0.2
1	15	5.24 ± 0.05	5.2 ± 0.5
1	16	5.30 ± 0.07	4.3 ± 0.7
1	17	5.35 ± 0.05	4.1 ± 0.4
1	18	5.22 ± 0.04	5.2 ± 0.4
1	19	5.38 ± 0.06	3.8 ± 0.6
1	20	5.02 ± 0.09	7.3 ± 0.8
1	21	5.210 ± 0.002	5.82 ± 0.02
1	22	5.0 ± 0.1	7.6 ± 1.1
1	23	5.1 ± 0.2	7.0 ± 1.8
1	24	5.13 ± 0.09	7.1 ± 0.8
1	25	5.13 ± 0.06	7.1 ± 0.5
1	26	5.0 ± 0.1	8.2 ± 1.3

1	27	4.95 ± 0.02	8.8 ± 0.2
1	28	5.21 ± 0.02	6.7 ± 0.2
1	29	5.20 ± 0.02	6.9 ± 0.2
1	30	5.0 ± 0.2	8.1 ± 1.4
1	31	5.04 ± 0.08	8.5 ± 0.8
1	32	6.3 ± 0.1	-0.1 ± 1.0
1	33	6.108 ± 0.009	0.08 ± 0.08
1	34	5.83 ± 0.02	2.1 ± 0.1
1	35	5.95 ± 0.04	2.1 ± 0.4
1	36	6.0 ± 0.02	1.7 ± 0.2
1	37	5.9 ± 0.1	2.7 ± 1.1
1	38	5.63 ± 0.03	3.1 ± 0.3
1	39	5.65 ± 0.01	2.4 ± 0.1
1	40	5.8 ± 0.1	1.3 ± 1.2
1	41	5.9 ± 0.2	1.6 ± 1.5
1	42	6.2 ± 0.2	0.5 ± 1.9
1	43	6.1 ± 0.2	2.3 ± 1.4
1	44	6.50 ± 0.06	-0.5 ± 0.5
1	45	6.5 ± 0.4	-0.5 ± 3.4
1	46	5.8 ± 0.2	4.8 ± 1.5
1	47	5.5 ± 0.2	6.9 ± 1.8
1	48	5.47 ± 0.09	5.9 ± 0.8
1	49	5.4 ± 0.2	7.1 ± 1.8
1	50	5.7 ± 0.1	5.1 ± 1.3
1	51	5.7 ± 0.2	4.8 ± 2.1
1	52	5.7 ± 0.2	5.4 ± 1.8
1	53	5.66 ± 0.05	6.7 ± 0.4
1	54	5.7 ± 0.1	6.6 ± 1.0
1	55	5.694 ± 0.009	5.84 ± 0.08
1	56	5.8 ± 0.1	3.5 ± 1.3
1	57	5.5 ± 0.2	4.7 ± 2.0
1	58	5.5 ± 0.1	3.2 ± 1.0
1	59	5.6 ± 0.3	1.1 ± 3.2
1	60	5.28 ± 0.04	3.0 ± 0.4
1	61	4.9 ± 0.1	8.8 ± 1.3
1	62	5.9 ± 0.4	2.7 ± 3.2
1	63	5.4 ± 0.4	5.8 ± 3.9
2	0	5.29 ± 0.03	1.7 ± 0.3
2	1	5.32 ± 0.02	1.8 ± 0.2
2	2	5.30 ± 0.03	2.1 ± 0.3
2	3	5.293 ± 0.008	2.18 ± 0.08
2	4	5.28 ± 0.01	2.4 ± 0.1
2	5	5.331 ± 0.009	2.18 ± 0.09
2	6	5.3166 ± 0.0001	2.189 ± 0.001
2	7	5.31 ± 0.05	2.7 ± 0.5

2	8	5.33 ± 0.03	2.6 ± 0.3
2	9	5.27 ± 0.06	3.1 ± 0.6
2	10	5.31 ± 0.08	3.0 ± 0.7
2	11	5.29 ± 0.07	3.0 ± 0.6
2	12	5.29 ± 0.03	3.5 ± 0.3
2	13	5.31 ± 0.02	3.3 ± 0.2
2	14	5.33 ± 0.03	3.5 ± 0.3
2	15	5.16 ± 0.05	5.3 ± 0.5
2	16	5.3074 ± 0.0005	4.129 ± 0.004
2	17	5.25 ± 0.07	4.4 ± 0.6
2	18	5.31 ± 0.06	4.2 ± 0.6
2	19	5.26 ± 0.07	5.0 ± 0.6
2	20	5.28 ± 0.02	4.8 ± 0.2
2	21	5.21 ± 0.01	5.7 ± 0.1
2	22	5.171 ± 0.004	6.20 ± 0.04
2	23	5.19 ± 0.06	5.7 ± 0.6
2	24	5.253 ± 0.008	5.63 ± 0.08
2	25	5.33 ± 0.07	5.0 ± 0.7
2	26	5.2 ± 0.1	5.7 ± 1.3
2	27	5.17 ± 0.06	6.7 ± 0.6
2	28	5.14 ± 0.07	7.2 ± 0.6
2	29	5.32 ± 0.05	6.0 ± 0.5
2	30	5.0 ± 0.1	8.5 ± 1.3
2	31	5.07 ± 0.06	8.2 ± 0.5
2	32	6.53 ± 0.04	1.0 ± 0.3
2	33	6.66 ± 0.08	1.3 ± 0.6
2	34	6.706 ± 0.003	1.95 ± 0.03
2	35	6.76 ± 0.03	0.5 ± 0.2
2	36	6.6 ± 0.2	1.0 ± 1.4
2	37	6.65 ± 0.03	-0.1 ± 0.3
2	38	6.58 ± 0.02	0.7 ± 0.2
2	39	6.5 ± 0.1	1.4 ± 0.8
2	40	6.7 ± 0.2	0.9 ± 1.7
2	41	6.61 ± 0.05	1.1 ± 0.4
2	42	6.8 ± 0.2	0.7 ± 1.2
2	43	7.07 ± 0.02	0.6 ± 0.1
2	44	6.4 ± 1.0	5.6 ± 7.9
2	45	6.8 ± 0.2	2.3 ± 1.6
2	46	6.77 ± 0.04	2.2 ± 0.3
2	47	6.60 ± 0.08	3.5 ± 0.7
2	48	6.6 ± 0.2	2.1 ± 1.6
2	49	6.6 ± 1.0	3.3 ± 7.8
2	50	6.934 ± 0.009	1.35 ± 0.07
2	51	7.0 ± 0.3	2.3 ± 2.0
2	52	7.06 ± 0.03	2.6 ± 0.2

2	53	7.06 ± 0.03	2.2 ± 0.2
2	54	7.10 ± 0.06	1.6 ± 0.4
2	55	6.9 ± 0.8	1.8 ± 6.3
2	56	6.364 ± 0.002	3.55 ± 0.01
2	57	6.082 ± 0.005	4.90 ± 0.04
2	58	6.10 ± 0.04	4.1 ± 0.3
2	59	6.707 ± 0.006	-2.37 ± 0.05
2	60	5.9 ± 0.1	3.7 ± 1.2
2	61	5.7 ± 0.1	4.4 ± 0.9
2	62	5.28 ± 0.02	6.2 ± 0.2
2	63	5.40 ± 0.05	6.4 ± 0.4
3	0	5.28 ± 0.03	2.4 ± 0.3
3	1	5.33 ± 0.06	2.1 ± 0.6
3	2	5.33 ± 0.03	2.0 ± 0.3
3	3	5.33 ± 0.02	2.4 ± 0.1
3	4	5.275 ± 0.005	2.75 ± 0.05
3	5	5.30 ± 0.06	2.7 ± 0.6
3	6	5.3 ± 0.1	2.8 ± 1.1
3	7	5.32 ± 0.01	2.7 ± 0.1
3	8	5.27 ± 0.03	3.1 ± 0.3
3	9	5.30 ± 0.03	2.9 ± 0.3
3	10	5.2 ± 0.1	3.9 ± 1.2
3	11	5.11 ± 0.06	5.1 ± 0.6
3	12	5.41 ± 0.04	2.5 ± 0.4
3	13	5.20 ± 0.06	4.5 ± 0.6
3	14	5.13 ± 0.05	5.5 ± 0.4
3	15	5.1 ± 0.2	5.4 ± 1.6
3	16	/	/
3	17	5.37 ± 0.07	3.8 ± 0.7
3	18	/	/
3	19	/	/
3	20	/	/
3	21	5.13 ± 0.04	7.2 ± 0.4
3	22	5.2 ± 0.1	6.4 ± 0.9
3	23	5.1 ± 0.1	7.0 ± 1.0
3	24	5.0 ± 0.1	7.9 ± 1.1
3	25	5.3 ± 0.1	5.4 ± 1.3
3	26	5.13 ± 0.06	7.1 ± 0.5
3	27	5.21 ± 0.05	6.5 ± 0.5
3	28	5.1116 ± 0.0006	7.536 ± 0.006
3	29	5.23 ± 0.08	7.0 ± 0.7
3	30	5.05 ± 0.09	8.6 ± 0.8
3	31	5.09 ± 0.04	8.7 ± 0.4
3	32	5.88 ± 0.03	1.1 ± 0.3
3	33	5.8 ± 0.1	1.6 ± 1.2

3	34	5.78 ± 0.06	1.8 ± 0.6
3	35	5.97 ± 0.05	0.7 ± 0.5
3	36	6.1 ± 0.2	1.1 ± 1.3
3	37	5.85 ± 0.03	3.6 ± 0.3
3	38	5.9 ± 0.2	3.3 ± 2.1
3	39	6.1 ± 0.2	1.4 ± 1.4
3	40	6.03 ± 0.09	3.2 ± 0.8
3	41	6.23 ± 0.07	2.9 ± 0.6
3	42	6.812 ± 0.004	-0.17 ± 0.03
3	43	5.6 ± 0.3	11.0 ± 2.2
3	44	6.3 ± 0.1	5.0 ± 1.1
3	45	6.4 ± 0.4	3.8 ± 3.4
3	46	6.08 ± 0.01	5.72 ± 0.08
3	47	6.23 ± 0.004	2.97 ± 0.03
3	48	6.0 ± 0.2	5.7 ± 1.3
3	49	6.1 ± 0.1	4.6 ± 1.2
3	50	6.39 ± 0.03	3.6 ± 0.2
3	51	6.3 ± 0.1	6.2 ± 1.1
3	52	6.9 ± 0.1	1.8 ± 1.0
3	53	6.466 ± 0.003	4.80 ± 0.02
3	54	6.52 ± 0.09	3.9 ± 0.7
3	55	6.36 ± 0.08	5.4 ± 0.6
3	56	7.0 ± 0.3	-0.0 ± 2.3
3	57	7.1 ± 0.4	-0.2 ± 2.8
3	58	7.1 ± 0.1	-0.3 ± 0.9
3	59	6.4 ± 1.6	5.5 ± 12.3
3	60	5.88 ± 0.02	10.8 ± 0.2
3	61	5.95 ± 0.05	10.2 ± 0.4
3	62	6.7 ± 0.3	4.9 ± 2.1
3	63	5.57 ± 0.07	13.6 ± 0.5
4	0	5.42 ± 0.03	1.4 ± 0.3
4	1	5.406 ± 0.006	1.26 ± 0.06
4	2	5.39 ± 0.02	1.4 ± 0.2
4	3	5.41 ± 0.02	1.5 ± 0.2
4	4	5.39 ± 0.02	1.8 ± 0.2
4	5	5.34 ± 0.03	2.1 ± 0.3
4	6	5.34 ± 0.03	2.6 ± 0.3
4	7	5.40 ± 0.08	2.1 ± 0.7
4	8	5.36 ± 0.04	2.6 ± 0.4
4	9	5.34 ± 0.06	2.8 ± 0.6
4	10	5.35 ± 0.04	2.7 ± 0.4
4	11	5.30 ± 0.04	3.5 ± 0.3
4	12	5.23 ± 0.07	3.9 ± 0.6
4	13	5.25 ± 0.08	4.0 ± 0.8
4	14	5.30 ± 0.05	3.6 ± 0.5

4	15	5.20 ± 0.06	4.8 ± 0.6
4	16	5.15 ± 0.03	4.8 ± 0.3
4	17	5.197 ± 0.002	4.79 ± 0.02
4	18	5.175 ± 0.002	5.05 ± 0.02
4	19	5.16 ± 0.02	5.4 ± 0.2
4	20	5.16 ± 0.07	5.5 ± 0.6
4	21	5.181 ± 0.005	5.56 ± 0.05
4	22	5.19 ± 0.07	5.5 ± 0.7
4	23	5.18 ± 0.03	5.6 ± 0.3
4	24	5.18 ± 0.03	5.8 ± 0.3
4	25	5.052 ± 0.009	7.24 ± 0.08
4	26	5.09 ± 0.02	7.0 ± 0.2
4	27	5.14 ± 0.05	6.4 ± 0.5
4	28	5.1 ± 0.1	6.6 ± 1.0
4	29	4.9 ± 0.1	9.2 ± 0.9
4	30	4.96 ± 0.09	8.6 ± 0.8
4	31	5.16 ± 0.03	6.7 ± 0.3
4	32	5.9 ± 0.2	4.1 ± 2.0
4	33	6.13 ± 0.03	2.5 ± 0.3
4	34	6.3 ± 0.1	0.8 ± 0.8
4	35	6.4 ± 0.1	0.4 ± 0.8
4	36	6.57 ± 0.05	-1.4 ± 0.5
4	37	6.278 ± 0.008	1.07 ± 0.07
4	38	6.46 ± 0.08	-0.4 ± 0.7
4	39	6.57 ± 0.03	-1.3 ± 0.2
4	40	6.6 ± 0.1	-0.02 ± 1.1
4	41	7.40 ± 0.02	-6.9 ± 0.1
4	42	6.41 ± 0.03	2.2 ± 0.3
4	43	6.6 ± 0.3	0.8 ± 2.8
4	44	6.61 ± 0.09	1.2 ± 0.7
4	45	6.3 ± 1.2	3.2 ± 10.1
4	46	6.58 ± 0.02	2.3 ± 0.2
4	47	6.4 ± 0.2	4.6 ± 1.8
4	48	6.9 ± 0.3	0.7 ± 2.2
4	49	6.696 ± 0.002	1.70 ± 0.02
4	50	6.2 ± 0.1	5.3 ± 0.9
4	51	7.3 ± 0.3	-1.9 ± 2.3
4	52	6.5 ± 0.2	3.3 ± 1.3
4	53	6.760 ± 0.005	1.11 ± 0.04
4	54	7.8 ± 0.3	-9.0 ± 2.7
4	55	6.2 ± 0.2	4.2 ± 1.7
4	56	6.37 ± 0.03	3.7 ± 0.2
4	57	6.7 ± 0.4	0.8 ± 3.3
4	58	6.3 ± 0.3	4.0 ± 2.3
4	59	6.2 ± 0.2	5.7 ± 1.3

4	60	6.1 ± 0.2	5.7 ± 1.4
4	61	5.27 ± 0.05	12.1 ± 0.4
4	62	6.0 ± 0.2	6.3 ± 1.9
4	63	6.228 ± 0.009	4.09 ± 0.07

A.2 Maya-Si detectors

Maya left

Maya nr.	a (keV/ch)	b (10^1 keV)
0	6.33 ± 0.02	6.3 ± 1.5
1	6.33 ± 0.01	5.0 ± 1.1
2	6.34 ± 0.05	2.5 ± 4.0
3	6.57 ± 0.03	3.6 ± 2.8
4	6.50 ± 0.02	-3.8 ± 1.8
5	6.46 ± 0.04	-2.7 ± 3.7

Maya right

Maya nr.	a (keV/ch)	b (10^1 keV)
0	6.475 ± 0.005	4.3 ± 0.4
1	6.56 ± 0.09	3.0 ± 7.8
2	6.46 ± 0.05	7.8 ± 4.0
3	6.45 ± 0.08	5.4 ± 6.8
4	6.51 ± 0.09	0.5 ± 7.7
5	6.54 ± 0.04	0.5 ± 3.6

DEPARTEMENT NATUURKUNDE EN STERRENKUNDE

Celestijnenlaan 200d bus 2412

3001 HEVERLEE, BELGIË

tel. + 32 16 32 71 24

fys.kuleuven.be

